

Fibroblast Growth Factors Influence Collective Cell Behavior during Mesoderm Migration

Thesis by

Amy J. McMahon

In Partial Fulfillment of the Requirements

for the Degree of

Doctor of Philosophy

California Institute of Technology

Pasadena, California

2010

(Defended January 20, 2010)

© 2010

Amy J. McMahon

All Rights Reserved

To my family, especially my mom, for supporting me through my academic
journey

and

To RJ, for keeping me sane during the tough times

Acknowledgments

There are many people to thank in my life who have intentionally or unintentionally helped me during my time at Caltech. Firstly, and most importantly, I would like to thank my advisor, Angela Stathopoulos, for providing guidance and inspiration during my PhD studies. Being in her lab has always been very stimulating (and fun), and she has been continually supportive through the millions of mouse clicks that made up my thesis work. Her breadth of knowledge has been invaluable during my graduate studies. She has shown me that being a professor is a rewarding career choice, and I plan to follow in her footsteps toward academia.

I am also thankful to Scott Fraser, who has inadvertently acted as a co-advisor for me and is the chair of my committee. He provided many helpful tidbits as we struggled with really learning microscopy (not just what the knobs do, but how microscopes really work). I am also very grateful to Willy Supatto, a postdoctoral fellow in Scott's lab. His expertise was pivotal in developing the in vivo analysis of *Drosophila* embryos. He also helped me finally jump into the realm of Matlab. Both Scott and Willy helped us to write two manuscripts, for which I am very grateful. I am thankful to my other committee members Paul Sternberg and Marianne Bronner-Fraser for always being supportive and providing feedback on papers before they were submitted.

I would like to thank the Stathopoulos lab members for providing a great environment for doing science. I would especially like to acknowledge Greg Reeves, who has patiently taught me my limited skills in Matlab and who helped us with statistical analyses. I would also like to thank my awesome baymate, Sarah Tulin, who,

in addition to being an amazing friend, has let me bounce ideas off her and put up with my bench clutter.

I would like to thank my family for being almost embarrassingly proud of me and for always supporting me even when I could not make it home as often as I would have liked.

Lastly, I want to thank RJ. He has made my time at Caltech a true joy and pleasure. He put up with me through good times and bad, and his faith in me has kept me going.

Abstract

Collective cell migration is a complex process that occurs in development and disease. As a result, understanding migration has become an important topic in biology. Several models have been developed over the last decade, but these models lack enough diversity to encompass the many different types of migration. Therefore, we propose to add mesoderm migration in *Drosophila melanogaster* as a model for collective migration. Mesoderm migration involves the movement of hundreds of cells in concert, a process that occurs in many developing animals especially during gastrulation. We have developed a technique for studying mesoderm migration in vivo using two-photon microscopy and subsequent quantitative analyses. Using this technique, we explored the role of fibroblast growth factors (FGFs) during migration of the mesoderm. *Drosophila* embryos exhibit a simplified FGF signaling pathway, with two ligands interacting with one receptor, making it an ideal system for addressing two complementary questions. Firstly, we investigated what role FGF signaling plays in collective cell migration. At the same time, we were able to ask whether both FGF ligands are required for mesoderm migration, as it is an unanswered question in the FGF field whether FGF ligands function redundantly. We found that during mesoderm migration FGF signaling is required for movement of mesoderm cells toward the ectoderm, and that both ligands are involved. We found some evidence of functional redundancy, but also found that each ligand tended to play a dominant role during different developmental events. In addition, we discovered that mesoderm migration is a multistep process, with only a subset of steps requiring FGF signaling. As a result, we have established the role of FGF during mesoderm migration and opened up many interesting avenues for further study.

Contents

Chapter 1. Introduction	1
Chapter 2. Quantitative Imaging of Collective Cell Migration during <i>Drosophila</i> Gastrulation: Multiphoton Microscopy and Computational Analysis	20
Abstract	21
Introduction	22
Materials	52
Procedures	57
Troubleshooting	65
Anticipated Results	66
Chapter 3. Dynamic Analyses of <i>Drosophila</i> Gastrulation Provide Insights into Collective Cell Migration	69
Abstract	70
Introduction	71
Methods	71
Results	81
Discussion	92
Chapter 4. Mesoderm Migration in <i>Drosophila</i> Is a Multistep Process Requiring Two FGF Ligands	94
Abstract	95
Introduction	96
Materials and Methods	99
Results	103

Discussion	120
Chapter 5. Discussion	127
Appendices	136
A. Supplementary Materials for Chapter 2	137
B. Supplementary Materials for Chapter 3	139
C. Supplementary Materials for Chapter 4	157
D. Data for the GTPase Ras1	165
Bibliography	170

Chapter 1:

Introduction

Migratory Behavior and Gastrulation

Cell migration is a complex and essential process that occurs in all animals and is important in both development and disease (Leptin, 2005; Lecaudey and Gilmour, 2006; Rorth, 2007; Montell, 2008). In the absence of or migration, tissue and organ formation is disrupted, whereas loss of migratory control is an influential factor in invasive cancers (Deisboeck and Couzin, 2009; Friedl and Gilmour, 2009; Rorth, 2009). It is critical to understand what factors control migration and whether there is an underlying mechanism that contributes to migratory behavior in all cells or if each cell type obeys different signals.

Migration has been studied extensively in many different model organisms and in many tissue types. In *Drosophila melanogaster*, well-studied migration models include the germ cells, the border cells of the ovary, the trachea, and the gut (Beccari et al., 2002; Fuss et al., 2004; Montell, 2006). We are interested in studying the earliest migration in *Drosophila* embryos, the internalization and spreading of the mesoderm during gastrulation (Wilson and Leptin, 2000), as we believe this model will add to the understanding of cell behavior during migration, particularly within the subject of collective behaviors.

Gastrulation generally involves movements of large populations of cells and sets up the different tissue layers during embryonic development (Stern, 2004). In vertebrates, the movements of gastrulation transform a ball of cells into the three germ layers: endoderm, mesoderm and ectoderm (Wang and Steinbeisser, 2009). In addition, the body plan axes are specified at this time. Each germ layer gives rise to different body parts; the ectoderm will become the epidermis and nervous system, the mesoderm will

give rise to muscles, blood, skeletal components and connective tissue, and the endoderm will form the lining of the respiratory and digestive tracts (Wang and Steinbeisser, 2009). There are only a few distinct movements that comprise gastrulation, and it is by varying these movements that gastrulation can result in different body plans. These main types of morphogenetic movements include epithelial migration, cell-cell rearrangement, cell detachment, and movement of single cells (Leptin, 2005). These movements are controlled by several key molecules including (but not limited to) the signaling molecules fibroblast growth factor, Wnt, Nodal, bone morphogenetic protein; master transcription factors like Snail, Twist, and Brachyury; and adhesion molecules like cadherins, catenins, and integrins (Wang and Steinbeisser, 2009).

In *Drosophila*, gastrulation consists of several distinct phases of movement (Leptin, 2005). The ectoderm undergoes cell-cell rearrangements that drive germband elongation, bringing the posterior of the embryo into a position to receive external signals (Butler et al., 2009). At the same time, the mesoderm is being specified and invaginates into embryo (Wilson et al., 2005). To achieve this, cells of the presumptive mesoderm first undergo apical constriction, resulting in inward movement (Figure 1A). The internalized cells then undergo an epithelial-to-mesenchymal transition, enabling them to migrate (Figure 1B). The cells collapse toward the ectoderm, allowing cells to spread dorsally along the ectoderm (Figure 1C). Finally, the mesoderm cells intercalate to form a monolayer (Figure 1D). Completion of this migration is essential for proper muscle and heart formation, as cells migrate dorsally to come into contact with specific ectodermal cues that help guide their differentiation.

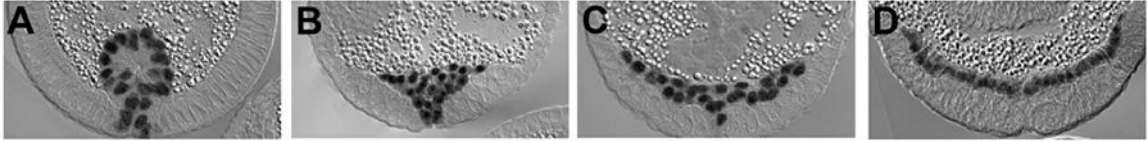


Figure 1. Gastrulation of *Drosophila melanogaster*. Cross-sections of embryos stained with twist antibody (black). **(A)** Stage 6 embryo, phase I of gastrulation. **(B)** Stage 7 embryo, phase II of gastrulation. **(C)** Stage 9 embryo, phase III of gastrulation. **(D)** Stage 10, phase IV of gastrulation.

In addition to the physiological importance of mesoderm migration, the movement of mesoderm cells serves as a model for understanding many factors that influence cell behavior, including signaling pathway interactions, cell cycle control, group vs. individual behavior, and cell polarity, amongst others. By making this system more tractable to studying dynamic behavior of groups of cells, we propose to bring this model to the forefront of the field of developmental morphodynamics and computational image analysis.

Cell Migration – A Brief Introduction

Basic Migration Machinery of a Single Cell

In order to study behavior of groups of cells during migration, it is important to first review migration of single cells, as group migration involves the coordination of individual cells in motion (Rorth, 2007; Friedl and Gilmour, 2009). A single cell must perform several molecular actions before directional migration can be accomplished. The two interrelated processes of utmost importance for directed migration involve sensing

chemoattractive gradients and polarizing a cell to move directionally; both processes occur simultaneously and repeatedly (Lauffenburger and Horwitz, 1996).

Cells respond to chemoattractive cues via chemotaxis, the process by which cells move toward a diffusible external chemical signal. Chemotaxis involves the integration of two essential processes: sensing the external gradient of a chemoattractant, and transferring the information conferred by the gradient to internal cell machinery to achieve directed migration toward the source of the chemoattractant (Devreotes and Janetopoulos, 2003; King and Insall, 2009). Chemotaxis at the single cell level has been studied extensively in *Dictyostelium discoideum*, a soil-dwelling slime mold that utilizes chemotaxis heavily during its life cycle, and in cell culture of other eukaryotic cell types (Devreotes and Zigmond, 1988; Lauffenburger and Horwitz, 1996; Etienne-Manneville and Hall, 2001; Devreotes and Janetopoulos, 2003; Pollard and Borisy, 2003).

Chemoattractants, which are most typically diffusible molecules that are secreted by a cell, are detected by neighboring cells (Friedl and Gilmour, 2009). For example, in *Dictyostelium* starving cells secrete the chemoattractant cyclic adenosine monophosphate (cAMP), causing neighboring cells to move toward the starving cells and form aggregates (Mann et al., 1997). This response provides a framework for examining chemotaxis in a generalized way. cAMP (similarly to other chemoattractants) binds to a receptor, which then transfers the signal to the inside of the cell. Once a chemoattractant binds a receptor, such as a G-Protein coupled receptor or a receptor tyrosine kinase (RTK), intercellular downstream pathways are activated (Thisse and Thisse, 2005; King and Insall, 2009). These downstream pathways, most importantly the Ras superfamily of GTPases (which

includes Ras, Rho, and Rap), are involved in generalized cell motility and polarizing the cell for directed migration in many cell types (Etienne-Manneville and Hall, 2002).

In order to move in a particular direction, a cell must establish polarity, with a lagging and leading edge (Lauffenburger and Horwitz, 1996). Subcellular localization of Rho GTPases set up this polarity, with Rac and Cdc42 localizing to the leading edge, while Rho presumably occupies the lagging edge (Nobes and Hall, 1995; Raftopoulou and Hall, 2004). Ras and/or Rap maintain the balance of Rac and Rho activation within a cell by activating guanine nucleotide exchange factors and GTPase-activating proteins (GEFs or GAPs, respectively), which in turn activate or inactivate Rac and Rho (Raaijmakers and Bos, 2009).

To move directionally, the cell must send out filopodia to continually sense chemoattractants in the environment, and lamellipodia must be formed to move the front edge of the cell forward. This is accomplished by regulated actin polymerization via Arp2/3 and several other actin-binding proteins (Pollard and Borisy, 2003; Ridley et al., 2003). Rac and Cdc42 appear to be the main activators of actin polymerization and organization at the leading edge. Additionally, integrins play a key role in forming adhesion points, which are used for attachment of a cell to the extracellular matrix (ECM) and are thought to stabilize lamellipodium formation (Friedl and Wolf, 2003; Ridley et al., 2003; Vicente-Manzanares et al., 2009). Following extension of the front of the cell, the anchor located at the back of the cell then retracts, allowing the rear part of the cell to move forward. Detachment of the anchor is achieved by breaking adhesion points at the back of the cell via FAK, ERK, and Src, while retraction is controlled by Rho kinase and myosin (Friedl and Wolf, 2003; Ridley et al., 2003). Regulation of these many

intracellular pathways through Ras and Rho GTPases allows the cell to perform chemotaxis efficiently. By combining the movement of individual cells and adding extra regulatory mechanisms collective movement is achieved (Friedl and Gilmour, 2009).

Migration in the context of a tissue

Migration of many cells as a collective is required for many diverse functions, such as organ formation and wound healing, and as a result, requires different types of group movements. For instance, cells may move as a tightly associated but small group, an epithelial sheet, a sprouting group, or a mesenchymal cluster (Friedl and Gilmour, 2009; Rorth, 2009; Weijer, 2009). Regulation of these movements is essential for proper development and to prevent diseases (Deisboeck and Couzin, 2009; Rorth, 2009).

Like in movement of a single cell, groups of cells must polarize such that a leading edge of cells is formed, and cells in the lagging section must somehow follow these leading cells to undergo directed movement (Lecaudey and Gilmour, 2006; Rorth, 2009). To this end, collective migration requires that cells be associated physically, that leading and lagging cells respond differently to chemokines, and/or that cells within the collective be able to send feedback to keep the group coordinated. This is demonstrated best in the lateral line of the zebrafish (*Danio rerio*) where differential expression of growth-factor and chemokine receptors at the leading and lagging edge allows for distinct behaviors; leading cells undergo chemotaxis in response to stromal-cell-derived factor 1(SDF1)-CXCR4 signaling while lagging cells respond to SDF1-CXCR7 and FGF signaling to retain their lagging cell characteristics and to aid in differentiation (Valentin et al., 2007; Lecaudey et al., 2008). This type of differential behavior is also observed in

the trachea of *Drosophila* embryos, where the highest level of FGF receptor activity is in leading cells and FGF signaling is responsible for outgrowth of trachea (Ghabrial and Krasnow, 2006).

To undergo directed migration the group of cells must become polarized, especially at the leading edge, and at the same time remain associated via cell-cell junctions. In the lagging cells, these junctions often involve cadherins and integrins, which keep the cells physically attached as well as provide mechanosensory feedback and cell-cell signaling (Friedl and Gilmour, 2009). Integrins additionally provide adhesion to the matrix on which the cells crawl, creating traction to keep the collective moving (Hegerfeldt et al., 2002). Polarization at the leading edge of the collective is achieved in response to chemokines and growth factors, which cause actin-rich protrusions along the leading edge most likely under the control of Rho and CDC42 as in single cell migration [see above; (Mattila and Lappalainen, 2008)]. RhoA and Rac at the back of the leading edge are responsible for reinforcing cell-cell junctions between the leading edge and lagging cells. In the many well-characterized distinct types of collective migration, these underlying themes of polarization, feedback, and chemotaxis are used repeatedly but with variation in the growth factors, chemokines, and ECM molecules that are used (Rorth, 2009).

Border cell migration in *Drosophila*, a model for invasive behavior, serves as the most well-studied example of how collective migration is achieved. Border cells migrate 200 microns over the course of 4–6 hours inside of the egg chamber of an adult female fly (Jang et al., 2007). Initially, border cells must escape from the follicular epithelium, a process dependent on PAR-1 (McDonald et al., 2008). Four to eight border cells are then

recruited by two particular follicle cells, which activate the JAK/STAT pathway in border cells to make them migratory (Silver et al., 2005). Two signaling pathways then guide the border cells to their destination: epidermal growth factor (EGF) and PDGF- and VEGF-related Factor 1 (PVF1) signaling (Bianco et al., 2007; Prasad and Montell, 2007). These two pathways serve to control two distinct phases of collective behavior in the border cell cluster. Firstly, a highly polarized leading cell is established and guides the group via chemotaxis toward the ligands for EGFR and PVF1 (Duchek and Rorth, 2001; Duchek et al., 2001). This is dependent on several downstream effectors including Myoblast City (Mbc) and Engulfment and Cell Motility (ELMO) (Bianco et al., 2007). Secondly, the leading cell is lost and the border cells begin to shuffle while probing their environment with short protrusions, which are dependent on EGFR, PVR and Notch signaling (Prasad and Montell, 2007; McDonald et al., 2008). Cells that experience the highest level of signaling, specifically signaling through the MAP kinase pathway, stay toward the front of the cluster, presumably guiding the cluster in the right direction (Bianco et al., 2007).

Border cell migration has provided the groundwork for understanding how small groups of cells can move collectively. What remains to be seen, however, is whether the signaling pathways, specifically the downstream effectors, are used in all types of migration. By studying several models, it will become apparent if there are few or many methods for achieving collective migration. We propose that adding mesoderm migration in *Drosophila* as a model will help to answer these questions. In mesoderm migration, the only known pathway that controls migration is the fibroblast growth factor (FGF) pathway. Understanding whether FGFs are involved in controlling collective

behavior of the mesoderm and what downstream effectors are involved will help to resolve whether this complex three-dimensional migration follows the same rules as other collective migratory events.

Receptor Tyrosine Kinases, Fibroblast Growth Factors, and Migration

Receptor Tyrosine Kinases and Fibroblast Growth Factors

Receptor tyrosine kinases (RTKs) are a group of membrane-bound receptors that bind to growth factors and propagate extracellular signals to the inside of the cell through several phosphorylation events. RTKs are involved in many developmental processes including differentiation, growth, survival, and migration (Schlessinger, 2000). Signaling through RTKs occurs when a ligand binds to two RTK monomers, resulting in transautophosphorylation of their cytoplasmic tails, which in turn activates downstream pathways that affect cellular processes (Schlessinger, 1994).

Fibroblast growth factor receptors (FGFRs) are a class of RTKs that are activated upon binding of an FGF ligand and a heparin sulfate proteoglycan (HSPG) accessory protein (Yayon et al., 1991). There are 24 FGF ligands for 4 receptors in humans, 3 ligands for 2 receptors in *Drosophila*, and 2 ligands for one receptor in *Caenorhabditis elegans* (Huang and Stern, 2005). Once an FGFR has been activated, additional proteins are recruited to the cytoplasmic tails of the FGFR. Proteins that are recruited to the phosphorylated FGFR contain Src homology (SH2) and phosphotyrosine binding (PTB) domains, which recognize phosphorylated sequences on the FGFR tail (Pawson, 1995; Forman-Kay and Pawson, 1999).

In vertebrates, the most studied proteins that bind activated FGFRs are growth factor receptor-bound protein 2 (Grb2) and phospholipase c (PLC); the binding of these proteins to FGFRs results in their activation via phosphorylation (Thisse and Thisse, 2005). The phosphorylation of these two proteins triggers two different cascades, which result in activation of different cellular processes (Figure 2). Grb2 and its associated nucleotide exchange factor SOS (son of sevenless) recruit and activate Ras GTPase, which in turn activates the mitogen-activated protein (MAP) kinase pathway. The last protein in the MAP kinase pathway, extracellular signal-regulated kinase (ERK), enters the nucleus and activates transcription factors, resulting in transcription of FGF target genes (Sternberg and Alberola-Ila, 1998). PLC, on the other hand, hydrolyzes phosphatidylinositol-4,5-diphosphate (PIP₂) to inositol-1,4,5-triphosphate (IP₃); IP₃ then causes a release of calcium within the cell (Thisse and Thisse, 2005). This calcium release stimulates GEFs that activate Rap1 GTPase (Bos, 2005). Rap1, in turn, aids in the maturation of cell-cell junctions and adhesion by recruitment of cadherins and integrins to the plasma membrane (Knox and Brown, 2002; Kooistra et al., 2007). RTK (and more specifically FGFR) signaling, therefore, results in different cellular responses: differentiation through Ras GTPase and cell adhesion and migration via PLC and Rap1 (Raaijmakers and Bos, 2009).

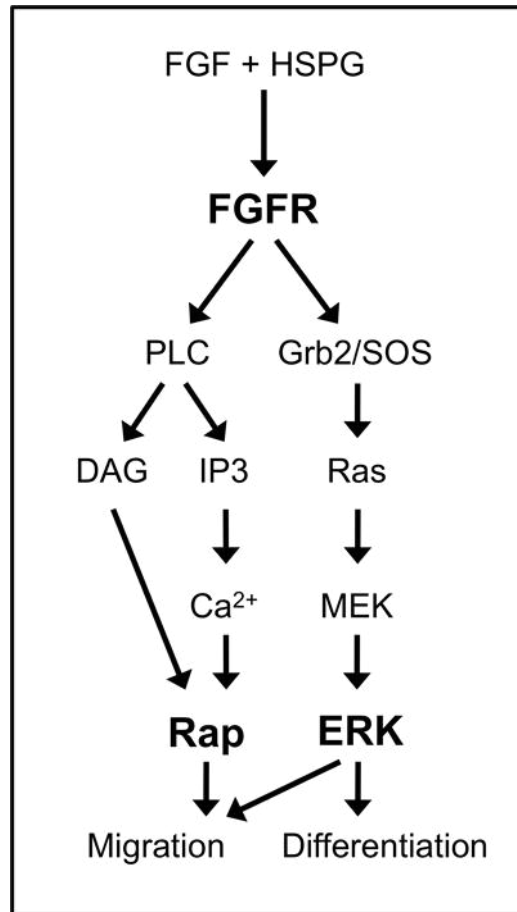


Figure 2. FGF signaling consists of two downstream pathways with potentially different outputs. A fibroblast growth factor receptor (FGFR) is activated by binding of a fibroblast growth factor (FGF) plus a heparin sulfate proteoglycan (HSPG). The activated FGFR then recruits and activates the Grb2/SOS complex, which in turns activates Ras. Ras then phosphorylates mitogen-activated protein kinase kinase (MEK), which triggers the mitogen-activate protein (MAP) kinase signaling pathway. Extracellular signal-regulated kinase (ERK), the last member of the pathway, enters the nucleus and activates transcription factors. FGFR activation also results in activation of phospholipase C (PLC). PLC converts phosphatidylinositol-4,5-diphosphate (PIP₂) to inositol-1,4,5-triphosphate (IP₃) and diacylglycerol (DAG). IP₃ triggers a release of calcium (Ca²⁺) and together with DAG activates Rap.

FGFs in Drosophila

Because of the complexity of the FGF-FGFR interactions in mammals, other models offer a simplified way to study how two or more ligands can activate one receptor and whether different downstream pathways are triggered by different ligands. In *Drosophila*, there are three FGF ligands Pyramus, Thisbe, and Branchless, and two FGFRs, Heartless and Breathless (Huang and Stern, 2005). These ligands show specificity, with Pyramus and Thisbe only activating Heartless, while Branchless activates Breathless (Kadam, S. et al., 2009). Downstream of the FGFRs in *Drosophila* both the PLC and Grb2 pathways exist, although the adaptor used to recruit Grb2, called Stumps, is unique to the fly and is only expressed in cells that express an FGFR (Michelson et al., 1998; Vincent et al., 1998). Traditionally, diphosphorylated ERK (dpERK) has been used as a readout in *Drosophila* for FGF activity and is found in the mesoderm and tracheal pits of the embryo, where the FGFRs are also expressed (Gabay et al., 1997).

The two FGFRs and their corresponding ligands are involved in specific developmental processes during embryogenesis (Dossenbach et al., 2001). Branchless and Breathless are involved in tracheal development and migration (Ghabrial et al., 2003). Heartless signaling is required for mesoderm and glial cell migration and differentiation (Gisselbrecht et al., 1996; Franzdottir et al., 2009). The interaction of Pyramus and Thisbe with Heartless during mesoderm migration and differentiation offers a unique opportunity to understand whether FGF ligands function redundantly or separately during migration (Gryzik and Muller, 2004; Kadam, S. et al., 2009; Klingseisen, A. et al., 2009).

Mesoderm Migration and FGF signaling

Mesoderm migration in *Drosophila*, as described briefly at the beginning of the chapter, is a complex three-dimensional movement of hundreds of cells during gastrulation (McMahon et al., 2008). The literature so far indicates that there are several genes contributing to this migration. Chief amongst these are Twist and Snail, transcription factors required for early patterning, invagination of the mesoderm, and later specification of muscles (Baylies and Bate, 1996; Riechmann et al., 1997; Anant et al., 1998; Grosshans and Wieschaus, 2000). Other genes implicated in mesoderm migration are the Rho GTPase Pebble, Rac, and the mRNA regulatory protein Held-out wings (HOW), which both show migratory defects (Grosshans and Wieschaus, 2000; Schumacher et al., 2004; Nabel-Rosen et al., 2005; van Impel et al., 2009). Many important signaling molecules implicated in other migratory systems are also present in the embryo at this time, including FGFs, EGFs (epidermal growth factors), TGF- β (transforming growth factor), Tumor Necrosis Factor (TNF), and Notch; although to date only FGF signaling has been demonstrated to be involved in mesoderm migration (Stathopoulos and Levine, 2004; Stathopoulos et al., 2004).

Several studies have shown that the FGFs, Pyramus and Thisbe, and their receptor, Heartless, are required for proper mesoderm migration, but fail to distinguish whether the FGFs function as a chemoattractive or permissive signal and whether both ligands are required for migration (Michelson et al., 1998; Schumacher et al., 2004; Stathopoulos et al., 2004; Wilson et al., 2005; Kadam, S. et al., 2009; Klingseisen, A. et al., 2009). Activated MAP Kinase (dpERK) is observed in the leading edge of the

mesoderm during spreading, indicating that FGF signaling is active during this time. In the absence of FGFs, migration is affected, resulting in clumping of cells or occasional shifting of cells to one side of the embryo (Michelson et al., 1998; Schumacher et al., 2004; Wilson et al., 2005).

There are two models proposed to explain the function of FGFs during spreading (Figure 3). The first model supports the idea that the FGFs act as a permissive signal, aiding in the epithelial-to-mesenchymal transition. In this model, it is thought that the FGFs are uniformly distributed in the ectoderm and that they give the mesoderm a high affinity for the ectoderm causing the cells to spread into a monolayer to maximize contact with the ectoderm (Figure 3A). Model two supports the hypothesis that FGFs are expressed in a gradient and that there is organization amongst the cells, forming a leading edge, which follows the FGF gradient dorsally (Figure 3B).

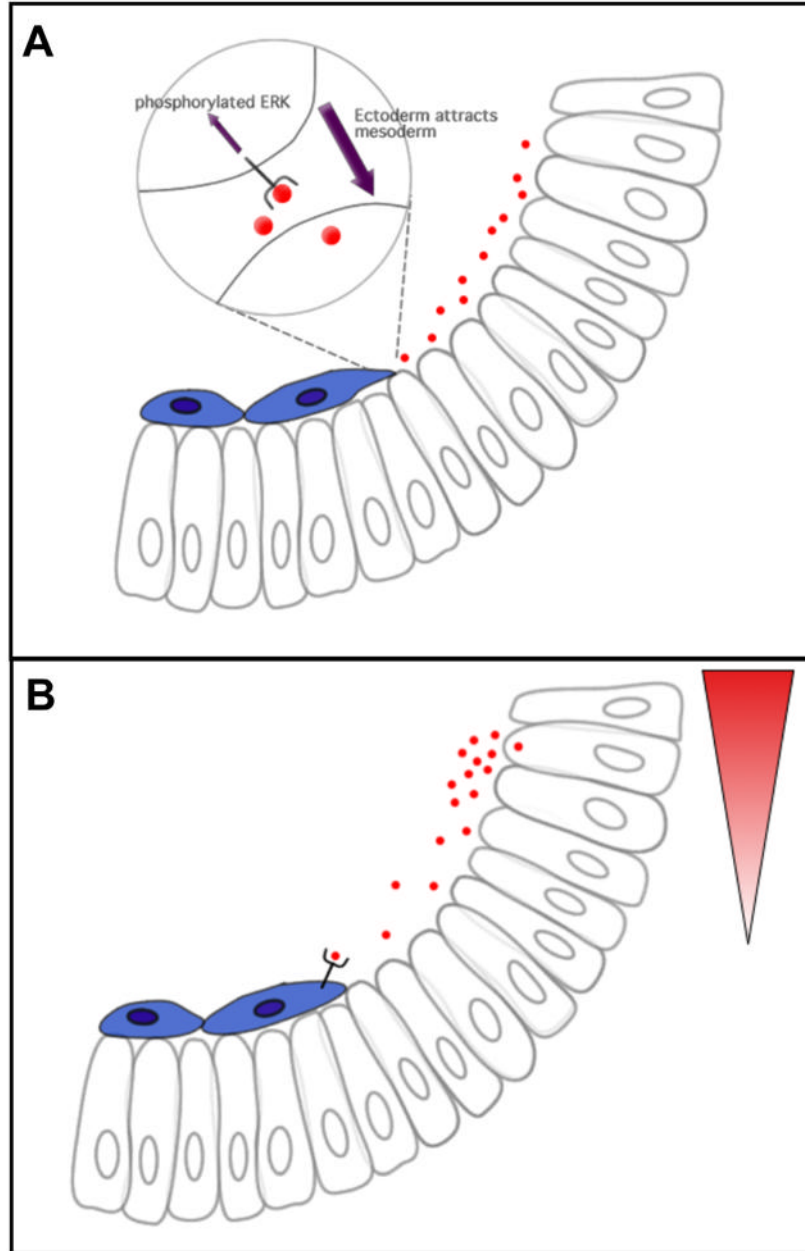


Figure 3. Two distinct models of mesoderm migratory behavior. **(A)** Model one assumes that the FGFs are evenly distributed (red circles) and that FGFs mediate contact with the ectoderm as a result of FGF signaling. **(B)** Model two predicts that FGFs are deposited in a gradient (represented by red triangle), which guides the mesoderm dorsally. Activation of the FGF pathway results in phosphorylation of an unknown factor that causes directed movement. Diphosphorylated MAP Kinase, which is present at the leading edge, may indicate “contact” with ectoderm or that a leader cell has sensed the maximal ligand concentration.

There are currently several gaps in the molecular pathways responsible for proper mesoderm migration, both related to and distinct from FGF signaling. Within the context of FGF signaling, it remains unclear whether the two ligands are necessary for mesoderm migration (Kadam, S. et al., 2009; Klingseisen, A. et al., 2009). Contributing to the limited knowledge is the fact that the migratory behavior of wild type cells has only recently been characterized, making analysis of subtle phenotypes only now possible (McMahon et al., 2008).

In vivo imaging and Quantitative Analysis

In the past, studies of mesoderm migration in *Drosophila* were performed in fixed tissues, which helped to create the foundation of knowledge in the field (Michelson et al., 1998; Leptin, 2005). Limitations in analysis, however, become apparent when trying to understand complex behavior (Wilson et al., 2005). Examining cell migratory behavior in vivo is finally within reach with the invention of highly sophisticated imaging techniques, allowing researchers to overcome previous roadblocks.

Traditionally, in vivo imaging of *Drosophila* has been problematic due to the physical properties of the embryo. The *Drosophila* embryo is highly light scattering and extremely sensitive to phototoxicity, making conventional confocal microscopy (which is useful for surface visualization) ineffective for deep-tissue imaging. Using the longer wavelength and more focused excitation of 2-photon excited fluorescence (2PEF), we can bypass much of the scattering and obtain a sufficiently strong signal for imaging migration within the embryo (Figure 4). In addition, 2PEF has excellent three-

dimensional spatial resolution, especially along the z-axis, which is lacking in traditional confocal imaging (Helmchen and Denk, 2005).

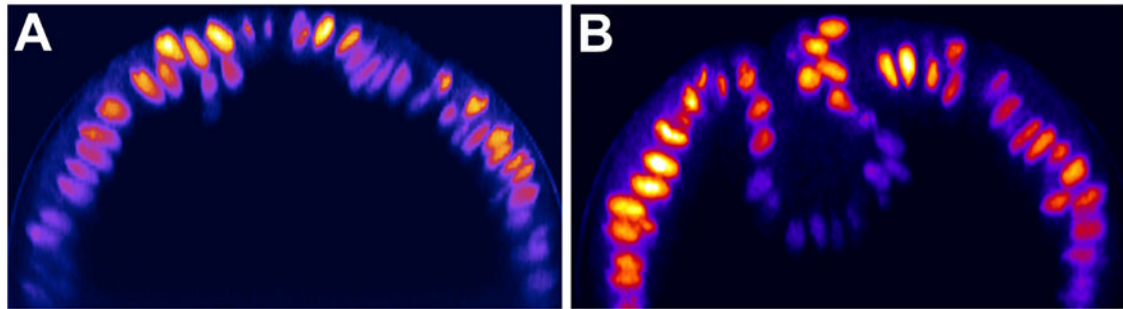


Figure 4. (A) Confocal and (B) 2-photon (2PEF) two-dimensional images along the xz-axis of an invaginating embryo. Images were taken from the same embryo expressing ubiquitin-nls-GFP, showing that 2PEF extracts more information from deep within the embryo. Scale bar = 30 nm. Grey box shows spacial resolution at 70 nm. Figure adapted from McMahon *et al*, 2008.

By using 2PEF, we can achieve a sufficient signal-to-noise ratio, which allows us to subsequently use software to track cells over time. We can then utilize computational analyses to dissect out different types of behavior during migration and also to aid in mutant analysis. Chapter 2 showcases this technique in analyzing *Drosophila* mesoderm migration. Using this approach, we are able to address the roles of FGF signaling during mesoderm migration.

Investigating the Roles of FGF signaling in Collective Mesoderm Migration

With in vivo imaging techniques developed specifically for *Drosophila* embryos, we are now able to study mesoderm migration mutant phenotypes precisely. In chapter 3, the initial function of the FGFR Heartless during mesoderm migration is accurately

characterized for the first time. We show that *heartless* mutants have collapse defects, which result in disruption of collective migration as two distinct migratory populations arise in the absence of FGF signaling. We also show that FGF signaling is only involved in movement toward the ectoderm and not in mesoderm spreading toward the dorsal side of the embryo.

Chapter 4 details the functions of the two ligands, Pyramus and Thisbe, as well as the GTPase Rap1 and its target β PS1 integrin. Both Pyramus and Thisbe are required for mesoderm migration, with Thisbe guiding collapse and both Pyramus and Thisbe contributing to monolayer formation. We demonstrate that Rap1 is also required for collapse and monolayer formation, and that Heartless and Rap1 control localization of β PS1 integrin, which is also required for monolayer formation.

Further extensions of the *in vivo* techniques and quantitative analyses used to characterize other signaling pathways will provide additional insight into collective migration. Improvements to this technique for uncovering new signaling pathways and candidate genes that most likely involved in migration are discussed in chapter 5.

Chapter 2:

Quantitative Imaging of Collective Cell Migration during *Drosophila* Gastrulation: Multiphoton Microscopy and Computational Analysis*

*This chapter, first published in *Nature Protocols* in 2009, was written by Willy Supatto, Amy McMahon, Angela Stathopoulos, and Scott E. Fraser.

ABSTRACT

This protocol describes imaging and computational tools to collect and analyze live imaging data of embryonic cell migration. Our five-step protocol requires a few weeks to move through embryo preparation and four-dimensional (4D) live imaging using multiphoton microscopy, to 3D cell tracking using image processing, registration of tracking data, and their quantitative analysis using computational tools. It uses commercially available equipment, and requires expertise in microscopy and programming that is appropriate for a biology laboratory. Custom-made scripts are provided, as well as sample data sets to permit readers without experimental data to perform the analysis. The protocol has offered new insights into the genetic control of cell migration during *Drosophila* gastrulation. With simple changes, this systematic analysis could be applied to any developing system: the definition of cell positions in accordance with the body plan, the decomposition of complex 3D movements, and the quantification of the collective nature of cell migration.

INTRODUCTION

Quantitative Imaging of Collective Cell Migration in a Developing Embryo

The combination of advanced imaging and image analysis techniques enables the investigation of large, dynamic cell populations within a developing embryo (Keller et al., 2008; McMahon et al., 2008). These imaging approaches provide a unique opportunity to study embryonic morphogenesis from the level of cellular processes to the scale of an entire tissue or organism. Gastrulation in the *Drosophila melanogaster* embryo is an excellent model system for the study of embryonic morphogenesis (Leptin and Grunewald, 1990). In less than two hours of development, ~6,000 cells undergo stereotypical morphogenetic events, such as tissue invagination (Kam et al., 1991), convergence-extension (Irvine and Wieschaus, 1994; Bertet et al., 2004), planar cell intercalation (Irvine and Wieschaus, 1994; Bertet et al., 2004), radial cell intercalation (McMahon et al., 2008), epithelial-to-mesenchymal transition (Smallhorn et al., 2004), synchronized waves of cell division (McMahon et al., 2008), and collective cell migration (McMahon et al., 2008). Although the geometry of the *Drosophila* embryo is relatively simple at early stages of development, the morphogenetic events involve highly dynamic processes and complex 3D movements of cells that prevent a complete investigation of most wild-type or mutant phenotypes based on the analysis of fixed embryos.

This protocol presents the quantitative imaging of complex cell migration in vivo, using mesoderm cell spreading during *Drosophila* gastrulation as a model system. The experimental strategy combines 4D in vivo imaging using 2-photon excited fluorescence (2PEF) microscopy, 3D cell tracking using image processing, and automated analysis of

cell trajectories using computational tools. This quantitative approach decomposes 3D cell movements, generating a precise description of morphogenetic events. Furthermore, this protocol describes the quantitative investigation of the collective nature of mesoderm cell migration. The reproducibility of morphogenetic events among wild-type embryos can be tested and mutant phenotypes can be dynamically analyzed. This approach provides a method to study complex or even subtle mutant phenotypes, such as the ability to distinguish cell populations that exhibit different behaviors (McMahon et al., 2008). We recently applied this approach to gain insights into the control of cell migration during mesoderm formation in *Drosophila* embryos (McMahon et al., 2008).

Experimental Design

The experimental workflow is divided into five main parts (Figure 1): the embryo preparation (steps 1–9), the 4D imaging (steps 10–15), the 3D cell tracking (steps 16–22), the tracking data registration (steps 23–27), and the tracking data analysis (step 28). Flies containing a fluorescent reporter are mated and embryos are collected. The chorion is removed and the embryos are mounted for live imaging and 4D image dataset acquisition using a 2PEF microscope. Typically ~2,000 mesoderm and ectoderm cells moving through the field of view are imaged during 2–3 hours of development. Each imaging dataset contains $\sim 10^9$ voxels and is processed using Imaris software to track the trajectories of the cell collection. Finally, a quantitative and automated analysis of the cell trajectories is performed using Matlab. Customized Matlab scripts required to perform steps 23–28 are provided in the supplemental section of this protocol (Supplementary Data 1). A sample dataset is also provided to allow readers to start the

procedure at step 23 without having to collect experimental data (Supplementary Data 2). This protocol can be directly applied to study mesoderm spreading in gastrulating *Drosophila* embryos. However, the workflow is not specific to this particular stage or model system. In order to facilitate the adaptation of this protocol to other stages or model organisms, we discuss below each part of the workflow with general comments and advice that are summarized in Table 1. The specific experimental choices made to study *Drosophila* gastrulation are clearly indicated.

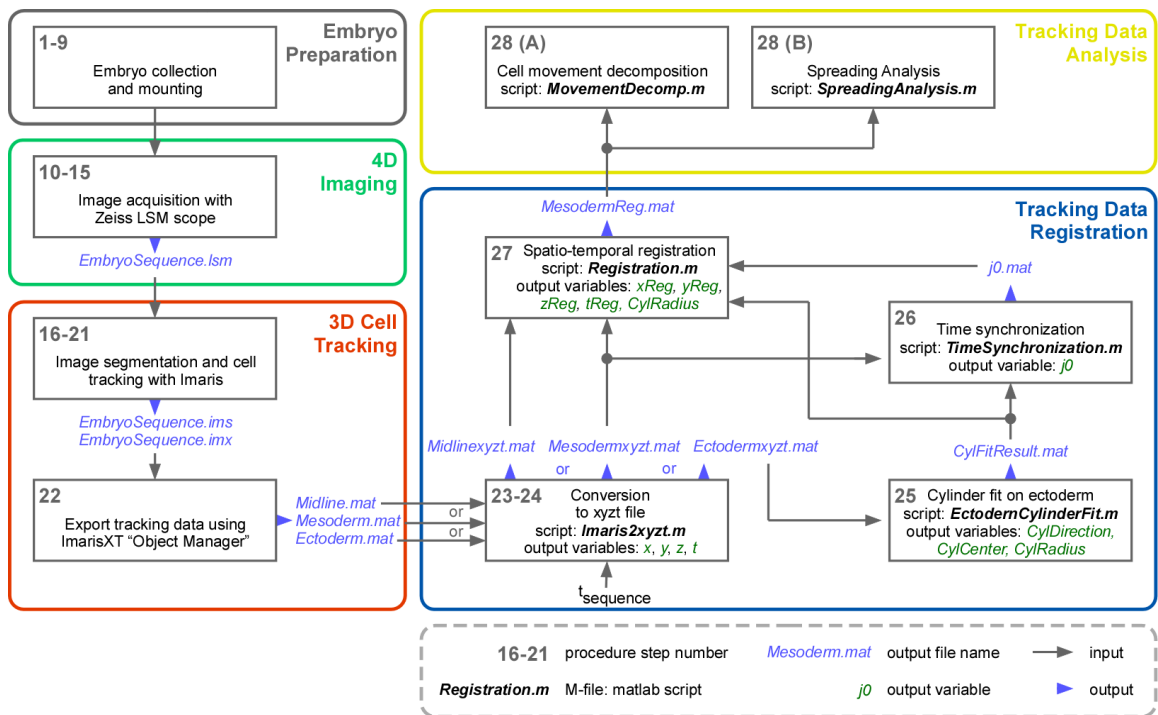


Figure 1. The experimental workflow shows the five main parts of the protocol: embryo preparation (gray), 4D imaging (green), 3D cell tracking (red), tracking data registration (blue) and tracking data analysis (yellow).

Table 1. Experimental recommendations to investigate the collective migration of large cell population in a live embryo using quantitative imaging and analysis.

Workflow step		General recommendations	<i>Drosophila</i> mesoderm spreading
Embryo Preparation	<i>Fluorescent labeling</i>	Strong and ubiquitous labeling of nuclei (histone labeling is better than nuclear localization sequence to follow cell division)	H2A-GFP line
	<i>Stabilization</i>	Avoid motion artifacts by holding the embryo in place during the acquisition time	Embryos are glued to a coverslip
	<i>Mounting setup</i>	Embryo mounting optically adapted for efficient microscopy	Embryos are imaged directly through water without coverslip
4D imaging	<i>Microscope</i>	Adapted technique of microscopy depends on the sample/process to image	2PEF microscopy Objective: 40X / 1.1NA / water immersion / large working distance For scattering tissue imaging: improved photon collection and <i>klarsicht</i> line with improved optical properties
	<i>Field of view</i> <i>Spatial/ temporal resolution</i>	Compromised between proper image processing and low phototoxicity Spatial sampling critical for proper nuclear segmentation Temporal sampling critical for proper tracking Field of view adapted to the dynamic process	200 μ m x 200 μ m x 200 μ m field of view 45 s time sampling 0.5 μ m x 0.5 μ m x 1 μ m spatial sampling
	<i>Excitation wavelength</i>	Compromised between efficient fluorophore excitation, low phototoxicity and endogenous signal excitation	Excitation at 940nm Good GFP excitation, low phototoxicity and low background
	<i>Phototoxicity</i>	Acquisition parameters (field of view, spatial/temporal sampling, laser power, resting time, wavelength) adjusted to limit phototoxicity	Mean power < 30mW 10 s resting time between z-stack acquisitions

3D cell tracking	<i>3D segmentation</i>	<p>Spatial sampling and signal-to-noise ratio critical for proper nuclear segmentation</p> <p>Manual correction can be useful</p>	<p>Signal level critical: the use of <i>klarsicht</i> mutant and improved photon collection facilitate nuclear segmentation</p> <p>Use of Imaris</p>
	<i>3D tracking</i>	<p>Temporal sampling critical for proper tracking</p> <p>Motion artifacts (embryo rolling, stage or sample drift, etc.) can drastically deteriorate tracking efficiency. If so, spatial registration can be required before 3D cell tracking step</p> <p>Manual correction can be useful</p> <p>Export of tracking results for further analysis</p>	<p>Drosophila develops fast: 45 s of temporal sampling is critical</p> <p>Use of Imaris and data export into Matlab</p>
Data Registration	<i>Spatial registration: Motion artifact correction</i>	<p>Correction of motion artifacts (embryo rolling, stage or sample drift, etc.) can be done before or after cell tracking</p>	<p>Segmented-based registration</p> <p>Angular drift correction using the tracking of ectoderm midline cells</p> <p>Matlab Processing</p>
	<i>Spatial registration: coordinate system</i>	<p>Spatial coordinate system adapted to biological structure (body plan, polarity, etc.)</p> <p>Adjustment of a reference frame to the dataset</p>	<p>Cylindrical coordinate system</p> <p>Fit of a cylinder on the ectoderm cell layer</p> <p>Matlab processing</p>
	<i>Temporal registration: synchronization</i>	<p>Synchronization of image sequences based on a biological event not disrupted in the mutant (onset of movement, etc.)</p>	<p>Synchronization using the onset of GBE</p>
Tracking Data Analysis	<i>Movement decomposition</i>	<p>Complex 3D cell motions: decomposition along each spatial directions using a coordinate system meaningful for the biology</p> <p>Color coding trajectories can be useful</p>	<p>Morphogenetic movements decomposed in the cylindrical coordinate system</p> <p>Color coding for angular position reveals spatial organization of cell migration</p>
	<i>Statistical analysis of collective motion</i>	<p>Statistical analysis depends on the nature/geometry of the collective process</p>	<p>$\theta_{\text{end}}(\theta_{\text{start}})$ graph exhibits collective migration of mesoderm cells</p> <p>Collective nature quantified as correlation coefficient of a linear regression</p>

Embryo Preparation

Nuclear fluorescent labeling. A critical component of this protocol is the choice of the fluorescent reporter, as this reporter must be suitable both for high quality imaging and cell movement quantification. To this end, fluorescent labeling of nuclei provides several advantages: (i) the nuclei are easier to segment and track from 4D image datasets than other cellular structures, such as membranes; (ii) the spatial position of the segmented nucleus can directly define the spatial position of a cell for cell movement analysis; (iii) nuclear fluorescent labeling provides a direct indicator of cell division; and (iv) transgenic lines of *Drosophila* with a strong and stable expression of fluorescent protein fused with histone or nuclear localization sequence are available (see Reagents section and Bloomington Stock Center, for instance). The lines expressing in-frame fusions of GFP to a nuclear localization sequence (NLS) have the disadvantage of producing a diffuse fluorescent signal each time the nuclear envelope breaks down during each cell division (Supplementary Movie 1). In this protocol, we used the transgenic line expressing GFP fused with Histone 2A available from Bloomington Stock Center (see Reagents section). The fluorescent Histone remains associated with the chromosomes even during nuclear envelope breakdown, giving an unambiguous signal for tracking (McMahon et al., 2008).

Sample optical properties and *klarsicht* mutant. The scattering property of the biological sample is usually the factor limiting the depth of imaging. These properties are developmental stage and species dependant (Box 1 and Figure 2). During *Drosophila* gastrulation, a high density of sub-micrometer scale refractive vesicles, mostly lipid

droplets, are observed in cells and at the surface of the yolk (Debarre et al., 2006). These lipid bodies are strong light scatterers, which results in the high scattering property of early embryos and prevents deep tissue imaging. The distribution of these lipid bodies is altered in *klarsicht* (*klar*) mutants: the lack of Klar in these embryos prevents the apical redistribution of lipid bodies at the end of cellularization, yet the homozygous mutants are viable (Welte et al., 1998). As a result, *klar* cells appear more transparent than wild-type during gastrulation (Figure 2A,B). We compared the optical properties of wild-type and *klar* embryos at stage 8 (stages defined by (Hartenstein, 1993)) by measuring the scattering mean free path, l_s^{ex} , of the near-infrared (NIR) light (Box 1 and Figure 2c). l_s^{ex} is $\sim 56 \mu\text{m}$ in wild-type embryos (blue in Figure 2D) and $\sim 76 \mu\text{m}$ in *klar* embryos (red in Figure 2D). These measures allow plotting the typical 2PEF signal decay depending on the depth of imaging (Figure 2E, see details in Box 1). It shows that the higher value of l_s^{ex} in *klar* compared to wild-type embryos is sufficient to double the intensity of 2PEF signal recorded at $80 \mu\text{m}$ depth (compare blue and red curves in Figure 2E). In this protocol, we used the *klar* background to improve the imaging depth and the level of signal — two criteria that significantly facilitate the image processing. Of note is the fact that we did not observe any disruption of mesoderm migration in *klar* embryos (McMahon et al., 2008), therefore conducting experiments in a *klar* mutant background provides a good option to improve imaging capabilities.

In most biological tissues, light scattering is the main physical process limiting the depth of imaging. In 2PEF microscopy, it can be characterized experimentally by measuring l_s^{ex} , the scattering mean free path of the excitation light. This length provides an estimate of the maximum depth of imaging and allows comparison of the imaging conditions between different biological samples. If light absorption and optical aberrations can be neglected, and assuming the fluorescence collection efficiency is constant within the depth of imaging (Beaurepaire and Mertz, 2002), the detected 2PEF signal F from a homogeneous fluorophore distribution is expected to scale as (Oheim et al., 2001):

$$F(z) \propto \left[P_0 \cdot \exp\left(-\frac{z}{l_s^{ex}}\right) \right]^2 \quad (1)$$

where z and P_0 are the imaging depth and the average incident laser power at the tissue surface, respectively. Hence, l_s^{ex} is experimentally estimated by acquiring a z-stack of images through the sample with a given incident power, by measuring the average 2PEF signal $\langle F(z) \rangle$ in a homogenous area at each z-position and the background signal

$F_{background}$, and by plotting $G(z) = \frac{1}{2} \ln[\langle F(z) \rangle - F_{background}]$. A linear regression on $G(z)$

provides an estimate of the slope as $-1/l_s^{ex}$ (Figure 2c). We measured l_s^{ex} at 940 nm in the mesoderm and ectoderm tissues in wild-type and *klar* embryos at stage 8 as 56 and 76 μm , respectively (Figure 2d). The estimation of l_s^{ex} displays the typical 2PEF signal decay based on equation (1) (Figure 2e). This graph shows that at 80 μm in depth, the signal in wild-type embryos at stage 8 is low (blue line) and twice as much signal can be expected in a *klar* mutant at the same stage (red line). As a comparison, we provide l_s^{ex} measurements and signal decay in stage 5 *Drosophila* embryos and in zebrafish embryos from previous reports (Debarre et al., 2004; Supatto et al., 2008) (Figure 2D,E). It demonstrates that the optical properties of embryonic tissues and the subsequent limitation of imaging depth is highly stage and species dependant.

Box 1. How to characterize the optical properties of a biological sample in 2PEF microscopy.

To show the scattering properties of embryonic tissues and the subsequent limitation of imaging depth are stage and species dependant, we plotted the depth-dependent 2PEF signal from stage 5 *Drosophila* or early *zebrafish* mesoderm (gray curves in Figure 2E) based on the previous experimental measurement of the scattering properties (gray in Figure 2D). The signal decay demonstrates that stage 5 (before gastrulation,) and stage 8 *Drosophila* embryos (dark gray and blue curves in Figure 2E,

respectively) exhibit significantly different properties, whereas these two stages are separated by only 1 hour of development. In addition, the 2PEF signal at 80 μm is expected to be 5 times weaker in *Drosophila* at gastrulation (blue curve in Figure 2E) compared to early *zebrafish* embryos (light gray in Figure 2E) for the same labeling and imaging conditions. Hence, the maximum depth of imaging and the choice of the microscopy technique depend on the stage and model system. For instance, as opposed to *Drosophila* embryos, the imaging of mesoderm structures at 80 μm in early zebrafish embryos is achievable with confocal microscopy and does not require 2PEF microscopy (Supatto et al., 2008).

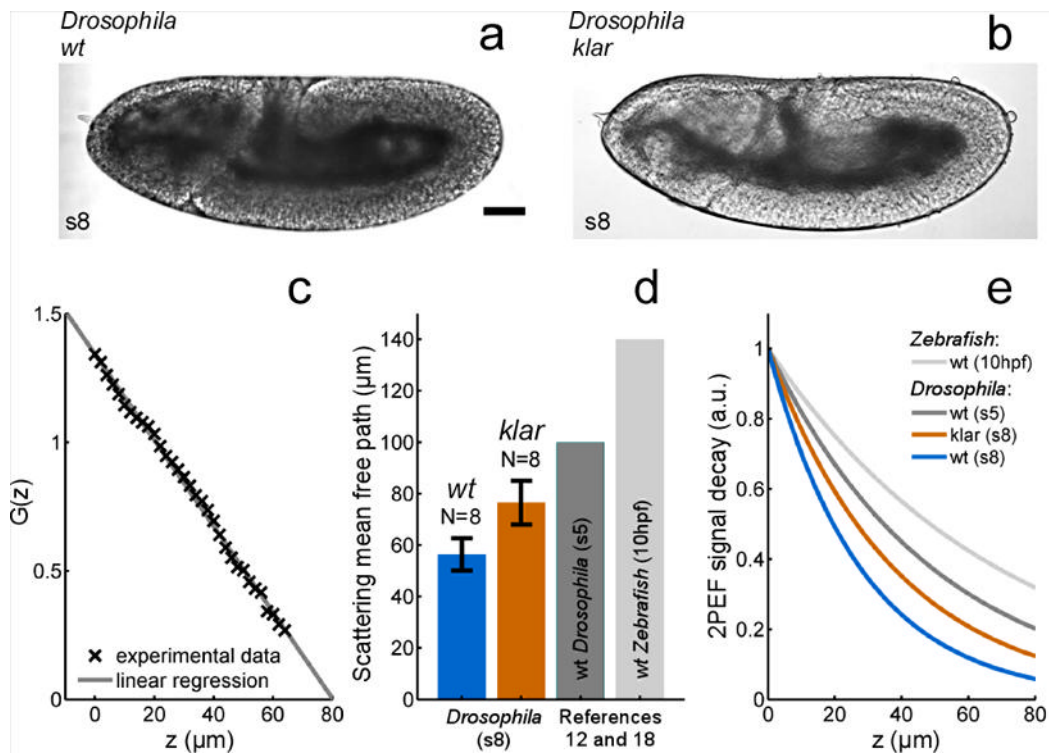


Figure 2. Optical properties of mesoderm in early *Drosophila* and zebrafish embryos. Using brightfield microscopy, wild-type *Drosophila* embryos (A) at stage 8 (s8) appear darker than *klarsicht* mutants (B), which is due to the different light scattering properties of the cells. The

experimental quantification of these optical properties is performed as explained in Box 1. Each fluorescent imaging dataset is analyzed by plotting $G(z)$ (see Box 1 for its definition) and fitting the experimental data using a linear regression (C). This analysis allows estimation of the scattering mean free path l_s^{ex} of the excitation light from embryonic tissues at different stages or from different species (D). The graph (D) shows that *klarsicht Drosophila* embryos (red) exhibit $l_s^{ex} \sim 76 \mu\text{m}$, which is $20 \mu\text{m}$ larger than wild-type embryos at the same stage (blue). The error bars represent the standard deviation of the l_s^{ex} estimations for $N = 8$ embryos. Previous studies show that similar measurements performed in *Drosophila* blastoderm cells at stage 5 (s5) and in zebrafish mesoderm cells at bud stage (10hpf, hours post fertilization) result in l_s^{ex} two and three times larger, respectively (dark and light gray in d, respectively). These measures are used to plot the typical 2PEF signal decay in depth (E) as explained in Box 1. This graph displays the loss of fluorescence signal when imaging deeper inside an embryonic tissue and permits comparison of the expected signal loss observed in tissues with different optical properties. It shows that the difference in optical properties between wild-type *Drosophila* (blue curve) and *klarsicht* (red curve) s8 embryos is significant, and results in the ability to obtain twice the fluorescent signal at $80\mu\text{m}$ within *klarsicht* embryos. It also shows that the signal is three times higher in wild-type *Drosophila* at s5, and 5 times higher in zebrafish embryos under similar imaging conditions (dark and light gray curves at $80 \mu\text{m}$, respectively). Scale bar in A1 indicates $50 \mu\text{m}$; *wt*: wild-type.

Embryo mounting procedure. The mounting procedure is a critical step of the embryo preparation for optimized imaging. The use of materials inducing optical aberrations on the optical path, such as agarose gel, should be avoided or limited. In order to enable a proper quantification of cell movements and avoid motion artifacts, the embryos must be precisely oriented and maintained in place during the image acquisition. Furthermore, the mounting of the embryos should not deform the embryo itself (for instance, by

squeezing the embryo between coverslips), as this might alter the cell behaviors. In the case of *Drosophila* embryos, we found that mounting them in water and imaging without an additional coverslip between the specimen and the objective offered the best compromise between embryo health and image quality. This arrangement avoids the refractive index mismatch between embryo and immersion solution that would be present with an oil-immersion objective, prevents hypoxia, and does not induce deformation. The embryos are oriented and maintained in place by gluing them on a coverslip. The orientation is first based on the shape of the embryo: the dorsal side has a smaller curvature than the ventral side (Supplemental Movie 2). The well-oriented embryos are then selected at early stage 6 (Hartenstein, 1993) under the microscope with the ventral side facing the objective. The onset of ventral furrow formation at stage 6 makes it easy to identify well-oriented embryos: the furrow should face the objective, in the middle of the field of view.

4D-imaging

Multiphoton microscopy for *in vivo* imaging of scattering embryos. Choosing the appropriate microscopy technique to image living embryos depends on several criteria: the required spatial and temporal resolution, the size or shape of the embryo and volume to image, the sensitivity to phototoxicity, and the optical properties of the tissue. Imaging the early stages of *Drosophila* gastrulation is limited by two major factors: the light scattering properties of the tissue and phototoxicity. These limitations are especially apparent when imaging mesoderm formation using confocal microscopy. When using confocal microscopy only half of the required depth is visualized and the required

spatiotemporal sampling quickly induces strong phototoxicity (see below). 2PEF microscopy (Supatto et al., 2005) and other multiphoton microscopy techniques (Debarre et al., 2006), are better choices to support the 4D (3D in space and 1D in time), long-term, deep-tissue imaging of *Drosophila* embryos in a manner that does not compromise their viability.

In multiphoton microscopy, the sample is illuminated with NIR radiation and the spatial resolution is intrinsically three dimensional, resulting in (i) good penetration and low absorption of the excitation light, and (ii) efficient collection of the emitted light, including scattered photons, due to the absence of pinhole. We reported the imaging of internalized mesoderm cells up to a depth of 80 μm within the embryo using 2PEF (McMahon et al., 2008). Another significant advantage of using NIR radiation, compared to the linear excitation at 488 nm used in standard fluorescence microscopy, is that the nonlinear excitation of GFP can be obtained using a wavelength (see below) inducing a lower background (i.e., autofluorescence).

The main limitation of 2PEF microscopy, as with any laser scanning microscopy, is the time of acquisition. Although *Drosophila* embryonic development is fast, the morphogenetic movements are slow enough to be captured with laser scanning microscopy. However, the acquisition speed becomes a limitation when imaging a large volume of cells while trying to maintain good spatial and temporal sampling. As a consequence and in order to avoid phototoxicity and obtain a signal level and spatiotemporal sampling suitable for proper image analysis, the 2PEF imaging of *Drosophila* mesoderm cells requires careful adjustment of the imaging parameters (i.e.,

objective, spatial and temporal sampling, field of view, resting time, laser power, wavelength).

Phototoxicity. The depth of imaging, the level of fluorescent signal, and the speed of acquisition required for this procedure can easily lead the investigator to use imaging conditions that induce phototoxic effects and prevent the normal development of the imaged embryo. For this reason, it is important to systematically check for any sign of photo-induced effects on movement. The imaging parameters must be carefully tuned in order to stay far away from phototoxic conditions while maintaining sufficient image quality to support the subsequent image processing steps. Though the molecular mechanisms resulting in phototoxicity in 2PEF microscopy are not fully understood, phototoxic processes usually appear to be highly nonlinear (Hopt and Neher, 2001; Ji et al., 2008): meaning that the threshold is sharp and that small changes in imaging parameters are enough to switch from toxic to nontoxic conditions.

Several criteria can be used to identify phototoxic effects in *Drosophila* at gastrulation. The level of endogenous fluorescent signal (also called autofluorescence) is often a good indicator. If the endogenous signal from the yolk or the vitelline membrane begins to approach the level of the GFP fluorescent signal, it indicates that the imaging conditions will most likely induce phototoxicity. In this case, a different GFP labeling and/or a different excitation wavelength should be used. The cell movements can indicate phototoxicity: if these movements slow down independently of the temperature and specifically within the field of view, it is a clear effect of phototoxicity. Finally, it is possible to observe more subtle effects at low laser power level, including changes affecting cell division rates. Cell divisions occurring a few minutes earlier or later than

normal induce a disruption of the cell division pattern that can be quantified (McMahon et al., 2008). We interpret this effect as a mild disruption of cytoskeleton dynamics. Lastly, it is important to note that phototoxic effects may result long before any photobleaching is induced. Hence, the mere absence of photobleaching is not a good indicator of non-invasiveness.

How to choose the appropriate objective. For the deep-tissue imaging of highly scattering tissue using 2PEF microscopy, the ideal objective must have a large working distance, a high numerical aperture (NA), a low magnification, and good transmission of NIR light. The large working distance prevents embryo hypoxia and allows deep-tissue imaging. The high NA improves the spatial resolution, the 2-photon excitation, and the light collection efficiency. The low magnification allows image acquisition from a larger area, which significantly improves 2PEF signal collection efficiency (Beaurepaire and Mertz, 2002). For this procedure, we used a 40x water immersion objective with 1.1 NA and working distance of 600 μm .

How to choose the appropriate excitation wavelength. The choice of the excitation wavelength is critical to obtain an efficient fluorophore excitation, a low endogenous signal (background), and low phototoxicity. Use of a tunable femtosecond laser allows the user to test different wavelength and choose the best compromise. When imaging GFP, the optimal 2-photon excitation wavelength is 940–950 nm. We observed that in gastrulating *Drosophila* embryos, the use of lower wavelength leads to higher phototoxicity, lower GFP excitation efficiency, and higher levels of endogenous fluorescent signal. Consequently, in this case, the absorption of water in the 950 nm wavelength range does not play a significant role in the phototoxicity.

Improved collection efficiency of scattered photons in 2PEF microscopy. In most techniques of fluorescence microscopy, such as confocal microscopy, only the ballistic photons that are not scattered from the emission spot en route to the detector contribute to the fluorescent signal. As the fluorescence excitation is restricted to the focal volume in 2PEF microscopy, every emitted photon can contribute to the signal, including scattered photons. In practice, it means that the signal collected from scattering tissue can be improved by collecting light in every spatial direction. For instance, the 2PEF signal can be collected in both the trans- and epi-direction if the microscope setup permits it. In our case, we added a silver mirror in the trans-direction, which reflects forward-directed photons and contributes to collection of some of them by the objective in the epi-direction. This straightforward procedure allowed us to collect up to 30% more 2PEF signal with the same illumination conditions, thus significantly improving the image quality and facilitating the image processing steps.

How to choose the appropriate spatial and time sampling. The spatial resolution has to be sufficient for the proper segmentation of nuclei. Even if the tracked objects are large (nuclei are of $\sim 5\text{--}10\ \mu\text{m}$ diameter), the gap between them can be small ($< 2\ \mu\text{m}$). As a result, a high NA objective is required, especially for the segmentation of nuclei located deep within the embryo. A spatial sampling of $0.5\ \mu\text{m}$ per pixel in x,y direction and $1\ \mu\text{m}$ in z appears sufficient.

The time resolution is critical in order to ensure error-free cell tracking, and to avoid the incorrect assignment of cell identities due to temporal aliasing. Temporal aliasing occurs when 3D stacks of images are acquired with a time interval between two frames too large to permit faithful cell tracking. Indistinguishable nuclei travel with a

velocity v and are separated by a distance d . When images are acquired with a time interval Δt between two stacks, for the nuclear trajectory to be extracted unambiguously the distance $v.\Delta t$ travelled by the cell in between two stacks must be less than half the distance d [i.e., $v.\Delta t < d/2$; (Vermot et al., 2008)]. In our case, as $v \sim 5 \mu\text{m}.\text{min}^{-1}$ and $d \sim 10 \mu\text{m}$, thus the requirement is that $\Delta t < 1 \text{ min}$. We used $\Delta t = 45\text{--}50 \text{ seconds}$.

3D-Cell Tracking

Image processing techniques other than cell tracking have been successfully applied to quantify morphogenetic movements in embryos. For instance, image cross-correlation velocimetry is specifically adapted to measure tissue deformation by direct differential analysis of the estimated velocity field (Debarre et al., 2004; Supatto et al., 2005; Zamir et al., 2006). However, the spatial resolution is limited by the size of the image interrogation window and this approach is usually limited to 2D. Cell tracking based on the segmentation and tracking of nuclei provides an opportunity to follow the behavior of individual cells in 3D with good spatial and temporal resolution (Figure 3).

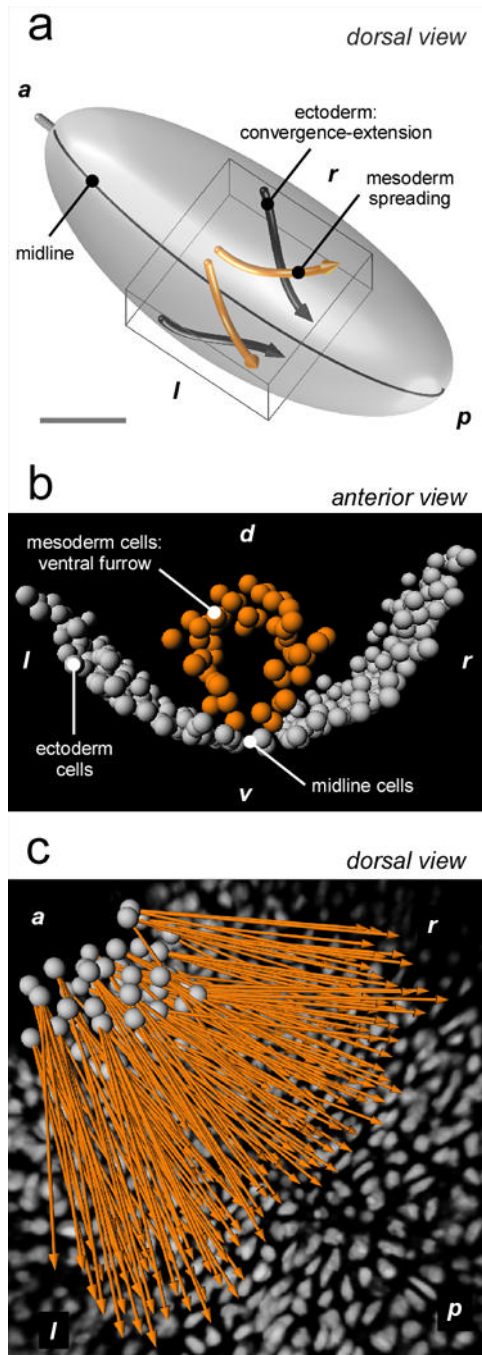


Figure 3. Typical image processing results with Imaris. The 3D schematic representation of the embryo (**A**) shows the position of the imaging field of view (black box), the movements of ectoderm convergence-extension (black arrows) and of mesoderm spreading (orange arrows). The 3D segmentation of the cell nuclei on the ventral side of the embryo at the onset of mesoderm spreading (**B**) shows the cylindrical shape of the ectoderm layer (gray spheres) and the furrow formed by the mesoderm cells (orange spots). The 3D tracking of mesoderm cells (**C**) (gray spots in **C**) and their overall displacement (orange arrows) show the combination of movement toward the posterior direction due to germband extension (GBE) and the angular spreading in the left and right directions. 3D view. Scale: the scale bar in (**A**) indicates 50 μm ; the spots in (**B-C**) are 5 μm diameter. Gray in (**B**): imaging data of ectoderm cells. *a*: anterior, *p*: posterior, *l*: left, *r*: right, *d*: dorsal, *v*: ventral. [Figure 3B is reproduced with permission from (McMahon et al., 2008)].

The quality of the image dataset is critical for the proper tracking of cell movements; any slight improvement of this dataset can drastically improve the image

processing. For instance, as discussed above, the signal level as well as the spatial and temporal resolution is critical for proper nuclear segmentation and tracking (Table 1).

We choose to use Imaris software to perform 3D cell tracking for several reasons. First, the user interface and the 3D visualization of the imaging dataset are extremely efficient. The cell tracks can be visualized, checked and manually corrected using the tracking editor (provided in version 5.7). The Imaris XT interface with Matlab allows improving the functionality of the software without extensive knowledge of computer programming: for instance, the data can be exported into Matlab for further analysis. Together, it appears to be a good compromise option, as it combines the user-friendly interface and standard analysis of commercial software with sufficient flexibility that the user can customize the tools for their applications without the need to write a completely custom software package. Because an improved background knowledge of Imaris software and its functionalities can drastically reduce the time spent performing 3D cell tracking of a large dataset, users should consider obtaining experience from Bitplane user training sessions (contact Bitplane customer service for details).

This protocol describes the tracking of two cell populations during *Drosophila* gastrulation: mesoderm and ectoderm cells. These two groups are defined by sorting the cell trajectories using Imaris functions. The mesoderm cells are those that have invaginated and the ectoderm cells stay at the surface of the embryo. A few midline cells (a sub-population of the ectoderm) are independently tracked and their trajectories are used for spatial registration (see below). The tracking of mesoderm and midline cells is carefully checked so that the trajectories span the entire time sequence.

Tracking Data Registration

The registration is an important step including any spatial or temporal transformation of the datasets that enables their comparison from one experiment to the other. This protocol describes three types of data registration: the correction of motion artifacts, the transformation of the adapted spatial coordinate system, and the synchronization of imaging sequences (Table 1 and Figures 4–5).

In image analysis, different methods of registration exist. For instance, the distribution of specific markers in the sample can be used to correct its drift during time of acquisition (landmark-based spatial registration), or the voxel values of an image sequence can be used to synchronize several datasets [voxel-based temporal registration; (Liebling et al., 2005)]. In this procedure, we used the segmented objects themselves to perform both spatial and temporal registration in a fully quantitative and automated manner. For this reason, the registration is performed after the 3D cell tracking. Under some experimental conditions, spatial registration has to be done before 3D cell tracking; for instance, strong motion artifacts during the image acquisition (embryo rolling, sample or stage drift, etc.) can degrade the cell tracking process.

In this protocol, the spatial registration includes the definition of cell positions in accordance with the body plan. The choice of a spatial coordinate system adapted to the geometry of the tissue or embryo enable the user to investigate complex cell movements in 3D by decomposing their trajectories into components that have a biological meaning. The appropriate coordinate system depends on the biological model used: for instance, during early stages of development, a spherical coordinate system is adapted to the shape of zebrafish (Keller et al., 2008) or *Xenopus Laevis* (Tyszka et al., 2005), whereas a

Cartesian coordinate system remains appropriate for avian embryos (Zamir et al., 2006). In the case of *Drosophila* gastrulation, the embryo has a cylindrical shape in the area where mesoderm spreading occurs (Supplemental Movie 2). The protocol shows first how a cylinder is fitted onto the spatial distribution of ectoderm cells (EctodermCylinderFit.m Matlab script, Supplemental Data 1 and Table 2) in order to identify the anterior-posterior axis of the embryo and to switch from a Cartesian (x, y, z) to a cylindrical (r, θ, z) coordinate system (Figure 4). In this coordinate system, the movements in each direction (radial, angular or longitudinal) can be directly compared from one embryo to the other and correspond to specific morphogenetic events (McMahon et al., 2008).

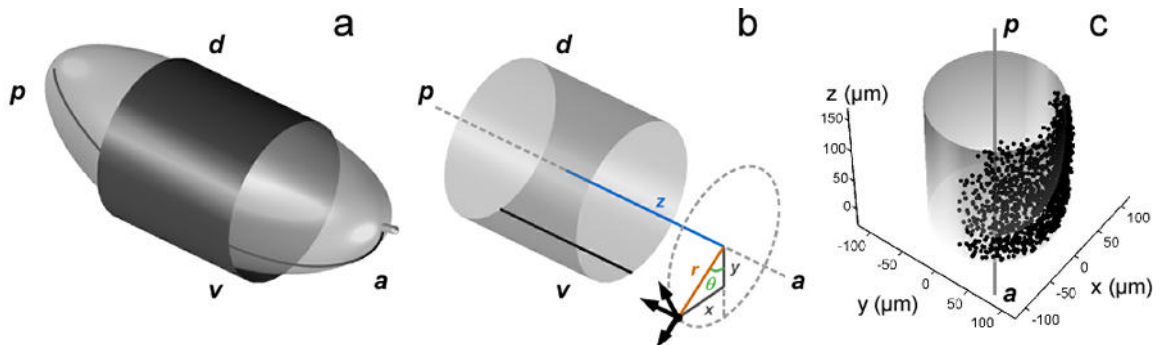


Figure 4. Cylinder fit on the spatial distribution of ectoderm cell positions obtained with EctodermCylinderFit.m script (step 25). The part of the embryo imaged has a cylindrical shape (A) with its main direction aligned with the anterior-posterior direction. The cylindrical coordinate system (B) is obtained after fitting a cylinder on the distribution of ectoderm cells (A and C). After the final registration (step 27), the Cartesian reference frame is rotated and the z -axis is aligned with the anterior-posterior axis of the embryo as in (C). The angular position of the midline (black line in A and B) defines the value $\theta=0$. *a*: anterior, *p*: posterior, *d*: dorsal, *v*: ventral.

The final step of spatial registration is the angular drift correction (Registration.m Matlab script, Supplemental Data 1 and Table 2). During the time of acquisition, the embryo can exhibit some rolling inside its vitelline membrane, corresponding to a solid rotation around the anterior-posterior axis (Supplemental Movies 2–3). This angular drift is corrected by tracking a few cells from the ectoderm midline and defining their angular position at each time point as $\theta=0$ radian (Figure 5A–C).

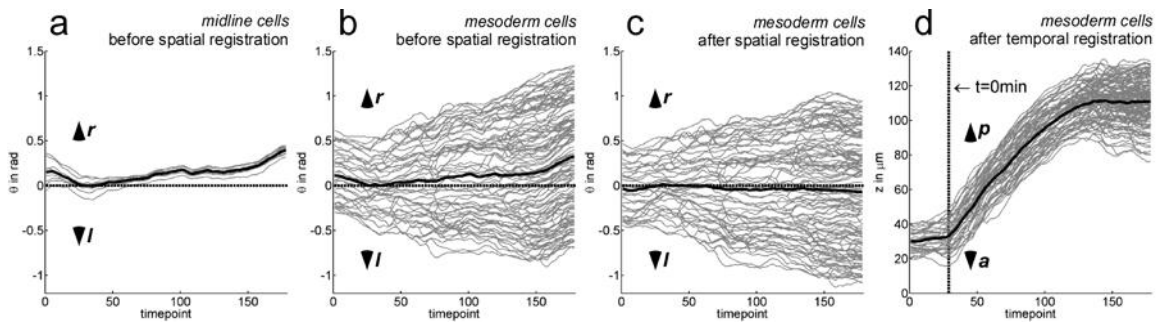


Figure 5. Spatial and temporal registration (step 26 and 27). The Registration.m script subtracts the average angular movement of midline cells (**A**) from the angular movement of mesoderm cells (**B**) to obtain a correction of the angular drift (**C**). After correction, the average angular position of mesoderm cells (black line in b–c) remains close to 0 during the entire spreading process, showing the symmetrical nature of the spreading. The TimeSynchronization.m script identifies the onset of germband extension (GBE, at $t=0$ min) and displays the mesoderm cell movement toward the posterior direction (**D**). The gray lines represent the trajectories of midline cells (A) or mesoderm cells (B–D). The black line is the average trajectory of the cell population. The dashed gray lines in (A–C) show $\theta=0$ rad position. The dashed gray lines (D) shows $t=0$ min position. The timepoints (horizontal axis of the graphs) represent the image number within the sequence; after temporal synchronization these timepoints are converted into minutes. *a*: anterior, *p*: posterior, *l*: left, *r*:right, *d*: dorsal, *v*: ventral. rad: radians.

The temporal registration corresponds to the synchronization of image sequences based on the occurrence of a specific morphogenetic event (TimeSynchronization.m Matlab script, Supplemental Data 1 and Table 2). We choose the onset of germband extension (GBE) (Irvine and Wieschaus, 1994; Bertet et al., 2004) as the time reference to synchronize the sequences and define $t=0$ min (Figure 5D). At this time, both ectoderm and mesoderm cells start to move toward the posterior direction (McMahon et al., 2008).

It is important to notice that the references used for spatial and temporal registration are identical among embryos and are not disrupted in mutants. Hence, they depend on the model system studied. In this protocol, the estimation of the AP axis using the shape of the ectoderm layer, the angular reference $\theta=0$ rad using the ectoderm midline cells, and the time synchronization based on the onset of GBE are independent of the mesoderm spreading process. In addition, we used these references for registration because they are not disrupted in the mutant we studied (McMahon et al., 2008).

Tracking Data Analysis

Once the tracking data are registered, the cell trajectories can be analyzed directly and compared from one embryo to the other. We provide two examples of tracking data analysis useful to study complex 3D movements of cell migration and to quantify the collective nature of this process: decomposition of cell trajectories along each cylindrical direction (Figure 6) using MovementDecomp.m Matlab script (Supplemental Data 1 and

Table 2) and mesoderm spreading analysis (Figure 7) using SpreadingAnalysis.m Matlab script (Supplemental Data 1 and Table 2).

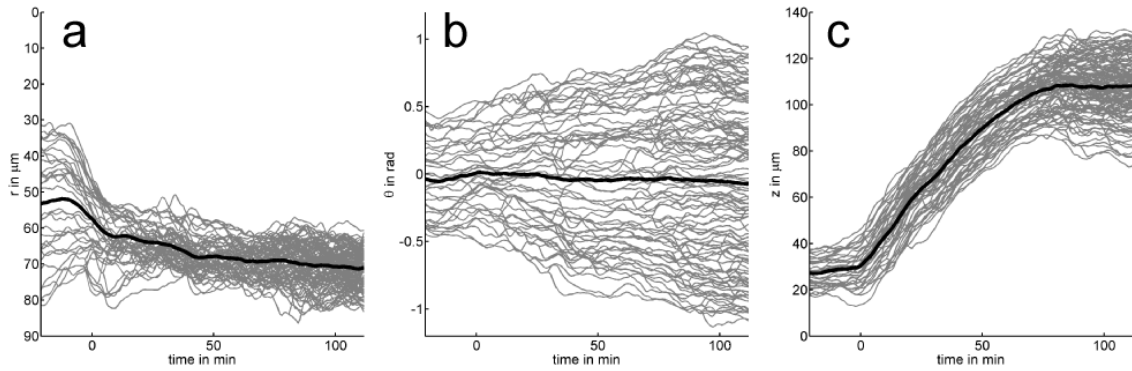


Figure 6. Decomposition of mesoderm cell movements into their cylindrical components using MovementDecomp.m (step 28A). This script displays the three graphs $r(t)$ (A), $\theta(t)$ (B), and $z(t)$ (C): the gray lines represent the trajectories of mesoderm cells along each cylindrical direction after spatial and temporal registration. The black line is the average trajectory of the cell population. See Anticipated Results for details. rad: radians.

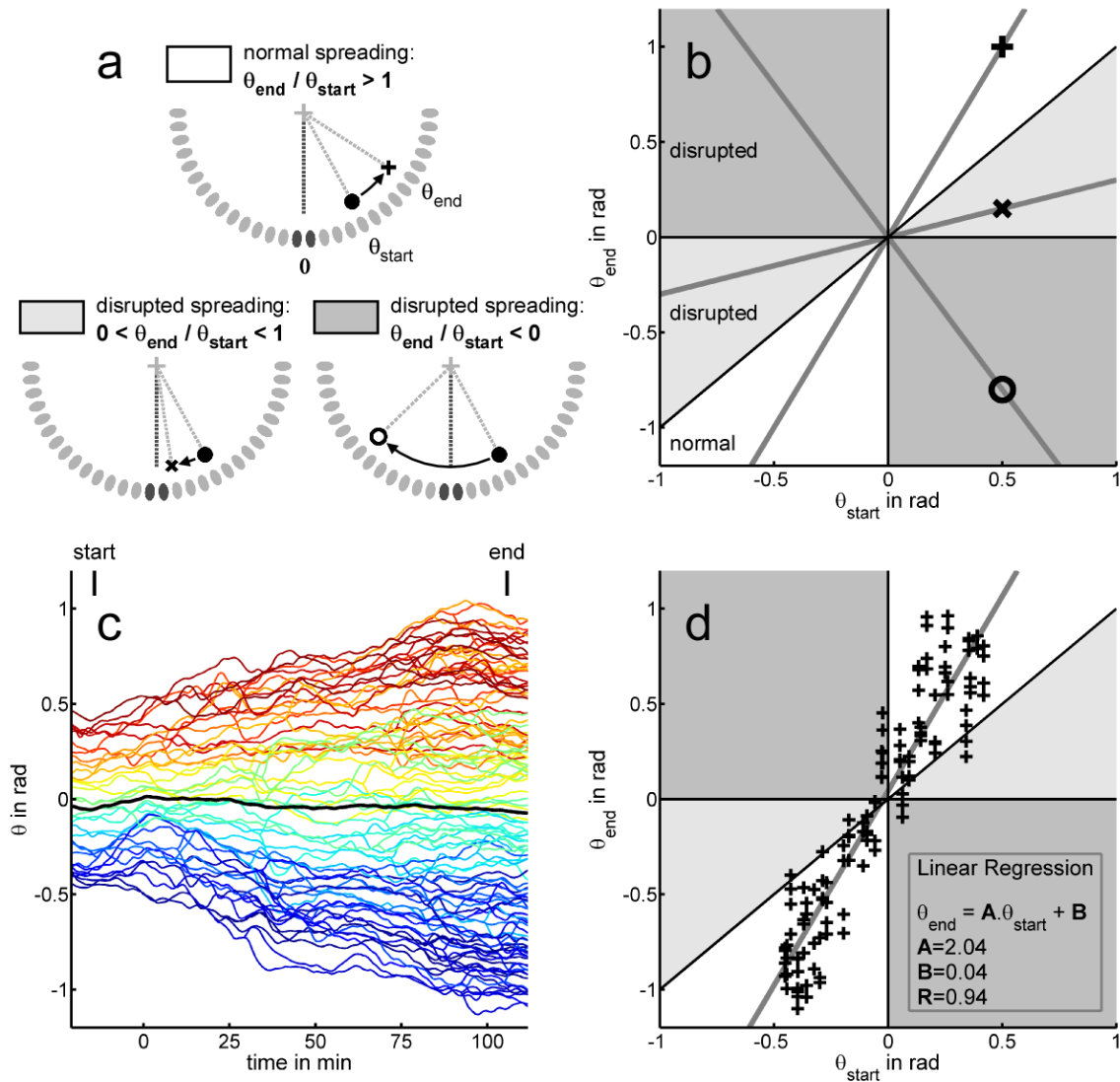


Figure 7. Analysis of mesoderm cell spreading using SpreadingAnalysis.m (step 28B). **(A)** Three specific cell movements are identified. Firstly, a cell moving from θ_{start} to θ_{end} (angular positions at the onset and at the end of the process, respectively) with $\theta_{\text{end}} / \theta_{\text{start}} > 1$ corresponds to a normal spreading behavior (white area). In this case, the cell (+ sign) is moving on top of the ectoderm layer (gray ovals), further away from the midline position (black ovals, $\theta=0$ position). A disrupted spreading (light gray area) with cells moving toward the midline (x sign) corresponds to $0 < \theta_{\text{end}} / \theta_{\text{start}} < 1$. Finally, the most disrupted behavior (dark gray area) corresponds to a cell crossing the midline (o sign) and moving on the opposite side of the embryo with $\theta_{\text{end}} / \theta_{\text{start}} < 0$.

These three behaviors correspond to three different areas of the $\theta_{\text{end}}(\theta_{\text{start}})$ graph (**B**): white, light gray, and dark gray, respectively. The movement of each cell is represented by a point on this graph and the slopes of the gray lines is the $\theta_{\text{end}} / \theta_{\text{start}}$ in each case (normal spreading, + sign and disrupted movements, x and o signs). This representation is used by the script to analyze the spatial organization of the cell movements in the angular direction. It first displays $\theta(t)$ for each cell with a color coding for the angular position at the onset of the furrow collapse (**C**) and the $\theta_{\text{end}}(\theta_{\text{start}})$ graph (**D**). The experimental data obtained from a wild-type embryo (+ signs in D) are mainly located in the white area of the graph, corresponding to a normal spreading. This distribution is analyzed using a linear regression as described in Anticipated Results. The result of the regression is displayed on the graph (gray line and values A, B and R, see Anticipated Results for details). rad: radians. [Figure 7D is modified with permission from (McMahon et al., 2008)].

Table 2. Description of the customized Matlab scripts contained in Supplementary Data 1.

Matlab script name	Description
<i>Imaris2xyzt.m</i>	Converts the tracking data exported by ImarisXT Object Manager into x, y, z, t matrices. x(i,j), y(i,j), z(i,j), and t(j) are the spatial cartesian coordinates in micrometers and the time in minutes of each cell i at each time point j. i and j are integers. In case the tracking data appear noisy (i.e., trajectories with small movements at high frequency), this script can smooth them in time by using a 5-point Loess quadratic fit applied to each spatial component. Requires Imaris tracking files (Mesoderm.mat, Ectoderm.mat or Midline.mat) and stores the results in Mesodermxyzt.mat and Ectodermxyzt.mat or Midlinexyzt.mat files, respectively.
<i>EctodermCylinderFit.m</i>	Fits a cylinder on the distribution of ectoderm cell positions. Estimates the direction (CylDirection), the center (CylCenter) and the radius (CylRadius) of the cylinder. Requires Ectodermxyzt.mat and stores the result into the file CylFitResult.mat.
<i>TimeSynchronization.m</i>	Estimates j0, the time point for which t=0 min as the onset of GBE by checking the mesoderm cell movements toward the posterior direction. Requires Mesodermxyzt.mat and CylFitResult.mat and stores j0 in the j0.mat file.
<i>Registration.m</i>	Spatial and temporal registration of the tracking data. Registers the time matrix t by using the j0 value. Rotates in 3D the Cartesian reference frame using the cylinder fit result so that the z-axis is aligned with the embryo anterior posterior direction (main axis of the cylinder). In this frame, the new Cartesian components x, y, and z can be directly converted into the cylindrical components r, θ , and z using the cart2cyl.m function from geom3d toolbox. An additional rotation of the frame along the anterior-posterior axis creates the mesoderm cell angular positions θ in the $[-\pi/2, \pi/2]$ range using cart2cyl0.m

	<p>function. Corrects the angular drift of mesoderm cells using the midline tracking data. Requires Mesodermxyzt.mat, Midlinexyzt.mat, CylFitResult.mat and j0.mat. Stores the registered mesoderm cell tracking data (xReg, yReg, zReg, and tReg matrices) into the MesodermReg.mat file.</p>
<i>MovementDecomp.m</i>	<p>Loads the MesodermReg.mat file and converts the Cartesian coordinates into the Cylindrical coordinates. Plots the time variation of each component ($r(t)$, $\theta(t)$, and $z(t)$) for each cell into three graphs as displayed in Figure 6. Requires MesodermReg.mat file.</p>
<i>SpreadingAnalysis.m</i>	<p>Loads the MesodermReg.mat file and converts the Cartesian coordinates into the Cylindrical coordinates. Displays $\theta(t)$ for each cell with a color coding for the angular position at the onset of the furrow collapse, as in Figure 7c. Identifies this timepoint (j_{start}) as the time when the furrow has a cylindrical shape. Displays the angular position at the end of the spreading θ_{end} (defined as 120 minutes after j_{start}) depending on the angular position at the onset θ_{start} (at j_{start}) for each cell. Performs a linear regression on the distribution of the points in this graph and the result is displayed on it as in Figure 7d). Requires MesodermReg.mat file.</p>
<i>Browse.m</i>	<p>Browse function.</p>
<i>cart2cyl0.m</i>	<p>Converts cartesian to cylindrical coordinates. This function is similar to cart2cyl.m from the geom3d toolbox but return θ in $[-\pi, \pi]$, instead of in $[0, 2\pi]$.</p>

Advantages and limitations of this protocol to investigate in vivo cell migration

There are number of protocols available to investigate cell migration in tissue cultures or in model organisms [see (Guan, 2005) for instance]. Here we discuss the advantages and specificity of this protocol for studying cell migration *in vivo*:

(i) The cells are imaged in challenging conditions: they move fast and deep inside a scattering and photo-sensitive embryo. Hence, we describe here an optimized imaging approach.

(ii) Most studies of cell migration are limited to 2D in space and to cells migrating on a fixed substrate; however, inside a living organism, it usually occurs in 3D, with the simultaneous combination of different movements. This protocol shows how to investigate such complex movements in 3D by choosing the appropriate spatial coordinate system and decomposing the cell trajectories into meaningful components. In this study, the mesoderm cells migrate on a moving cell layer (ectoderm): we recently demonstrated that the data generated by this protocol allowed us to investigate the mechanical coupling between two cell layers and to decouple their movements (McMahon et al., 2008).

(iii) During embryonic development, cells rarely migrate alone but more often as a collective. The method for tracking a large cell population described in this protocol allows for simultaneous observation of individual and collective behaviors, both of migrating and non-migrating cells. This approach allows the investigator to evaluate migration with a statistical analysis and to identify variability within the population (McMahon et al., 2008). By following a limited number of cells using techniques such as

local photo-activation, one can focus on specific behaviors that are not representative of the collective.

(iv) Whereas many studies analyze the cell tracking results using a qualitative or manual approach, we provide a quantitative and automated analysis of cell trajectories. In this protocol, the spatial and temporal registration of the data enables the investigator to quantitatively compare one experiment to the other, to test the reproducibility between embryos and to quantify mutant phenotypes (McMahon et al., 2008). In addition, the statistical analysis of cell trajectories presented here illustrates how to quantify the collective nature of a cell migration process.

(v) Sophisticated quantitative imaging of cell movements usually involves fully custom-designed approaches that are difficult to implement or modify by other laboratories without strong expertise (Keller et al., 2008). This protocol uses commercially available equipment and software and provides customized Matlab scripts that are annotated and simple enough to be used and modified with minimum expertise. Imaris, the commercial software used to perform 3D cell tracking is extremely user-friendly; its interface ImarisXT, can be used with classic programming languages and image processing software, such as Matlab or ImageJ, enabling a user with minimum skills in programming to improve the functionality of Imaris for specific scientific applications. Together, these aspects make this protocol possible to implement, modify, or extend in a biology laboratory without extensive expertise in microscopy or computer science.

This protocol has two main limitations. First, cell migration is investigated by only tracking the cell nuclei. Although this approach can already generate a lot of

biological insights, the analysis of other cell features, such as cell shape changes, can be required for specific studies. In the case of mesoderm spreading in *Drosophila*, the challenging scattering conditions (see above) strongly limit the imaging of structures other than nuclei, such as cell membranes. The second limitation concerns the 3D cell tracking: the fluorescent signal from the deepest nuclei is weak and their segmentation and tracking requires manual correction. This step, which is not fully automated, limits the number of cells segmented per experiment. For this reason, we limited our application of this protocol to ~100,000 segmented cell positions per embryo (including ectoderm and mesoderm cells). To increase this number, further improvement of imaging quality and/or of image segmentation/tracking strategy would be required. The subsequent computer analysis of cell trajectories provided here is automated and is not limited by the cell number.

MATERIALS

REAGENTS

- *Drosophila* transgenic line with an ubiquitous expression of Histone A-GFP fusion protein (Bloomington *Drosophila* Stock Center, stock number 5941) and *klarsicht* mutant strain from Bloomington *Drosophila* Stock Center, stock number 3256)
- Halocarbon Oil 27 (Sigma, cat. no. H8773)
- Heptane (EMD, cat. no. HX0080)
- 50% (v/v) Bleach (Clorox) or Sodium hypochlorite (Reagent grade, Sigma, cat. no. 239305) **! Caution Bleach is poisonous. Wear personal protection, such as gloves and goggles.**
- Glacial acetic acid (VWR, cat. no. MK312146)
! Caution Acetic acid is corrosive. Handle with gloves.
- Ethanol (Sigma-Aldrich, cat. no. 459836)
! Caution Ethanol is flammable.
- UltraPure Agarose (Invitrogen, cat. no. 15510-019)
- Apple juice (generic brand)
- Sucrose (generic brand)

EQUIPMENT

- Paintbrush (small brush size: 3/0 White Sable Robert Simmons)
- Double-sided sticky tape (TESA)
▲ CRITICAL if another brand is used, ensure the glue is not toxic for the embryos.

- Coverslips (22x22mm, No1, VWR, cat. no. 48366 067)
- 35x10mm dishes (BD Falcon, cat. no. 353001)
- 60x15mm dishes (BD Falcon, cat. no. 353002)
- 2PEF Microscope: Zeiss LSM 510 with Chameleon Ultra Laser (Coherent Inc)
- C-Apochromat 40X/1.1 N.A. W Corr UV-VIS-IR (Carl Zeiss Inc) objective.
- Software: Imaris 5.7 with ImarisTrack, Imaris MeasurementPro, and ImarisXT modules (Bitplane) and Matlab 7.7 (The MathWorks).
- Computer: 3.0 GHz Dual-Core Processor, 16 Gb DDR RAM, Large SATA Hard Drive (> 100 Gb, faster than 7000 rpm)
- 1 L glass bottles and 25 ml plastic pipettes.
- Optional: Thumbtack/Needle
- Small basket to handle the embryos. One can use: 100 μm - cell strainers (BD Falcon, cat. no. 352360)
- Standard dissecting microscope

REAGENT SETUP

Apple juice plate: Dissolve 22 g of sucrose in 350 ml of H₂O and pour it into a 1 L bottle. Add 7 g of agarose into this bottle, mix by vigorous shaking. Microwave first for 2 min, and then 2 times for 1 min, mixing the solution in between.

▲ **CRITICAL** the agarose solution must boil in the microwave.

Put aside to cool to approximately 60°C. Add 10 ml of ethanol and 5 ml of glacial acetic acid to the solution. Add 50 ml of apple juice and mix well. Pipette into 35 x 10 mm

dishes (~60 plates/preparation) using 25 ml plastic pipette or syringe. The plates can be stored in a container at 4°C for weeks.

! Caution Acetic acid is corrosive. Handle with gloves.

! Caution Ethanol is flammable.

Agarose plate: Dissolve 30 g of sucrose in 350 ml of H₂O and pour it into a 1 L bottle. Add 10 g of agarose to the bottle, mix by vigorous shaking. Microwave first for 2 min, and then 2 times for 1 min, mixing the solution in between.

▲ CRITICAL the agarose solution must boil in the microwave.

Put aside to cool to ~60°C. Pipette into 60 x 15 mm dishes (~20 plates/preparation) using a 25 ml plastic pipette or syringe. The plates can be stored in a container at 4°C for weeks.

EQUIPMENT SETUP

Preparation of coverslips coated with glue for embryo imaging. Add short pieces (5-10 cm) of double-sided tape to a 200 ml glass bottle. Add heptane to cover the pieces of tape (typically 50 ml for 50 cm of tape). Gently shake the bottle at least overnight at room temperature (18–25 °C) to dissolve the glue. The heptane-glue bottle can be stored at room temperature for months. Prepare coverslips coated with glue at least 10 min before using them. Add a 60–100 µl droplet of heptane-glue to the middle of each coverslip and allow to dry for 10 min. The coated coverslips can be stored for a few days at room temperature in a box to protect them from dust.

Microscope settings for live imaging (Zeiss LSM 510). Most of our imaging datasets have been acquired using a Zeiss LSM 510 microscope and a Chameleon Ultra

femtosecond laser. However, the protocol can be accomplished with any similar 2PEF microscope. The embryos were imaged using C-Apochromat 40X/1.1 N.A. W Corr UV-VIS-IR (Carl Zeiss) objective at 940 nm. The non-descanned pathway is used with a single short-pass filter (KP680nm) to cut out the laser light. 200 x 200 x 80 μm^3 3D-stacks with 0.5 x 0.5 x 1 μm^3 voxel size and 1.9 μs pixel dwell time were acquired every 45–50 seconds for ~3 hours.

LSGE and geom3D toolboxes for Matlab processing. The Matlab processing requires two freely available toolboxes: the Least Squares Geometric Elements (LSGE) library and the geom3d toolbox. The LSGE library was developed by the Centre for Mathematics and Scientific Computing (National Physical Laboratory, UK) and is available from the EUROMETROS website (http://www.eurometros.org/gen_report.php?category=distributions&pkey=14). The geom3d toolbox was developed by David Legland and is available from Matlab Central website (<http://www.mathworks.com/matlabcentral/fileexchange/8002>). Download the files, save the “lsge-matlab” and “geom3D” folders and their content on your computer and add both of them in the Matlab path (using “File/Set Path” from the Matlab menu).

Customized Matlab scripts. Download the Matlab scripts from the supplemental section of this protocol (Supplementary Data 1). Unzip the corresponding file and place all contained files (Imaris2xyzt.m, EctodermCylinderFit.m, TimeSynchronization.m, Registration.m, MovementDecomp.m, SpreadingAnalysis.m, Browse.m, and cart2cyl0.m) in the same folder. The customized Matlab scripts included here are designed and annotated in order to allow the user to run and modify them with only basic knowledge of Matlab programming. However, to further manipulate the data, a working

knowledge of Matlab is required. Table 2 provides a list of the scripts and their description.

Sample tracking data files. In order to run the Matlab processing and start the procedure at step 23 without an imaging dataset, we provide sample tracking data files. Download the files from the supplemental section of this protocol (Supplementary Data 2). Unzip the corresponding file and place all of the files (Mesoderm.mat, Ectoderm.mat, and Midline.mat) in the same folder as the Matlab scripts.

PROCEDURE

Embryo Preparation • **TIMING** 4 h per set of embryos for imaging

- 1| Grow flies in standard culture bottles (the generation time is ~10 days at 25°C; see http://flystocks.bio.indiana.edu/Fly_Work/culturing.htm for details).
- 2| Transfer the flies into a collection bottle and add an apple juice plate [see Reagent Setup and standard procedure in (Greenspan, 2004)].
- 3| Collect the embryos after 2-3 h of laying at 25 °C.
- 4| Add a few droplets of halocarbon oil on the embryos to make the chorion translucent, stage the embryos (Hartenstein, 1993), and select ~10-20 stage 5 embryos. Embryos reach stage 5 after 2-3 h of development. This stage is easily identified by looking at the transparent layer of cellularizing cells at the embryo periphery (see <http://flymove.uni-muenster.de/> for pictures of stages).
- 5| Dechorionate the embryos using either option A Dechoriation with bleach or option B Dechoriation with a needle, depending on the user preference and ability.

(A) Dechoriation with bleach

- (i) Transfer the embryos into a basket with a paintbrush.
- (ii) Remove the oil from the bottom with a paper towel.
- (iii) Rinse the embryos with a few milliliters of water.
- (iv) Soak the basket in fresh 50% bleach (vol/vol) and control the dechoriation by looking at the embryos under a dissecting microscope. When the first bubble appears between the chorion and the vitelline membrane of any embryo, immediately proceed to step v (should take 10-40 sec).
- (v) Rinse the basket with copious amounts of water to remove the bleach.

- (vi) Remove the water from the bottom with a paper towel.

▲ **CRITICAL STEP** do not over-bleach the embryos to ensure their viability and normal development.

(B) Dechoriation with needle

- (i) Prepare a microscope slide with double-sided tape on one side of it.
- (ii) Transfer the embryos into a basket with a paintbrush.
- (iii) Remove the oil from the bottom with a paper towel.
- (iv) Rinse the embryos with a few milliliters of water.
- (v) Transfer embryos to the sticky tape on the slide prepared in step 5 Option B(i).
- (vi) Use a needle or thumbtack to gently tear the chorion open.
- (vii) Use a paintbrush to gently remove the embryo from chorion [see video step 7 in (Reed et al., 2009) for details].

▲ **CRITICAL STEP** after dechoriation, the embryos are more fragile, therefore they should only be gently manipulated. Minimize the time they spend in the air without water.

6| Gently transfer the embryos onto an agarose plate (see Reagent Setup). Once placed on this plate, the water content of the agarose gel prevents them from drying.

7| Align and orient the embryo dorsal side up in the center of the agarose plate.

▲ **CRITICAL STEP** from step 6 to step 8, the embryos have to be kept as clean as possible: any piece of chorion, dust, or agarose sticking to their surface can have a large negative impact on the imaging quality.

? TROUBLESHOOTING

- 8| Cut the central piece of agar and transfer it under a dissecting scope.
- 9| Gently stick the embryos to a coverslip coated with glue (see Equipment Setup) by bringing the coverslip glue-side down towards the embryos until they just touch the coverslip. Turn over the coverslip and add a water droplet on top of them.

▲ **CRITICAL STEP** be careful not to crush the embryos with the coverslip.

4D-Imaging • TIMING 3h per imaging acquisition

- 10| Using an inverted Zeiss LSM microscope, add a water droplet onto the long working distance water objective. Place the coverslip (from step 9) under the microscope with the embryos facing the objective. Bring the embryos into focus using brightfield transmitted illumination to avoid any bleaching of GFP.
- 11| Adjust the femtosecond laser to 940 nm wavelength. Adjust the mean power to a level no higher than ~20 mW at the objective focus (use a power meter to check it).
- 12| Choose a well-oriented embryo at early stage 6 with the ventral furrow facing the objective, in the middle of the field of view. Adjust the position and field of the acquisition. Use a 200 μm x 200 μm square field in the center of the embryo (Figure 3a and Supplemental Movie 2). Select the appropriate spatial and temporal sampling as discussed in the introduction: typically 0.5 μm per pixel in x and y, and 1 μm in z; 45-50 seconds of time between each z-stack including 10 sec of resting time. Adjust the number of z-slices to image such that data is acquired from the most ventral ectoderm cells to the expected position of the most dorsal mesoderm cells when the ventral furrow is fully formed (typically 80 μm z-stack).

- 13| Adjust the photomultiplier tube (PMT) gain to avoid any saturation of the fluorescent signal from the mesoderm cells at every z-position. Saturation occurs when the signal detected causes the pixel to reach its maximum value (255 for a 8bit-image). There will be some saturation in the fluorescent signal from the ectoderm.
- 14| Run the time-lapse acquisition for 3 h at 25 °C. Monitor the temperature during acquisition: it is critical as the speed of development is highly sensitive to the temperature (development proceeds at rate approximately twice as fast at 25 °C compared to 18 °C).

■ PAUSE POINT Store the acquisition data until use. The rest of the protocol can be paused at any time.

? TROUBLESHOOTING

- 15| Repeat steps 1-15 several times in order to obtain a good imaging dataset (i.e., no phototoxicity, good orientation, good signal-to-noise ratio, correct time and spatial window, a sufficient number of cells staying within the field of view).

3D Cell Tracking • TIMING weeks

- 16| Load and visualize the imaging datasets in 3D using Imaris. Select a good data set (see step 15) and crop it in time and space to focus on the useful time and spatial window. Verify the spatial calibration (size of voxels in micrometers/pixel) corresponds to your microscope calibration. Save the file as EmbryoSequence.ims

▲ CRITICAL STEP In order to perform the 3D cell tracking efficiently and reduce the time spent to do it, extensive knowledge of Imaris software is recommended. The user is

invited to follow Bitplane user training sessions or to contact Bitplane customer service for further information.

? TROUBLESHOOTING

17| Segment nuclear position using Imaris spot detection: adjust the size to 4–5 μm .

? TROUBLESHOOTING

18| Track the cell movements using Imaris spot tracking. Use “autoregressive motion” option with gap size set to 2 as the scripts provided to analyze the data are not designed for a larger gap.

19| Sort and manually correct the tracks using the Tracking Editor, so that each track is complete from the beginning to the end of the sequence. However, keep in mind that the scripts provided to analyze the data handle only one-branch tracks, meaning that each track has a maximum of one spot per time point (see annotations in Matlab scripts for details, Supplementary Data 1). This is a concern since after a cell division only one daughter will acquire the initial track sequence. Manual correction is required. First, detect the cell divisions manually. Subsequently, duplicate each track before a cell division so that each daughter cell has its own track from beginning to end.

20| Complete the tracking data using manual spot detection and tracking. Save the scene file as EmbryoSequence.imx

21| Perform steps 17–20 successively for mesoderm cells, ectoderm cells and a few cells (typically 8) from the midline. Use Imaris functions to select the tracks from the corresponding subpopulation of cells. The midline cells can be visually discerned and tracked manually (Supplemental Movie 3). Because the ectoderm is only used

as a reference, the tracks from the ectoderm do not need to be complete (i.e. not all tracks have to go from beginning to end and some cells can be missing) for the subsequent analysis: typically 50% of cells tracked representing the ectoderm movement is sufficient. No need to identify the daughter cells after division in this case.

? TROUBLESHOOTING

- 22| Export the tracking data using ImarisXT Object Manager into 3 different files: Mesoderm.mat, Ectoderm.mat and Midline.mat

Tracking Data Registration • TIMING 1h

- 23| Place the tracking data files (Mesoderm.mat, Ectoderm.mat and Midline.mat) in the same folder as the customized Matlab scripts (Supplementary Data 1 and Table 2). One can start the procedure at this step using the sample tracking data files provided in the supplementary section of this protocol (Supplementary Data 2).
- 24| Convert Imaris tracking files into x, y, z, t matrices using Imaris2xyzt.m Matlab script. This script outputs x(i,j), y(i,j), z(i,j), and t(j), with i and j the cell number and the time point, respectively. x, y are the image plane coordinates, z the axial direction of imaging and t the time. Enter the t_{sequence} , the time calibration (time delay between z-stacks). This script checks errors in the tracking dataset: if required, correct the tracking in Imaris and recheck for errors (see script annotations for details). Run the script for each Imaris tracking file (Mesoderm.mat, Ectoderm.mat and Midline.mat). Output: Midlinexyzt.mat, Mesodermxyzt.mat and Ectodermxyzt.mat.

- 25| Fit a cylinder on the 3D distribution of ectoderm cell positions (Figure 4) using the EctodermCylinderFit.m Matlab script.
- 26| Synchronize the sequences based on the onset of GBE (Figure 5D) using the TimeSynchronization.m Matlab script.
- 27| Perform the final registration (Figure 5A-C) of the tracking data using Registration.m Matlab script. The registered mesoderm cell tracking data (xReg, yReg, zReg, and tReg matrices) are saved into the MesodermReg.mat file.

Tracking Data Analysis • TIMING 1h

- 28| A number of different analyses can be performed after tracking data registration (McMahon et al., 2008). For example, to decompose the cell trajectories into their cylindrical components use Option A below. To perform a statistical analysis of the mesoderm cell migration and quantify its collective nature, use option B.
 - (A) **Display the tracking data** using MovementDecomp.m Matlab script (Figure 6).
 - (i) Run MovementDecomp.m Matlab script and follow the instructions. The mesoderm cell 3D trajectories are decomposed along each cylindrical coordinate ($r(t)$, $\theta(t)$, and $z(t)$) as displayed in Figure 6.
 - (B) **Analyze the mesoderm cell spreading** using SpreadingAnalysis.m (Figure 7).
 - (i) Run SpreadingAnalysis.m and follow the instructions. It displays the spreading analysis of mesoderm cells: spatial organization as in Figure 7c and $\theta_{\text{end}}(\theta_{\text{start}})$ graph with the the statistical analysis results as in Figure 7d.

TIMING

Steps 1-9, **Embryo Preparation**: 4 h per set of embryos for imaging.

Steps 10-15, **4D Imaging**: 3 h per imaging acquisition. Repeat steps **1-15** several times to obtain 3-4 correct imaging datasets: ~1 week.

Steps 16-22, **3D Cell Tracking**: several weeks per imaging dataset depending on the quality of the dataset and on the efficiency of the user to perform the tracking correction with Imaris.

Steps-23-27, **Tracking Data Registration**: 1 h maximum per dataset.

Step 28, **Tracking Data Analysis**: 1 h maximum per dataset.

ANTICIPATED RESULTS

The imaging and the 3D cell-tracking (steps 1–22) should result in the visualization of mesoderm and ectoderm cell distributions (Figure 3B and Supplementary Movie 1) and the spreading movement of mesoderm cells during gastrulation (Figure 3C). An example 4D imaging dataset is available within published work (McMahon et al., 2008).

The results of tracking data registration (steps 23–27) obtained with the sample tracking data provided in supplemental section of this protocol (Supplementary Data 2) are displayed in Figures 4–5. First, the ectoderm cell positions are fitted onto a cylinder using `EctodermCylinderFit.m` script (step 25), which displays the distribution of a selected number of ectoderm cells on an estimated cylinder as in Figure 4C. The time synchronization using `TimeSynchronization.m` script (step 26) shows the movement of the mesoderm cells toward the posterior direction and estimates the time point at which the onset of movement occurs (Figure 5D). The `Registration.m` script (step 27) displays the angular movements of mesoderm cells before and after angular drift correction, as in Figure 5A–C.

After the tracking data registration, the decomposition of mesoderm cell movements into their cylindrical components $r(t)$, $\theta(t)$, and $z(t)$ using `MovementDecomp.m` script (step 28A) should result in the three graphs of Figure 6. Each of these graphs corresponds to a specific morphogenetic event: (i) $r(t)$ shows the furrow collapse with the cells moving toward the periphery of the embryo (Figure 6A); (ii) $\theta(t)$ shows the angular spreading of the mesoderm cells with movements toward the left and right directions (Figure 6B); (iii) $z(t)$ shows the movement of GBE with a concerted movement toward the posterior direction (Figure 6C).

The analysis of mesoderm spreading using SpreadingAnalysis.m (step 28A) should display the two graphs of Figure 7C and Figure 7D. The first graph displays $\theta(t)$ for each cell with a color coding for the angular position at the onset of furrow collapse. It shows that the angular distribution of the mesoderm cells is maintained over the two hours of mesoderm spreading (Figure 7C). The $\theta_{\text{end}}(\theta_{\text{start}})$ graph (Figure 7D), is used to investigate the collective migration of mesoderm cells during their spreading. The position of each cell in this graph corresponds to a specific movement behavior detailed in (Figure 7A-B). When $\theta_{\text{end}}/\theta_{\text{start}} > 1$ (white areas in the graphs), the cells are spreading normally. If $0 < \theta_{\text{end}}/\theta_{\text{start}} < 1$ (light gray areas in the graphs), the cells are not spreading and move in the opposite direction, toward the midline. If $\theta_{\text{end}}/\theta_{\text{start}} < 0$ (dark gray areas in the graphs), the cells are not spreading, cross the midline and move to the opposite side of the embryo. In wild-type embryos, the cells position in the $\theta_{\text{end}}(\theta_{\text{start}})$ graph are mainly distributed in the white area (Figure 7D). In addition, they tend to be aligned along a specific line: a linear regression gives an estimation of the slope of line (A) and of the correlation coefficient (R) (Figure 7D). As previously reported, A and R values should be close to 2 and 1, respectively (McMahon et al., 2008). This statistical analysis provides a quantitative tool for investigating the collective behavior exhibited by mesoderm cells during their spreading. The behavior is quantitatively defined as the spreading strength A, which corresponds to the typical value of $\theta_{\text{end}}/\theta_{\text{start}}$. The collective nature of the process is quantified by R: a value close to 1 demonstrates the spreading behavior $A = \theta_{\text{end}}/\theta_{\text{start}}$ is shared by the entire cell population, as in wild-type embryos; a lower value means the cell spreading is disrupted, as in mutants. This quantitative analysis has been used to demonstrate (i) the reproducibility of the collective behavior in

wild-type embryos and (ii) the disruption of the process and the identification of different cell populations in a mutant embryo (McMahon et al., 2008).

The procedure described in this chapter details every experimental step from the preparation of embryos for imaging to the quantitative analysis of mesoderm cell spreading. In addition to this analysis (step 28), the cell movements can be analyzed in whatever manner a user finds interesting by developing their own customized Matlab scripts to analyze the registered data (step 27).

Chapter 3:

Dynamic Analyses of *Drosophila* Gastrulation

Provide Insights into

Collective Cell Migration*

*This chapter, published in *Science* in 2008, was written by Amy McMahon, Willy Suppato, Scott E. Fraser, and Angela Stathopoulos

ABSTRACT

The concerted movement of cells from different germ layers contributes to morphogenesis during early embryonic development. Using an optimized imaging approach and quantitative methods we analyzed the trajectories of hundreds of ectodermal and mesodermal cells, following internalization within *Drosophila* embryos over two hours during gastrulation. We found a high level of cellular organization, with mesoderm cell movements correlating with some but not all ectoderm movements. The mesoderm population underwent two ordered waves of cell division and synchronous cell intercalation. In addition, cells comprising its leading edge stably maintained their positions during migration. FGF signaling guides mesodermal cell migration, however we found some directed dorsal migration in an FGF receptor mutant, suggesting additional signals are involved. Thus, decomposing complex cellular movements can provide detailed insights into collective cell migration.

INTRODUCTION

An embryo is shaped by a complex combination of collective cell movements, resulting in cell diversification and tissue formation (Stern, 2004; Lecaudey and Gilmour, 2006; Montell, 2006; Rorth, 2007). The majority of these morphogenetic events are dynamic and involve the simultaneous execution of different movements, with large populations of cells moving in three-dimensional space, deep inside the embryo (Lecaudey and Gilmour, 2006; Rohde and Heisenberg, 2007). Gastrulation is the earliest morphogenetic event involving massive cellular migration of the germ layers (Leptin, 2005). Because it is technically challenging to image individual cell movements inside an embryo without compromising viability, studies of mesoderm cell movements during gastrulation in *Drosophila* have relied on the extrapolation of dynamical events from observations of fixed embryos (see Figure 1A and 1B) or from in vivo descriptions of small numbers of cells (Schumacher et al., 2004; Wilson et al., 2005; Murray and Saint, 2007).

MATERIALS AND METHODS

Fly Strains and Genetics

All crosses and strains were maintained at 25°C. The following lines were obtained from Bloomington: His2AV-GFP; *htl*^{AB42}/TM3; *klar*¹; Dr/TM3, P(Dfd-GMR-nvYFP)3, Sb¹. His2AV-GFP was recombined with *htl*^{AB42} and *klar*¹ using conventional

methods. His2AV-GFP, *klar*¹, *htl*^{AB42} flies were maintained over a Dfd-GMR-YFP balancer. Wild-type refers to *yw* mutants or His2AV-GFP in a *yw* background.

Fixation for Antibody staining

Embryos were dechorionated for 3 minutes in bleach and washed thoroughly with 0.1% Triton NaCl and distilled H₂O. Embryos were fixed in 50% Heptane, 4% Formaldehyde, 0.25M EGTA, and PBS for 20 minutes. Vitelline membranes were removed by vigorous shaking of embryos in Methanol.

Antibody staining and Sectioning of Embryos

Color substrate staining was performed using the VectaStain kits (Vector). Embryos were blocked in 1.5% goat serum in PBS for 30 minutes. Primary antibodies were added overnight at 4°C. Guinea pig anti-Twist antibody (kind gift of Mike Levine, UC Berkeley) was used at 1:300 and secondary antibodies from the kit were used at 1:200. Sectioning was performed according to previous methods (Leptin and Grimwalde, 1990). Embryos were embedded in Araldite (Electron Microscopy Sciences) and hardened overnight at 55°C. Embryos were sectioned in 7 micron slices and mounted on slides with 50% Araldite/50% Acetone. Sections were visualized using an Axioplan microscope (Carl Zeiss) and Nomarski optics.

Fluorescent staining was achieved with mouse anti-Neurotactin (BP106, DSHB) and guinea pig anti-Twist antibodies, at dilutions of 1:10 and 1:300, respectively. Secondary antibodies were added as a 1:400 dilution of either anti-mouse 543 or anti-guinea pig 488 (Molecular Probes, Invitrogen). Embryos were mounted in 70% glycerol

and sectioned with a standard razor blade. Images were taken on a Zeiss LSM 310 upright confocal microscope (Carl Zeiss).

2PEF microscopy

Mesoderm spreading in *Drosophila* involves fast cell movements, up to 10 $\mu\text{m}\cdot\text{min}^{-1}$ occurring during two hours of development deep inside the embryo at a depth up to 80 μm , which is typically twice the scattering length of near infrared light in this embryo at this stage. These properties make mesoderm spreading challenging to image without compromising viability. Conventional confocal fluorescence microscopy is limited to a half of the required imaging depth (Figure 1C), and typically induces strong photo-toxicity. In order to circumvent these imaging limitations, 2-photon excited fluorescence (2PEF) microscopy appeared to be the most adapted technique. It still requires careful optimization of each imaging parameter, such as the fluorescent labeling, the mounting procedure, or the illumination and collection characteristics, in order to reach the image quality necessary to support computational analysis while at the same time maintaining embryo viability.

Embryos were aged for 3 hours at 25°C and dechorionated by hand. Heptane glue was used to cement embryos to a coverslip ventral side up and prevent any drift during the image acquisition. They were immersed in H₂O and placed directly above a large working distance, low magnification, high numerical aperture, and water-immersion objective (C-Apochromat 40X/1.1 N.A. W Corr UV-VIS-IR, Carl Zeiss), preventing strong refractive index mismatch. The high numerical aperture and low magnification of the objective optimize the light collection when imaging deep inside the scattering

embryo. Each embryo was imaged using 2PEF microscopy with a Zeiss LSM 510 inverted microscope (Carl Zeiss) at 940nm wavelength (Chameleon Ultra laser, Coherent). This high wavelength allows reduction of scattering, photo-toxicity and endogenous fluorescence signal from the yolk, while optimizing GFP excitation. 200 x 200 x 80 μm^3 3D stacks with 0.5 x 0.5 x 1 μm^3 voxel size and 1.9 μs pixel dwell time were typically acquired every 45-50 seconds for approximately 3 hours. Viability was scored by morphological changes of histone-labeled nuclei, timing of germband elongation, cell division delay, and ability to hatch to larvae. The fluorescence signal was collected in epi-collection using a 680 nm short pass filter, allowing collection of more fluorescent light than the standard 500-550nm filter for GFP. In order to increase the fluorescent signal-to-noise ratio when imaging in depth, forward emitted and scattered photons in the transmitted direction were back-reflected using a silver mirror positioned on the dorsal side of the embryo. A significant amount of these photons were epi-collected, with an increase of signal-to-noise reaching ~30%. This procedure was easier and more efficient than the use of a second detection in trans on the LSM 510 microscope. Mutant embryos were aged to stage 13 post-imaging and confirmed using a Dfd-GMR-YFP balancer. The *htl* mutation was recombined into a *klarschist* background (a lipid transport defective embryo) to clear the lipid-rich cells, thus decreasing the scattering properties of the tissue and increasing the imaging depth. *Klarschist* embryos (in the absence of the *htl* mutation) exhibit normal mesoderm migration (Figure S5 and S6).

3D cell tracking

Imaris (Version 5.7, Bitplane) was used for all initial analysis of images. Stacks were rendered into 3D volumes. The fluorescent signal from the nuclei was segmented in 3D using the spot segmentation procedure of Imaris. Segmented nuclei were tracked through the time sequence by applying the Imaris auto-regressive model for spot motion in 3D. Mesoderm and ectoderm tracks were first separated based on the fluorescent signal intensity, as the signal from ectoderm cells at the surface of the embryo appears stronger. This separation was then completed visually. Cell divisions were tracked manually by connecting separate tracks. The tracking data was manually corrected using the track editing function of Imaris. In addition, nuclear segmentation had to be completed semi-automatically for a significant number of mesoderm cells using the manual spot function in Imaris. The cell tracking procedure was helped with custom-made Imaris functions using ImarisXT and Matlab (The MathWorks) scripts. Typically 100 mesoderm cells (see Figure S5) and ~1,500 ectoderm cells were tracked for each embryo, corresponding to ~100,000 cell positions defined over time. All tracking analyses were performed using raw images. Sequences used for movies and figures were treated with a Gaussian filter applied to the entire image to improve image clarity. Overall, 3 wild-type embryos, 3 *htl* embryos (two in the *klar* background and one in the wild-type background), and 2 *klar* embryos were tracked and used for further analysis.

Cell tracking analysis

Cell tracking data were exported from Imaris to Matlab. Cell trajectories were analyzed with custom Matlab scripts. The gaps in cell tracks were filled with linear interpolation of cell positions.

Cylindrical coordinates

The main axis (**L**-axis) of the cylindrical coordinate system (**r**, **θ**, **L**) corresponds to the anterior-posterior axis of the embryo (Figure S1) and was defined by fitting a cylinder to the ectoderm cell positions at stage 7 of development. A least-squares cylinder was fitted to the cell positions using a Gauss-Newton algorithm. The spatial positions $\mathbf{r}_i(t)$, $\theta_i(t)$, and $\mathbf{L}_i(t)$ of each cell i were subsequently computed using the cylindrical coordinates (see Fig S1). The $\mathbf{L}=0$ position was defined arbitrarily along the **L**-axis (close to the cephalic furrow position, positive value towards the posterior direction), the $\mathbf{r}=0$ position corresponds to the center of the embryo and the $\theta=0$ position was defined as the position of the midline. The midline position was obtained experimentally by tracking 6 cells from the neuroectoderm over time. During the time of acquisition, the embryos usually exhibit some solid rotation around the anterior-posterior axis. This angular drift was corrected by subtracting the angular value of the midline position from the angular position of every cell. No significant translational drift of the embryos was observed during the time of acquisition. Defining cell positions in the cylindrical coordinate system allows for artificial unwrapping of the embryo. When the unwrapped cell positions are imported back into Imaris for display using ImarisXT (Movie S4), visualization of the motions in this way facilitates a better understanding of the spreading movement. The main morphogenetic events of mesoderm formation and ectoderm germband elongation are observed in specific directions of the cylindrical system. The radial direction, **r**, corresponds to a movement from the center to the outside of the embryo; mesoderm cells undergo furrow collapse and intercalation mainly in the **r** direction (Figure 2C). The angular direction, **θ**, depicts the medio-lateral movements of cells, such as spreading of

the mesoderm and convergent movement of the ectoderm (Figure 2D). Finally, the anterior-posterior direction, \mathbf{L} , corresponds to movement of cells along the length of the embryo, as occurs during germband elongation (Figure 2E).

Time synchronization and spatial color codes

Wild-type and *htl* sequences were synchronized in time by defining $t=0$ minutes as the onset of ectoderm cell movement in the anterior-posterior direction (L-axis), corresponding to the onset germband elongation. Stages 7, 8, 9 and 10 of development correspond to the time windows: $t < 0\text{min}$, $0\text{min} < t < 30\text{min}$, $30\text{min} < t < 70\text{min}$, and $t > 70\text{min}$, respectively. The upper and lower furrow cells were defined for $r_i(\text{stage } 7) < 0.6R_0$ and $r_i(\text{stage } 7) > 0.6R_0$, respectively, with R_0 being the radius of the fitted cylinder (typically representing the radius of the embryo) and $r_i(\text{stage } 7)$ the radial position of each cell i during stage 7. The radial and angular color codes were also defined depending on the distribution of r_i and θ_i values, respectively, within the mesoderm furrow at stage 7. After each cell division, the color code describing upper/furrow origins for the two daughter cells was defined as that of the originating mother cell. The color code used in Figure 4H and 4I corresponds to $[0.35 R_0; 0.9 R_0]$ at the end of the spreading process.

Cell division and cell intercalation

A cell division event was defined as the time point when cell tracks split into two different tracks and was identified computationally. Cell division orientation was computed automatically as the orientation of the vector joining the two daughter cells (\mathbf{u} vector in Figure S7A) at the time point immediately following the division. The normalized \mathbf{u} vectors for each cell division are displayed in 3D in Figure S7A. Cell

intercalation events were automatically identified from the tracking data using a custom MatLab script by analyzing the relative movement in the radial direction between each mesoderm cell and its nearest neighbors over a 30 minute time window.

Customized statistical analyses

Custom designed statistical analyses were created in order to analysis large amounts of tracking data for the purpose of decomposing movements and to provide a measure of consistency of mesoderm cell spreading between embryos.

Ectoderm/Mesoderm correlation analysis and ectoderm movement subtraction

For the velocity correlation analysis (Figure 2F–H and Figure S4), the instantaneous velocity of each cell was computed. Before that, the cell trajectories were smoothed in time using a 5-point Loess quadratic fit applied to each spatial component. The instantaneous velocity was estimated using low time sampling (a measurement every 13 minutes) by dividing the cell displacement by the time delay; this time sampling was most appropriate for analysis of movement in the 3 directions \mathbf{r} , $\boldsymbol{\theta}$, and \mathbf{L} , as in the \mathbf{r} and $\boldsymbol{\theta}$ directions the movement is slow ($\sim 0.5 \mu\text{m}/\text{min}$) relative to the movement in \mathbf{L} . However, using a time sampling of 13 minutes, the distribution of values along the \mathbf{L} axis is discontinuous (refer to Figure 2H) due to the rapid movement along this axis (up to $5 \mu\text{m}/\text{min}$) during germband elongation (GBE), followed by little movement upon completion of GBE (refer to Figure 2E). If a smaller time sampling is used, then the correlation is continuous. Each spatial component (v_r , v_θ , v_L) of mesoderm cell velocity was plotted depending on the average spatial components of the 6 nearest ectoderm cell

neighbors. The correlation coefficient refers to the Pearson product-moment correlation coefficient.

To subtract the movement of the ectoderm from the mesoderm cells over time, the average displacement ($\Delta\mathbf{r}$, $\Delta\theta$, $\Delta\mathbf{L}$) of six neighboring ectoderm cells was removed from the displacement of each mesoderm cell between each time point. The new mesoderm cell positions were subsequently imported back into Imaris for display using ImarisXT (Figure 2I, Figure S3, and Movie S5).

The correlation analysis of mesoderm and ectoderm cell movements is a demonstration of the strong mechanical coupling of these two movements in the \mathbf{L} direction (Figure 2). This quantitative demonstration identified particular mesoderm cell movements that exhibit no coupling with ectoderm movements. We, therefore, limited our analysis of mesoderm cell movements to two dimensions (\mathbf{r} - and θ -axes), the directions in which no coupling between mesoderm and ectoderm cell movements was observed. In this way, we were able to simplify the study of wild-type and mutant phenotypes.

Consistency analysis of mesoderm cell spreading

In order to compare one embryo to the other as well as to compare wild-type and mutant phenotypes, we developed a statistical analysis to study the overall pattern of cell spreading. The angular positions of each cell at the onset (θ_{start}) and at the end (θ_{end}) (Figures S4A and B) of the spreading process are obtained from the tracking data. These normalized values are plotted in a single 2D graph (Figure S4C). The spatial organization of the spreading observed in wild-type embryos (Figure 3A) is translated into a regular

distribution of points in the $\theta_{\text{end}}(\theta_{\text{start}})$ graph, which tends to align along a line, as shown in Figure S4C. For clarity purpose, the color code used for each cell in Figure 3A and S4B is kept the same in Figure S4C. This distribution is characterized by fitting a regression line: $\theta_{\text{end}} = A \cdot \theta_{\text{start}} + B$. The variables A and B are estimated using a least-squares method, and the resulting correlation coefficient is R.

A, B, and R have specific biological meanings. B is close to 0 when the spreading is symmetrical with respect to the midline. The slope A of the line characterizes the general spreading behavior and its strength. Values of A=1 and B=0 describe the case in which no movement has occurred at all. Values of A>1 describe normal spreading (white area in Figure S4C-K); the higher the value, the stronger the spreading is. A≤1 means an absence of movement or abnormal movement has occurred (grey area in Figures S4C and S4E-K). For clarity purpose, the graphs S4D-E show three typical cases (assuming that B=0). If a cell is spreading normally (blue line in S4D), the $\theta_{\text{end}}(\theta_{\text{start}})$ position of the cell is in the white area (blue cross in S4E, with A>1). If A>0 and <1 (red color in S4E), the cell is moving toward the midline (red line in S4D). If A<0 (green color in S4E), the cell is crossing the midline and migrating to the opposite side of the embryo (red line in S4D).

Note: The term coupled is used when a quantitative parameter (such as the velocity) in a specific population of cells (mesoderm) is correlated to the same parameter in another population (ectoderm). This correlation is estimated using a Pearson product-moment correlation coefficient.

The term collective is used when a specific behavior (such as the spreading angle relation $\theta_{\text{end}}(\theta_{\text{start}})$) is quantitatively defined and shared by every cell of a single population. The collective nature of the process is quantified by applying a regression

model and estimating the resulting correlation coefficient (R in this study). When the R value is close to 1, the quantitative behavior following the model is claimed to be collective.

RESULTS

Here we used optimized 2-photon excited fluorescence (2PEF) (Helmchen and Denk, 2005; Supatto et al., 2005) to image large domains of *Drosophila* embryos ubiquitously expressing nuclear GFP [Figure 1C, D; (Clarkson and Saint, 1999)] with sufficient spatial and temporal resolution to follow mesoderm spreading noninvasively over two hours [Figure 1E, Supplementary Movie S1]. The complex cell movements of the mesoderm and ectoderm cells were extracted from each large imaging dataset (~3 billion voxels) using 3D segmentation of cell positions and 3D tracking over time (Figure 1F–H, Supplementary Movie S2). This involved the analysis of over 100,000 cell positions per embryo (Supplementary Movie S3). Computational analysis captured the three main morphogenetic events of the mesoderm (Figure 1F), and confirmed that the ectoderm cell layer, upon which mesoderm cells are migrating, undergoes germ-band elongation by means of convergent-extension movements [Figure 1I and 1J; (Irvine and Wieschaus, 1994; Zallen and Blankenship, 2008)].

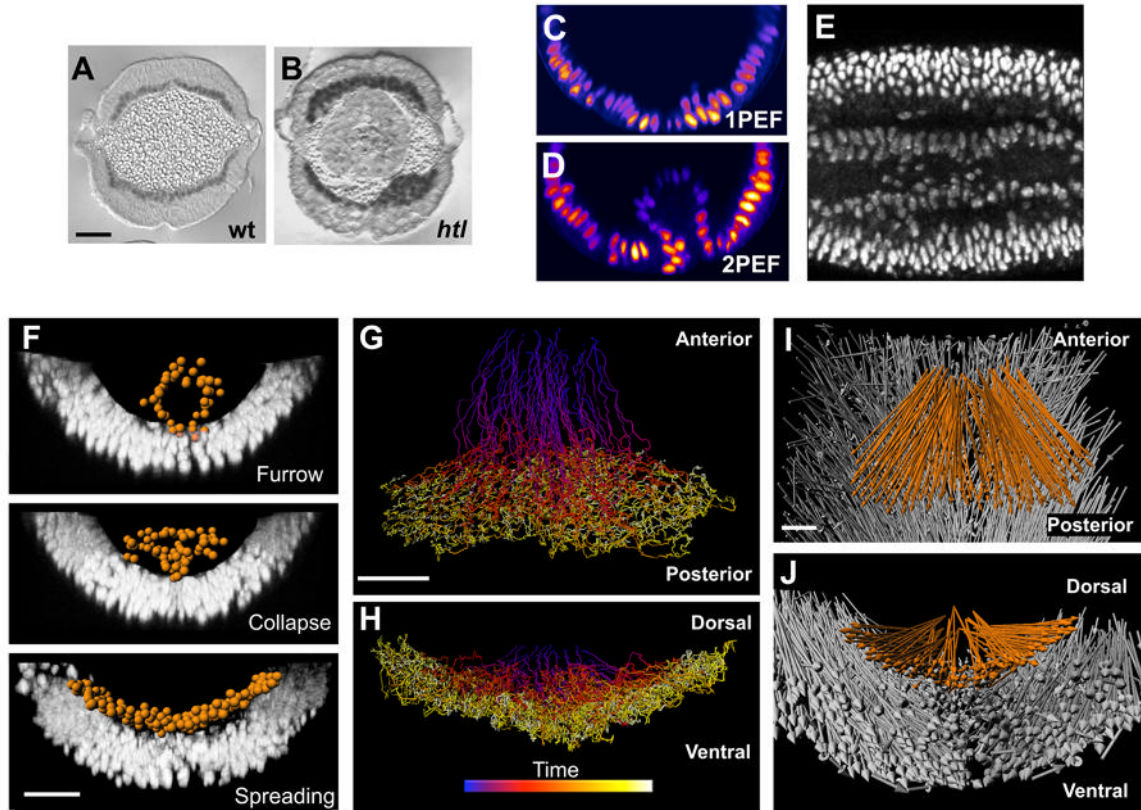


Figure 1. Two-photon microscopy and analysis of Histone2A-GFP expressing embryos captures key events in gastrulation. (A, B) Cross-sections of wild-type (A) and *htl* mutant (B) embryos stained with Twist antibody. (C, D) Confocal one-photon excited fluorescence (C) fails to image internalized Histone2A(H2A)-GFP in mesoderm cells, while 2PEF (D) captures the positions of the internalized cells. (E) A 50 μm deep, 10 μm thick lateral slice through an H2A-GFP embryo demonstrates the signal to noise ratio (anterior, left). (F) Segmentation of mesoderm nuclei using Imaris software (orange spheres). Each sphere was defined by the fluorescent intensity of H2A-GFP. Furrow formation, furrow collapse as a result of an epithelial-to-mesenchymal transition, and spreading of the mesoderm to form a monolayer are illustrated from top to bottom, respectively. (G–J) Tracking cell positions in 3D over time. Dorsal (G) and posterior (H) views of mesoderm tracks (blue and yellow indicate early and late timepoints, respectively). Dorsal (I)

and posterior (**J**) views of mesoderm (orange) and ectoderm (grey) net displacement vectors. Scale bar= 20 μm .

We developed custom software tools to extract quantitative information from the cell trajectories and to describe the dynamic behavior in detail [Supplementary Movie S3; see Methods for more details]. First, the positions of cells were redefined in accordance with a cylindrical coordinate system ($\mathbf{r}, \theta, \mathbf{L}$) by fitting a cylinder on the average position of ectoderm cells. This coordinate system, unlike the standard Cartesian system ($\mathbf{x}, \mathbf{y}, \mathbf{z}$), is more appropriate for the body plan of *Drosophila* embryos and the geometry of their morphogenetic events [Figure 2A-E, Figure S1, Supplementary Movie S4; (Irvine and Wieschaus, 1994; Zallen and Blankenship, 2008)].

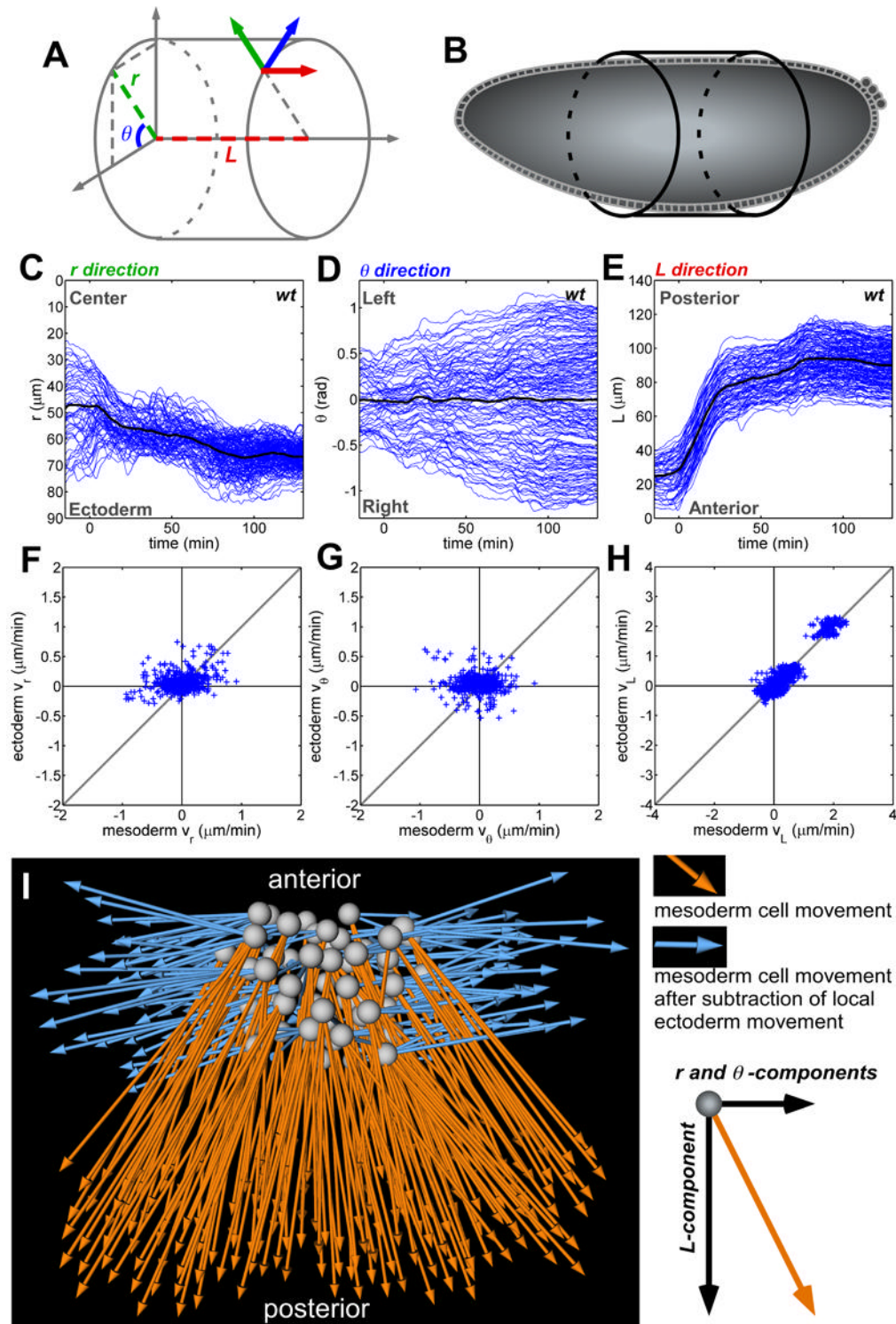


Figure 2. Decomposition and correlative analysis of cell movements using cylindrical coordinates. **(A,B)** The use of cylindrical coordinates allows positioning of cells according to the body plan of the embryo at stage 6. **(C–E)** Cell trajectories (blue lines) reveal that each axis

corresponds to a morphogenetic movement: **(C)** r is radial position over time (e.g., furrow collapse and intercalation, 0 = center of the embryo). **(D)** θ is the angular movement (e.g. mesoderm spreading and ectoderm convergence, 0 = position of the ventral midline). **(E)** L corresponds to movement of cells along the length of the embryo (e.g., germ-band elongation). In **(C–E)**, $t=0$ is set as the point when AP movement begins. **(F–H)** Correlation of the velocity of each mesoderm cell with its six nearest ectodermal neighbors along the **(F)** radial, **(G)** angular, and **(H)** AP axes, with correlation values of 0.21 ± 0.43 , 0.08 ± 0.18 , and 0.90 ± 0.06 , respectively (N=3 embryos). **(I)** Dorsal view of mesoderm cell displacement before (orange) and after (blue) subtraction of local ectoderm cell movements.

The influence of ectoderm cell movements on the migratory path of the overlying mesoderm was determined by investigating the coupling between the motions of these two cell populations. The ectoderm is in close physical contact with the mesoderm: the mesoderm invaginates from the ectoderm, and the ectoderm serves as the substratum on which the mesoderm cells spread during germ-band elongation (Wilson and Leptin, 2000; Zallen and Blankenship, 2008). Previous qualitative studies suggested coupling of their movements; in mutants that fail to form ectoderm, mesoderm cells are specified but fail to move (Irvine and Wieschaus, 1994). Statistical analysis of our data revealed that the trajectories of mesoderm and ectoderm cells correlate highly in the anterior-posterior direction (the L axis; Figure 2H). However, in the other directions (r and θ axes), little to no correlation was found (Figure 2F and 2G). Subtracting axial motions of the local ectoderm cells from the motion of each mesoderm cell resulted in no residual movement of the mesoderm in the L direction (Figure 2I, Supplementary Movie S5 and S6),

suggesting that the mesoderm cells are carried by the strong movement of the ectoderm during germ-band elongation in this direction. The lack of correlation in the radial and angular directions suggests mesoderm cells undergo active movement, distinct from that of the ectoderm.

In the angular direction (θ), mesoderm cell movement was symmetrical with respect to the ventral midline of the embryo, as demonstrated by a θ mean value of 0 (Figure 2D). Using a color code to identify each cell track by its position of origin in the furrow (Figure 3A) revealed a stable, chromatic pattern of the trajectories in the θ direction, highlighting that the spatial organization of cells in this direction is preserved over time. The straightness of the trajectories and the limited intermixing of cells support the view that cell movements are directed. The cell trajectories revealed that a group of cells originating from the upper, lateral parts of the furrow (Figure 3A) becomes positioned at each leading edge of the mesoderm cell population, which was maintained for the entire course of their migration (Supplementary Movie S7). These leading cells were neither the first nor the last to invaginate; instead, their location within the furrow positions them to land in the leading position as the furrow collapses following the epithelial to mesenchymal transition (EMT).

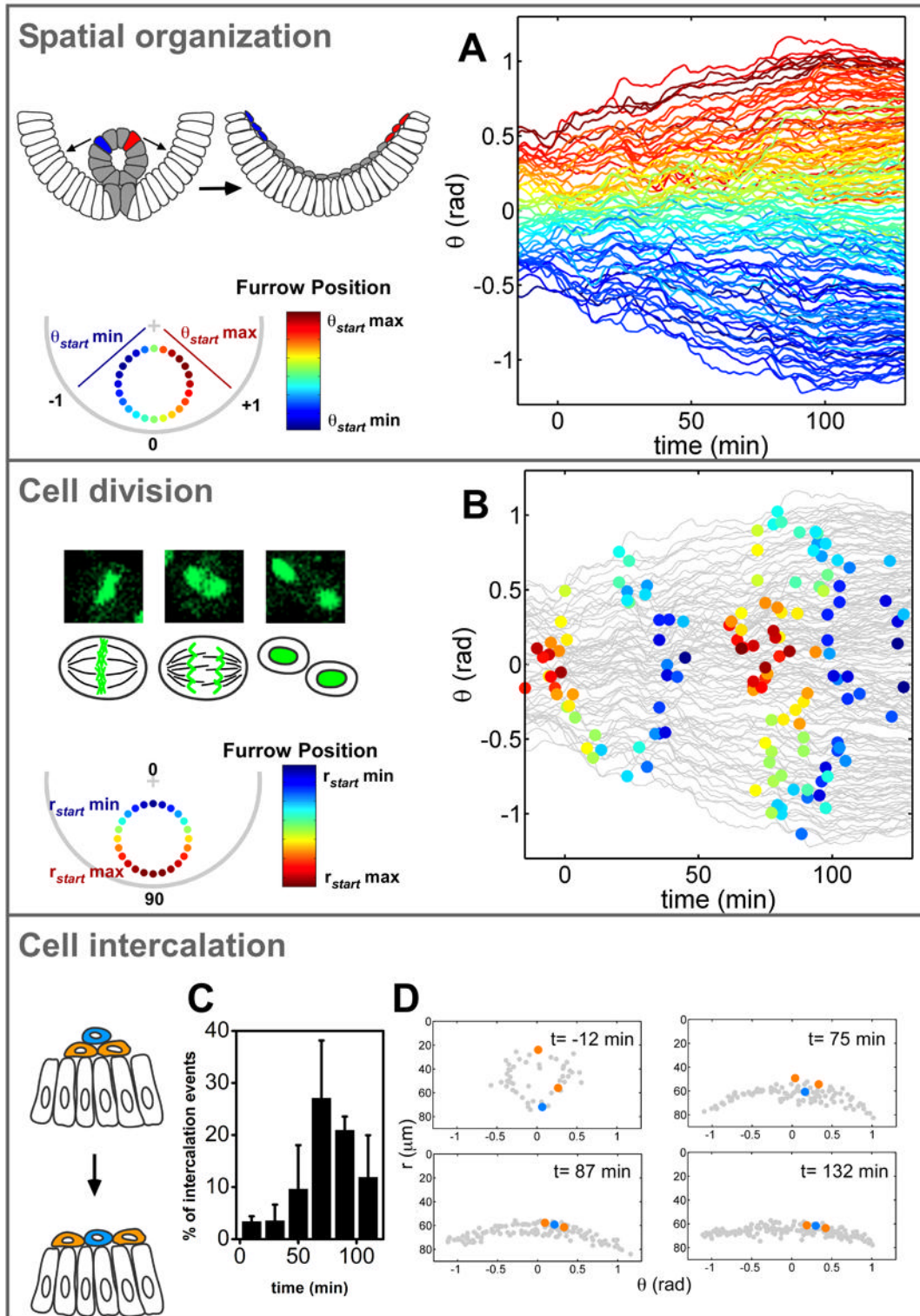


Figure 3. Quantitative analysis of morphogenetic events reveals a high level of organization in wild-type embryos. (A) A color code marks the angular position of cells in the furrow at stage 7

and shows the spatial organization as cells move over time. Each line represents the trajectory of one cell. **(B)** Position and timing of each cell division (colored spot). The color code represents the radial position in the furrow at stage 7. DNA morphology during cell division in H2A-GFP embryos is shown (left). **(C)** Analysis of intercalation events within the mesoderm over time shown as a percentage of mesoderm cells intercalating (N=3 embryos). **(D)** The position of mesoderm cells before and after intercalation events.

Other morphogenetic events that might contribute to mesoderm spreading, such as cell division pattern and cell intercalation, were explored based on our cell tracking data. Each mesoderm cell divided twice (Grosshans and Wieschaus, 2000; Seher and Leptin, 2000; Wilson et al., 2005; Murray and Saint, 2007), and these divisions were ordered in space and time (Figure 3B). Cells nearest the ectoderm divided first, followed by cells nearer to the top of the ventral furrow. This order was maintained during the second division cycle. Analysis of the cell division mutants did not uncover any of the characteristic mesoderm migration defects observable in fixed sections [Figure S6; (Grosshans and Wieschaus, 2000)]. Our tracking data revealed that the orientation of cell divisions within the mesoderm is random, and altering the organization of cell divisions had no effect on mesoderm spreading or embryo viability (Figure S7A-C). Thus, it is unlikely that these organized cell divisions play a role in mesoderm spreading. The radial cell intercalation events (Voiculescu et al., 2007) were synchronous with the second wave of cell division (Figure 3C and D), but the orientation of the cell divisions did not seem to play a causal role in the intercalation motions. Mesoderm cell intercalation contributes to monolayer formation and spreading (Figure 3C).

To facilitate comparisons between embryos, we developed a statistical analysis characterizing the spreading behavior of the mesoderm cells. As suggested by the spatial organization of the spreading (Figure 3A), the angular positions of each cell at the onset (θ_{start}) and at the end (θ_{end}) of the process were highly correlated. A plot of starting and ending positions revealed a linear relationship (Figure S4A–C). Given this, linear regression applied to the θ_{end} (θ_{start}) values provided a measure of both the strength of the spreading (as the slope of the line, A; Figure S4D-E) and a quantitative measure of collective behavior, the degree of correlation, R (see Methods for more details). *wt* cells followed an ordered spreading behavior ($\theta_{\text{end}} \approx 2 * \theta_{\text{start}}$), which is shared by the majority of cells ($R > 0.9$, Figure S5). Comparison of the regression analysis from 5 *wt* embryos showed the consistency of cell behaviors (Figure S5, N=5 embryos and n=596 cells).

Previous studies of fixed embryos (Beiman et al., 1996; Gisselbrecht et al., 1996; Schumacher et al., 2004; Wilson et al., 2005) have suggested that FGF signaling is involved in regulating mesoderm cell migration, but its exact function has remained elusive. We used our methodology to study the function of the FGF signaling pathway on regulation of gastrulation, by analyzing embryos of the FGF receptor mutant, *heartless* (*htl*), in the same way as wild-type embryos (Figure S2, S3, and Supplementary Movie S9). The cell movements within *htl* mutant embryos were decomposed into their components in \mathbf{r} , θ , and \mathbf{L} , (Figure S3A–C) permitting direct comparisons with wild-type embryos (Figure 2C–E). The ectoderm-coupled movements of mesoderm cells in the \mathbf{L} direction were unaffected in *htl* mutants (Figure S3F), and no evidence for defects in cell division events was obtained (Figure S7D). However, *htl* mutant embryos displayed mesoderm cell defects affecting both collapse of the furrow (\mathbf{r} axis) and spreading in the

angular direction (θ axis) (Figure S3A and B). A statistical analysis of cell movement conducted on *htl* mutant tracking data showed a scattered distribution of $\theta_{\text{end}}(\theta_{\text{start}})$ values (Figure S4I and S5), resulting in low spreading and correlation values (Figure S5C, $A < 1$ and $R < 0.5-0.7$, respectively). Values obtained by analysis of individual *htl* embryos or by pooling the cells from multiple *htl* embryos (Figure S5B and C, $N=3$ embryos and $n=284$ cells), demonstrated quantitatively that a similar disruption of spreading is present in all *htl* embryos.

Cell tracking analysis revealed that loss of FGF signaling affected the mesoderm cells nonhomogeneously (Movie S10). In the radial direction, cells originating from the upper half of the furrow (“upper furrow” cells), in general did not collapse, remaining far from the ectoderm during the entire acquisition time (Figure 4A; Figure 3SA, Movie S11 and S8). The angular movement of upper furrow cells was strongly affected in *htl* mutants (Figure 4B-G). In contrast, the last cells to invaginate in *htl* mutants, which comprise the lower furrow, behaved in a manner similar to wild-type mesoderm cells and could achieve the same dorsal position as *wt* (Figure 4G). Our statistical analysis of cell movements of upper and lower furrow cells confirmed the presence of two distinct cell behaviors in *htl* embryos (Figure S5D,E). Other cell labeling approaches, such as photoactivatable GFP, can be used to characterize mutant phenotypes, but the limited number of cells they can follow make interpretation difficult (Murray and Saint, 2007), especially when there are multiple behaviors, as in *htl* mutant embryos.

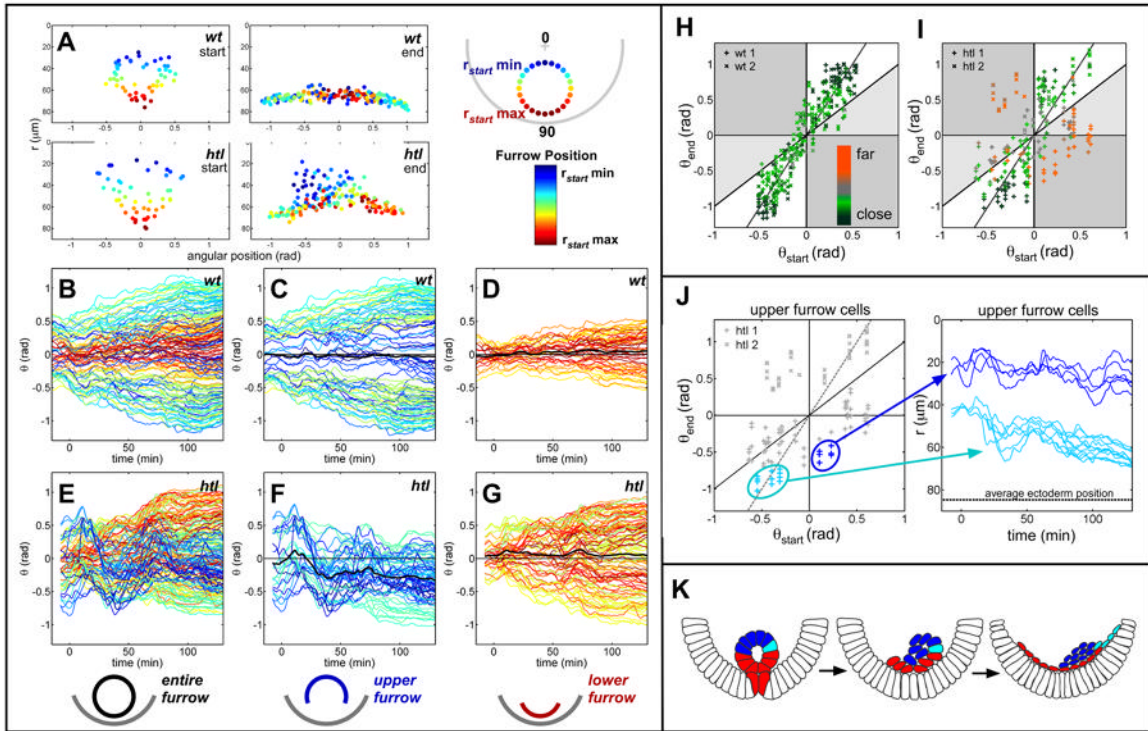


Figure 4. Furrow collapse and spreading of mesoderm cells is disrupted in *htl* mutants. (A) Position of mesoderm cells (spots) at stage 7 and stage 10 in wild-type and *htl* embryos using a radial color code. (B–G) Angular movement of cells over time analyzed in wild-type (B–D) and *htl* mutant (E–G) embryos, within the entire (B, E), upper (C, F), and lower furrow (D, G) (black line = average mesoderm displacement with respect to the midline). (H–I) Spreading profile of wild-type (H) and *htl* (I) embryos. Color code represents distance from the ectoderm at the end of spreading (red=far from ectoderm, green=close to ectoderm). The grey line represents a spreading coefficient of $A=2$, where $\theta_{\text{end}}=A(\theta_{\text{start}}) + B$. Cells that do not spread within the collective are represented within grey regions of the graph (see Appendix B for more details). In general, cells located close to the ectoderm fall along the grey line. (J) The radial position (r) of two particular groups of mesoderm cells from the upper furrow of *htl* mutants is depicted over time. One group exhibits normal spreading behavior (cyan), and the other group exhibits aberrant spreading (blue). (K) The furrow collapse in *htl* mutants is disrupted, resulting in cells falling randomly to one side

of the embryo. Upper furrow cells that reach the ectoderm (cyan) undergo normal spreading, whereas cells that remain far from the ectoderm spread abnormally (blue).

Some cells from the upper furrow in *htl* mutants displayed a normal position in the $\theta_{\text{end}}(\theta_{\text{start}})$ graph, similar to wild-type embryos. These cells were positioned close to the ectoderm at the end of spreading (Figure 4I and J, Figure S4J). This suggested that the distance from the ectoderm might be a major influence on spreading behavior. Indeed, the distinction between the two migratory behaviors observed was more clear when analyzing cells that were close to or far from the ectoderm (Figure S5D,E). This was confirmed by plotting a $\theta_{\text{end}}(\theta_{\text{start}})$ graph using a color code for the radial position of the cells at the end of the spreading process (Figure 4I and J): the *htl* cells that followed *wt* behavior ($\theta_{\text{end}} \approx 2 * \theta_{\text{start}}$ such that $A=2$) ended close to the ectoderm (green color), whereas the cells that stayed far from the ectoderm (red color) had clearly disrupted behaviors, with several cells crossing the midline and migrating in the wrong direction ($A < 0$). All wild-type cells ended up close to the ectoderm (Figure 4H).

DISCUSSION

Our analysis provides several insights into the *htl* mutant phenotype. First, the primary function of FGF signaling must be to help all cells within the furrow to collapse, directing them toward the ectoderm (Figure 4K). Second, another yet unidentified signal must guide migration of the cells in the angular direction toward the dorsal ectoderm, as movement is observed even in the absence of FGF signaling. Third, contact with the

ectoderm is key for the mesoderm to respond to this guidance cue, as distance of the mesoderm cells from the ectoderm defines their migratory competence. Any cell that encounters the ectoderm is capable of directed movement in the angular direction, in response to a cue that cannot solely be FGF dependent. Movement of the mesoderm might require contact with the ectoderm to make them competent to respond to a directional signal, as evidenced in other systems (Sato and Kornberg, 2002; Yang et al., 2002; Krieg et al., 2008).

This study demonstrates that stereotypical morphogenetic events during embryo development can be systematically quantified, analyzed and compared between wild-type and mutant embryos based on the live imaging of large groups of cells. Complex cell movements are decomposed into particular cell behaviors, revealing a high level of organization and permitting the interpretation of subtle mutant phenotypes in *Drosophila*. Future developments in imaging and cell tracking will facilitate this quantitative approach, enabling its application at a larger scale and on other model systems, to expand understanding of collective cell migration and embryonic development from the molecular level to that of the entire organism (Megason and Fraser, 2007).

Chapter 4:

**Mesoderm migration in *Drosophila* is a multi-step process
requiring FGF signaling and integrin activity**

ABSTRACT

Migration is a complex, dynamic process that has largely been studied using qualitative or static approaches. As technology has improved, we can now take quantitative approaches towards understanding cell migration using in vivo imaging and tracking analyses. In this manner, we have established a four-step model of mesoderm migration during *Drosophila* gastrulation: (I) mesodermal tube formation, (II) collapse of the mesoderm, (III) dorsal migration/spreading, and (IV) monolayer formation. Our data provide evidence that these steps are temporally distinct and that each may require different chemical inputs. To support this, we analyzed the role of fibroblast growth factor (FGF) signaling, in particular the function of two *Drosophila* FGF ligands, Pyramus and Thisbe, during mesoderm migration. We determined that FGF signaling through both ligands controls movements in the radial direction. Thisbe is required for the initial collapse of the mesoderm onto the ectoderm, while both Pyramus and Thisbe are required for monolayer formation. In addition, we uncovered that the GTPase Rap1 regulates radial movement of cells and localization of the beta-integrin subunit, Myospheroid, which is also required for monolayer formation. Our analyses suggest that distinct signals influence particular movements, as we find that FGF signaling is involved in controlling collapse and monolayer formation but not dorsal movement, while integrins are required to support monolayer formation only and not earlier movements. Our work demonstrates that complex cell migration is not necessarily a fluid process, but suggests instead that different types of movements are directed by distinct inputs in a step-wise manner.

INTRODUCTION

Controlled cell migration is an essential aspect of development in which cells relocate to respond to chemical signals and form structures (rev. in Lecaudey and Gilmour, 2006; Rorth, 2007; Montell, 2008; Iliina and Friedl, 2009). Aberrant migration, in contrast, can lead to diseases such as metastatic cancer (rev. in Deisboeck and Couzin, 2009; Friedl and Gilmour, 2009). As a result, studying the molecular and physical mechanisms that control migration is crucial for understanding both development and disease. Several models have been developed for examining different types of cell migration in vivo, such as the border cells in *Drosophila melanogaster* and the lateral line in *Danio rerio* for studying small group migrations; the neural crest cells in vertebrates for studying streaming; and wound healing for understanding sheet migration (rev. in Friedl and Gilmour, 2009; Rorth, 2009; Weijer, 2009). We study the migration of the mesoderm during gastrulation in *Drosophila melanogaster* embryos, as it is a tractable model for the collective migration of hundreds of mesenchymal cells that can be characterized by quantitative analysis (McMahon et al., 2008; Supatto et al., 2009).

Mesoderm migration in *Drosophila* involves several movements that transform a tube of cells into a monolayer; the completion of this migration is important for muscle and heart development (Leptin and Grunewald, 1990; Wilson and Leptin, 2000). First, the mesoderm invaginates by apical constriction to form an epithelial tube within the embryo. The mesoderm then undergoes an epithelial to mesenchymal transition (EMT) and collapse of the tube follows. Next, the collapsed cells spread dorsally along the ectoderm. Lastly, the mesoderm transforms from a multi-layer to a monolayer. This sequence of events has been described previously, but it was not known if these

migratory actions were distinct or overlapping events. Furthermore, it has not been established whether particular biochemical signals are required to coordinate each event.

The most well characterized molecular action during mesoderm migration is fibroblast growth factor (FGF) signaling (rev. in Wilson et al., 2005; Murray and Saint, 2007; McMahon et al., 2008; Kadam et al., 2009; Klingseisen et al., 2009). FGF signaling is essential in animals for both differentiation and migration (rev. in Thisse and Thisse, 2005). The FGF receptor (FGFR) Heartless (Htl) has been studied extensively in the context of mesoderm migration and differentiation (Beiman et al., 1996; Gisselbrecht et al., 1996), and has recently been shown definitively to control organized collapse of the mesodermal tube onto the underlying ectoderm during *Drosophila* gastrulation (McMahon et al., 2008). This organization helps maintain the collective behavior of the mesoderm, as the absence of Htl results in two behaviorally distinct cell populations. However, it remains unclear how the two ligands for Htl, the FGF8-like Pyramus (Pyr) and Thisbe (Ths) proteins, contribute to this process.

In the *Drosophila* system, two different models have been presented regarding how Pyr and Ths activate the Htl receptor during mesoderm migration. The first model proposes that the ligands function redundantly and provide robustness, and the second suggests that the ligands activate the receptor differentially (Kadam et al., 2009; Klingseisen et al., 2009). These previous studies, which include our own previous work, addressed the role of Pyr and Ths ligands by extrapolating their functions during the dynamic process of migration through examination of fixed tissues. Thus, it had yet to be determined definitively whether both Pyr and Ths are required for mesoderm migration during *Drosophila* gastrulation and, furthermore, whether the ligands regulate specific

aspects of migration. Therefore, in this work, we explored the roles of Pyr and Ths during mesoderm migration using *in vivo* imaging and quantitative analyses; the general approach used previously to decipher the FGFR mutant phenotype (McMahon et al., 2008; Supatto et al., 2009).

In addition to studying the two FGF ligands, we examined other molecules that could contribute to specific steps during mesoderm migration to test the hypothesis that mesoderm migration has temporally distinct inputs. We chose to examine the small GTPase Rap1 and integrins, as both have been implicated in migration and linked to FGF signaling (Mori et al., 2008; Carmona et al., 2009; Franzdottir et al., 2009). Rap1 has been shown to be involved in cell adhesion and migration in other systems (Huelsmann et al., 2006; Jeon et al., 2007; Boettner and Van Aelst, 2009). One way that Rap1 specifically regulates cell adhesion/migration is through integrin activation (Reedquist et al., 2000; Kooistra et al., 2007; Boettner and Van Aelst, 2009; Carmona et al., 2009). Integrins, in turn, are required for cell-cell junction formation and provide a physical link from these junctions to the actin cytoskeleton (rev. in Delon and Brown, 2007; Vicente-Manzanares et al., 2009). Of the two β PS subunits, only the β PS1 integrin, Myospheroid (Mys), is expressed in the *Drosophila* embryo during mesoderm migration (Leptin et al., 1989). Mys is involved in recruiting two alpha integrin subunits, α PS1 (Multiple edematous wings) and α PS2 (Inflated), to the cell membrane to form adhesion complexes that are important for cell migration and muscle attachment throughout *Drosophila* development (Leptin et al., 1989; Brown, 2000; O'Reilly et al., 2008). This evidence led us to investigate a role for Rap1 and Mys during mesoderm migration.

In this work, we find that mesoderm migration is indeed a multi-step process with temporally distinct migratory events. We show that movements in the radial direction, specifically collapse and monolayer formation, are controlled by FGF signaling. Dorsal movements appear to be FGF independent. We find that the integrin Mys is required only for monolayer formation. These results indicate that collapse, spreading, and monolayer formation are not only temporally distinct, but are also likely molecularly distinct.

MATERIALS AND METHODS

All crosses and strains were maintained at 25°C. The following lines were used: *yw*; *klar*¹; *htl*^{AB42}/TM3,ftz-lacZ; His2AV-GFP; *twi-gal4*; *twi-CD2*; *mys*¹,FRT19A/FM7c,ftz-lacZ (Bloomington Stock Center); DfBSC25; *pyr*^{e02915}; *ths*^{e02026}; Df²³⁸ (Kadam et al., 2009); *pyr*¹⁸; *ths*⁷⁵⁹ (Klingseisen et al., 2009); *Rap1*^{CD3} (Asha et al., 1999); *klar*¹,His2AV-GFP; *klar*¹,His2AV-GFP,*htl*^{AB42}/TM3,P[Dfd-GMR-nvYFP]3, Sb¹ (McMahon et al., 2008). Wild-type refers to *yw* or His2AV-GFP flies. Germline clones were made for *Rap1*^{CD3} and *mys*¹ and were produced using standard FRT-mediated germline clone methodology (Chou and Perrimon, 1996).

Morpholino Design and Injection

Anti-sense morpholinos were designed using the GeneTools Oligo Design and ordering system (Gene Tools, LLC.). The following sequences were used to make morpholinos:

pyr CATTGGGCATGAACTTGTGGAACAT

ths GCAGTCTCTCTAACTGATTCGACAT

Gal4 CGATAGAAGACAGTAGCTTCATCTT

mys TCGAGGATCATGGCTTTGGCGGTTA

Morpholinos were resuspended in water to a final concentration of 1.5 to 2mM. Filtered liquid green food coloring was added at 1/10 (vol/vol) to aid in visualization of injection. The injection protocol used was a modified version of Misquitta and Paterson, 1999. *yw* or *His2Av-GFP* flies were collected in 15 minutes intervals, washed with water to remove yeast and debris, lined up on a glass slide in a small volume of water and allowed to dry for 10 minutes before injection. Embryos were then covered with a thin layer of Halocarbon Oil 27 (Sigma-Aldrich). A morpholino or buffer alone was loaded into machine-pulled (Narishige) glass needles (FHC Inc.). Morpholinos were heated to 65°C and allowed to cool at room temperature prior to being loading into the needle to prevent clogging. Morpholinos were injected into the ventral or dorsal side of the pre-cellularized embryo using a Picospritzer (Parker Instrumentation) set to a 40 millisecond, 60 PSI ejection delivering approximately 100-200 pL into each embryo. Embryos were allowed to recover for at least two hours at 18°C in a humidified chamber. When the embryos reached stage 5, the embryos were set up for fixing or live imaging as previously described (Frasch, 1995; McMahon et al., 2008; Supatto et al., 2009).

Double-stranded RNA (dsRNA) targeted to *Pyr* and *Ths* transcript was designed as an additional control to confirm the mesoderm migration phenotype following previously described methods (Misquitta and Paterson, 1999). The following primers were used to amplify portions of the *pyr* and *ths* cDNAs (Stathopoulos et al., 2004):

Pyr:

5' GGATCCTAATACGACTCACTATAGGATTGCGCGGCTACAGATACT 3'

5' GGATCCTAATACGACTCACTATAGGATATTTTCGCCTTGATTTGCG 3'

Ths:

5' GGATCCTAATACGACTCACTATAGGAGATCACCTGGACAATTCCG 3'

5' GGATCCTAATACGACTCACTATAGGCCGTATGGGTCTCTTCATGG 3'

dsRNA was made from PCR products using the T7 RNA polymerase.

Fixation and Antibody Staining

Embryos were fixed and stained using in-situ, antibody, or antibody and in-situ protocols as previously described (Lehmann and Tautz, 1994; Frasch, 1995; Kosman et al., 2004). The following antibodies were used in this study: guinea pig anti-Twist (Mike Levine, UC Berkeley, USA), rabbit anti-Even skipped (Manfred Frasch, University of Erlangen, Nürnberg, Germany), rabbit anti-Beta galactosidase (Molecular Probes), mouse anti-rat CD2 (Serotec), and mouse anti-integrin- β PS1 (Developmental Studies Hybridoma Bank). Embryos were mounted in Permount (Fischer Scientific) for whole-mount studies or embedded in acetone-araldite (Electron Microscopy Sciences) and cut with a microtome (LKB Bromna) to create 10 μ m sections. Fluorescent images were obtained with a Pascal confocal microscope (Carl Zeiss).

Two Photon Microscopy and Image Analysis

Embryos were imaged as previously described (McMahon et al., 2008; Supatto et al., 2009) using a Zeiss LSM 510 inverted microscope (Carl Zeiss) at 940nm wavelength

(Chameleon Ultra laser, Coherent). At least three embryos for each of the following backgrounds were imaged and tracked: wild-type, *pyr* morpholino, *ths* morpholino, *htl*^{AB42} mutant, *pyr* and *ths* double morpholino, and *mys* morpholino. In addition, one null mutant was imaged for *pyr* (*pyr*^{e02915}) and *ths* (*ths*^{e02026}/*ths*^{Df238}) to confirm that the morpholino data was consistent with the null alleles. Nuclear tracking was performed on imaging data as previous described (McMahon et al., 2008) using Imaris software (Bitplane). Data from Imaris was exported to Matlab (The Mathworks) using ImarisXT, and analyzed as previously described using custom Matlab scripts (Supatto et al., 2009). Briefly, tracking data from the ectoderm was fit to a cylinder in order to convert the coordinate system used during imaging (i.e., Cartesian) into cylindrical coordinates. This allows for analysis of each movement along the corresponding body axis. A color-code is applied to show the organization of the mesoderm cells as they collapse and spread along the ectoderm.

To quantify intercalation events, a customized Matlab program was created to examine each row of mesoderm cells over time. Each cell was sequentially highlighted in blue so that it could be followed during monolayer formation. A cell was counted as being stably in the monolayer if it joined the monolayer and remained through stage 11 (~130 minutes after tube collapse). Linear fits to the data from the final four time points in Figure 5J were performed, with the time data centered and scaled. The intercept parameters for the linear fits were then compared pair-wise by Welch's modified *t*-test. The largest *p*-value found was 0.0018.

Statistical analysis of protrusive activity

Protrusive activity was quantified by measuring the number of large protrusions (i.e., greater than one hair-like extension per cell) per image, within a length of ~ 60 microns across per image. The numbers were compared using two-tailed Welch's *t* tests.

RESULTS

Mesoderm migration involves temporally distinct events

Mesoderm migration involves a series of complex behaviors that transform a tube of cells into a sheet of cells (Leptin and Grunewald, 1990; rev. in Wilson et al., 2005). Before migration begins, the mesoderm invaginates into the interior of the embryo via apical constriction of epithelial mesoderm cells, forming the ventral furrow. Next, the mesoderm cells lose their epithelial characteristics and migrate toward the ectoderm (mesoderm tube collapse, Figure 1A, B). The cells then change direction and move dorsally along the ectoderm (Figure 1D, E). Lastly, mesoderm cells that are not in contact with the ectoderm do so, forming a monolayer (Figure 1G,H).

Using live imaging of wild-type embryos, we explored whether the movements that encompass mesoderm migration are distinct or overlap temporally. Embryos were imaged and mesoderm cells were tracked as previously described (Supatto et al., 2009). Tracking data was transformed into cylindrical coordinates using Matlab to fit the body plan of the embryo, so that the radius of the cylinder/embryo, r , reflects movement in the radial direction (e.g. collapse of the mesodermal tube and intercalation; Figure 1 C,I), and the movement along curvature of the embryo, θ , represents motion in the angular direction, associated with the dorsoventral axis (e.g. dorsal spreading; Figure 1F). In our

previous study, we focused on decomposing the 3D movement of cells in particular directions (McMahon et al., 2008). In this work, we highlight the fact that collapse, spreading, and monolayer formation are temporally distinct (Figure 1B,F,I). We hypothesized that these movements involve different types of migratory behaviors guided by distinct molecular signals. As a result, our aim was to define the role of the genes involved in regulation of mesoderm migration within this temporal and spatial framework.

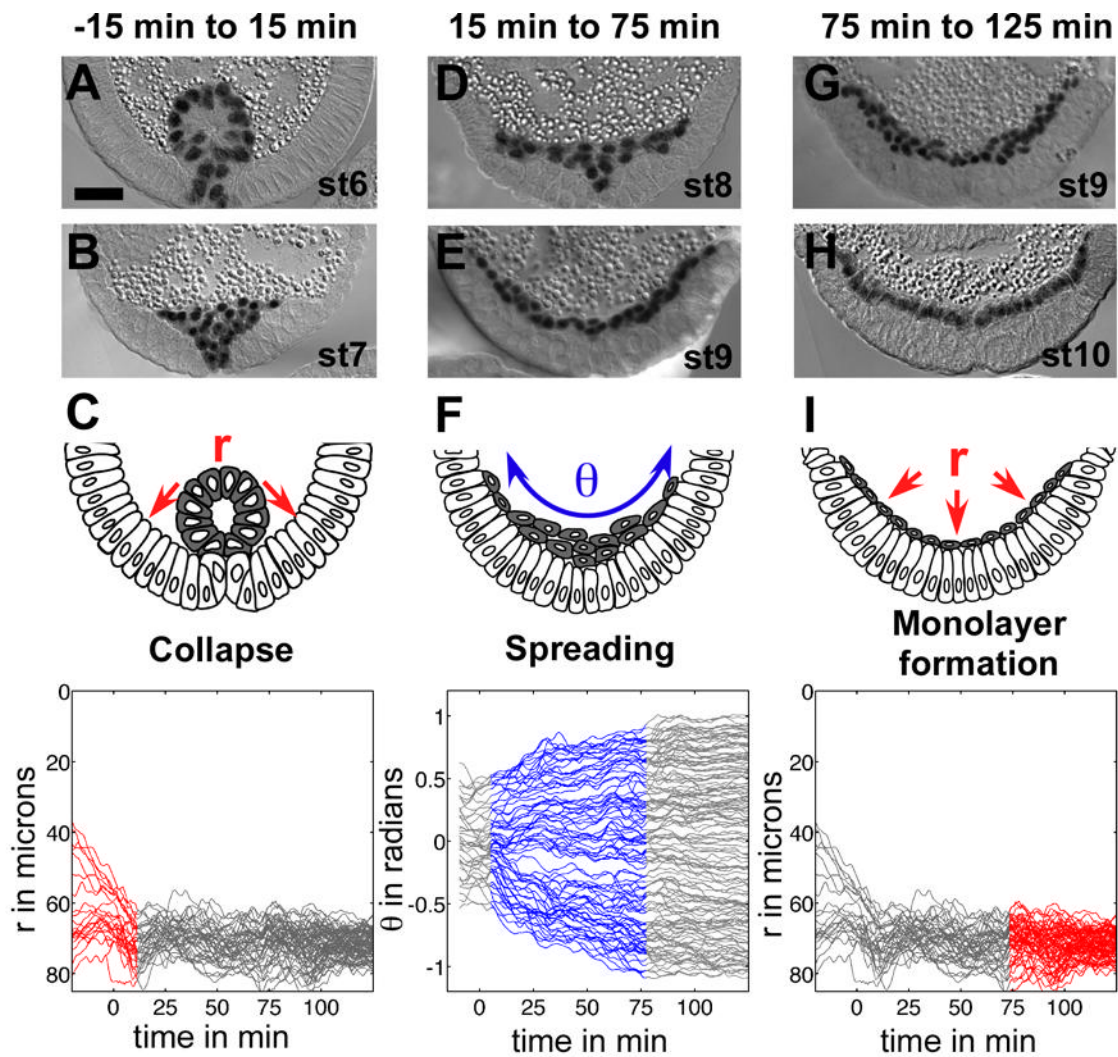


Figure 1. Mesoderm migration is a multi-step process involving temporally distinct movements. (A,B,E,G,H) Embryo cross-sections stained with twist antibody (black) to

mark the mesoderm. Each stage is shown to demonstrate movement of the mesoderm over time: (A) stage 6, (B) stage 7, (D) stage 8, (E,G) stage 9, and (H) stage 10. 0 min refers to the onset of germband elongation. Scale bar = 20 μm . (C) Collapse involves movement of mesoderm cells toward the ectoderm. Movement of mesoderm cells toward the ectoderm is represented by the radial axis of a cylinder, r (y -axis: 0 = center of embryo, 90 = ectoderm). The collapse of the mesoderm is shown as r over time, with each line representing movement of a single cell. Red is used to highlight the time period of collapse. (F) Spreading occurs after collapse and involves mesoderm cells crawling along the ectoderm, which is represented by the curvature of a cylinder, θ . Spreading is demonstrated by graphing θ over time (midline = 0, dorsalmost points = 1, -1). The timing of spreading is highlighted in blue. (I) Monolayer formation occurs last and involves incorporation of all cells into one layer via intercalation (see Figure 5 for more details). Monolayer formation happens in the r direction from 75 minutes onward (highlighted in red).

Pyramus and Thisbe mutants display a non-monolayer phenotype

FGF signaling has been previously shown to be important for mesoderm migration. We showed recently that the preliminary function of the FGFR Heartless (Htl) is to support symmetrical collapse of the mesoderm onto the ectoderm (McMahon et al., 2008). We set out to find whether the ligands for Htl — the FGFs Pyramus (Pyr) and Thisbe (Ths) — are both required for mesoderm migration, and if so, whether they have distinct roles in migration. Pyr and Ths are expressed in dynamic patterns throughout development and have non-overlapping expression domains during mesoderm migration

(Figure 2A and B; Gryzik and Muller, 2004; Stathopoulos et al., 2004). The *pyr* and *ths* mutant phenotypes were previously described using fixed sections. One study found that *pyr* and *ths* mutants both have a mesoderm monolayer defect (Kadam et al., 2009), while the other claimed that only *pyr* was important for monolayer formation (Klingseisen et al., 2009), demonstrating that analysis of dynamic processes using fixed sections can be inconsistent, especially if the phenotype is variable or subtle.

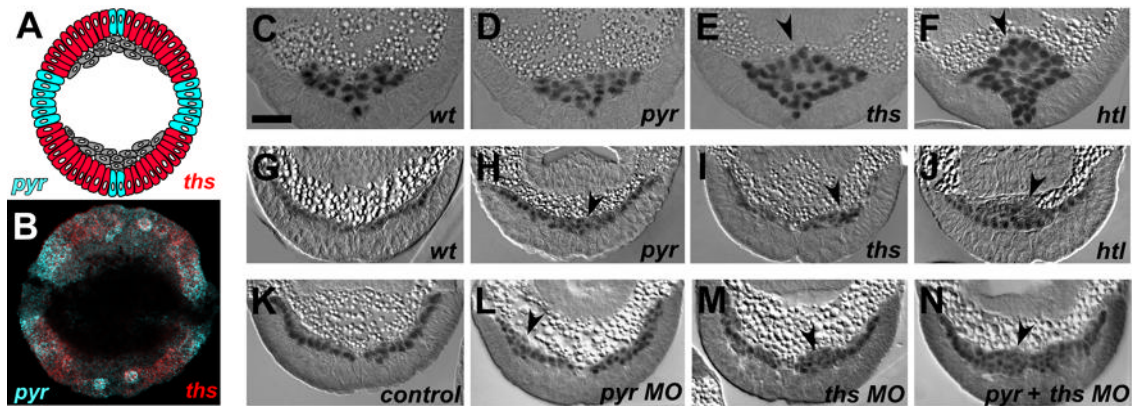


Figure 2. *pyr* and *ths* mutants have a non-monolayer mesoderm phenotype. (A,B,G-M) Embryo cross-sections at stage 10. (C-F) Embryo cross-sections at stage 7. (A) Schematic of Pyr (blue) and Ths (red) expression in the ectoderm during mesoderm spreading. The receptor Htl is found in the mesoderm (grey). (B) Expression patterns of *pyr* (blue) and *ths* (red) transcript during mesoderm spreading detected by in-situ hybridization. (C-M) Embryos sectioned and stained with twist antibody (black) in (C,G) wild-type, (D,H) *pyr*^{e02915}, (E,I) *ths*^{e02026}/*ths*^{Df238}, and (F,J) *htl*^{AB42} mutants. Arrowheads highlight defects. Morpholinos (MOs) were injected for live imaging purposes (see Materials and Methods). Injection of (K) *gal4* MO, which does not have a target in *Drosophila*, did not affect mesoderm spreading, while injection of (L) *pyr* MO and (M) *ths* MO produced phenotypes similar to the genetic mutants. (N) Injection of *pyr* and *ths* MO together produced a phenotype similar to *htl* mutants. Scale bar = 20 μm.

We confirm by statistical analysis of fixed sections that *pyr* and *ths* mutants do both exhibit a non-monolayer mesoderm phenotype, one weaker than that of the FGFR *htl* mutant (Figure 2C-J and FigureS1 in supplementary materials). All available mutants produce similar phenotypes, in general, but the phenotypes are variable, as *ths* supports a severe non-monolayer phenotype more frequently than *pyr* (Table 1 and FigureS1 in supplementary material). Placing a *pyr* allele over a *ths* allele was able to rescue monolayer formation, dismissing the possibility that a second site mutation contributes to the observed phenotype (FigureS1 in supplementary materials). In addition, we generated morpholinos and double-stranded RNAs (dsRNAs) to both *Pyr* and *Ths*, which produced similar phenotypes to the loss-of-function mutants (Figure 2K-N and FigureS1 in supplementary materials). By analyzing several different mutant backgrounds, it is clear that both *Pyr* and *Ths* are important for mesoderm migration. We therefore used in vivo imaging to determine their precise role in this dynamic process.

Table 1. Percent of embryos with a mesoderm monolayer at stage 10

Genotype	% Monolayer (N= number of embryos scored)
wild-type	84.6 (N=13)
<i>pyr</i> ^{e02915}	42.8 (N=11)
<i>ths</i> ^{e02026/DF238}	25.0 (N=12)
<i>htl</i> ^{AB42}	0 (N=7)
DFBSC25	0 (N=10)
gal4 MO	88.9 (N=18)
<i>pyr</i> MO	45.5 (N=11)
<i>ths</i> MO	27.3 (N=11)
<i>pyr</i> + <i>ths</i> MO	11.1 (N=18)

MO=morpholino

In vivo imaging reveals that *thisbe* mutants have a collapse defect

We used two-photon microscopy to image *pyr* and *ths* mutants expressing ubiquitous H2A-GFP, which permits simultaneous tracking of mesoderm and ectoderm cells during gastrulation (Figure 3A-D; McMahon et al., 2008). This permitted us to decompose the migration into different types of movements and to decipher the subtle non-monolayer phenotypes.

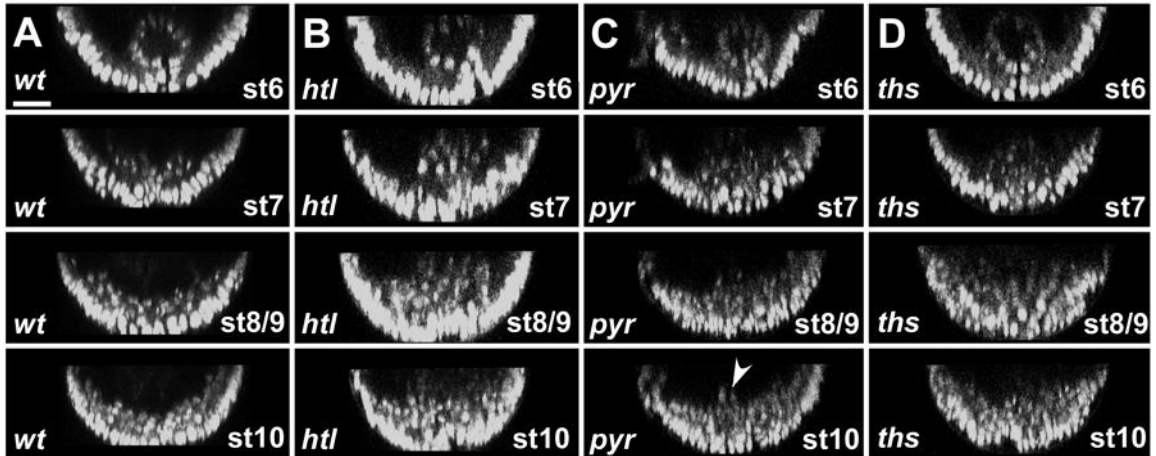


Figure 3. Live imaging of FGF mutants using two-photon microscopy. (A-D) Virtual cross-sections of H2A-gfp expressing embryos taken from 4D imaging data sets (3D plus time) obtained on a two-photon microscope (see Materials and Methods for details). (A) Wild-type embryos undergo characteristic movements: invagination at stage 6, collapse of the mesodermal tube at stage 7, spreading at stage 8/9, and monolayer formation at stage 10. (B) *htl* mutant embryo at stages 6-10. *htl* mutants have a collapse defect at stage 7 resulting in a severe non-monolayer at stage 10. (C) *pyr* mutant embryo at stages 6-10. *pyr* mutant embryos undergo normal collapse and spreading during stage 6-9. A few cells are observed outside the monolayer at stage 10 (arrowhead). (D) *ths* mutant embryo at stages 6-10. In *ths* mutants, collapse is defective at stage 7 and a severe non-monolayer is observed at stage 10. Scale bar = 20 μ m.

To facilitate more efficient live imaging, we utilized translation blocking morpholinos (MOs) designed against *pyr* and *ths* transcripts to reduce the number of imaging sessions required to obtain mutant data; when assaying embryos of zygotic recessive mutant backgrounds only one of four embryos is a homozygous mutant, whereas each morpholino injected embryo displays the expected phenotype. Morpholinos injected into pre-cellularized embryos were able to reproduce the *pyr* and

ths phenotypes of loss-of-function alleles (Figure 2K-L and Figure S1G in supplementary material). In addition, co-injection of *pyr* and *ths* morpholinos supported a mutant phenotype that was more severe and comparable to that of both *htl* mutants (compare Figure 2J to 2N) as well as the mutant background *Df(2R)BSC25*, which removes both *pyr* and *ths* genes (data not shown; Stathopoulos et al., 2004).

We imaged both morpholino and null mutants for Pyr and Ths (see Materials and Methods) and tracked a subset of mesoderm cells over time using Imaris software (Movies 1-2 in supplementary materials). As with wild-type embryos (see Figure 1), tracking data was converted into cylindrical coordinates to fit the body plan of the embryo (Figure 4A). When the movement is decomposed into r and θ , it reveals that *ths* mutants, like previously characterized *htl* mutants, have a mesoderm tube collapse defect in which cells from the uppermost part of the tube fail to migrate toward the ectoderm (blue lines, Figure 4B-C,E,G). In *htl* mutants, tube collapse is asymmetrical, with the tube falling either toward the left or right half of the embryo, resulting in an indirect migratory defect along θ (Figure 4D,F; McMahon et al., 2008)). Unlike in *htl* mutants, however, movement in the angular direction is at worst very mildly affected in a few cells in *ths* mutants, suggesting that Pyr can keep the collapse symmetrical in the absence of Ths (Figure 4H). *pyr* mutants display little to no defects along r or θ (Figure 4I and J), which suggests that Ths is able to support mesodermal tube collapse in the absence of Pyr.

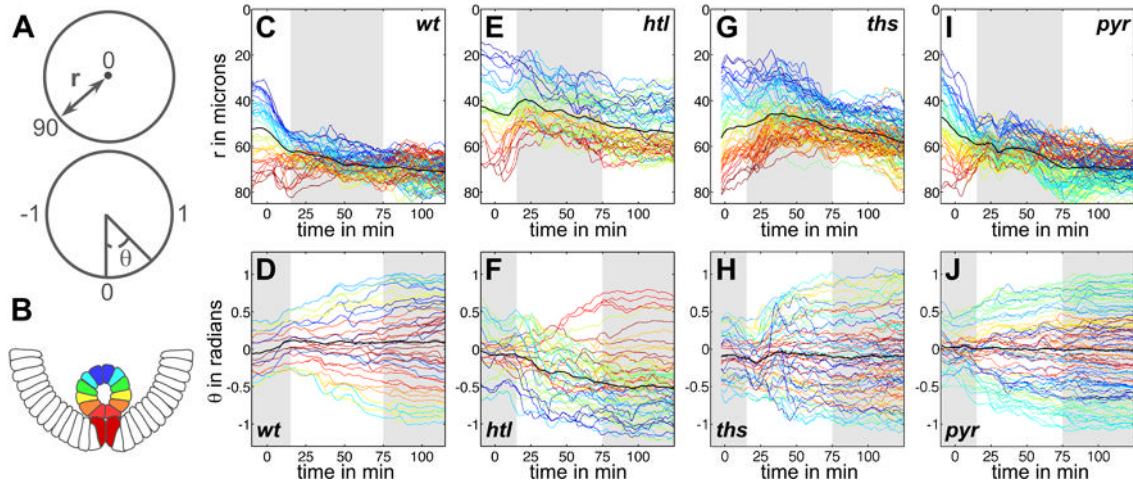


Figure 4. Live imaging and nuclear tracking reveals defects in *ths* mutants. (A) *Drosophila* embryos are roughly cylindrically shaped, such that movement of mesoderm cells along the dorsoventral axis can be represented by the curve of a cylinder, θ (0 =midline). Movement along the radial axis r represents movement of mesoderm cells toward or away from the ectoderm (0 =center of embryo). (B) A color code is applied to track the progress of each cell over time, with a color assignment given at stage 6 and retained throughout migration. The color code is along the radial axis, where red represents mesoderm cells closest to the ectoderm at stage 6 while blue represents the furthest mesoderm cells. (C,E,G,I) Collapse of the mesodermal tube as shown by a graph of r over time where each line represents the movement of one cell (y-axis: 0 = center of embryo, 90 = ectoderm; the black line is the average of all tracks). White boxes highlight the time intervals of collapse and intercalation in wild-type embryos defined in Figure 1. (C) Wild-type embryos undergo collapse of the mesodermal tube to flatten along the ectoderm. Mesoderm cells in (E) *htl* mutants and (G) *ths* mutants fail to collapse. (I) *pyr* mutants display no collapse defect. (D,F,H,J) Spreading of mesoderm cells away from the midline (0) toward the dorsal-most point of the embryo (1 or -1) is shown by graphs of θ over time. The black line is the average of all tracks. White boxes highlight the time intervals of spreading in wild-type embryos as defined in Figure 1. (D) Wild-type mesoderm cells spread directionally away from the midline toward the dorsal-most point in the embryo, while (F) *htl* mutants have aberrant spreading behavior, with

some cells crossing over the midline and spreading in the wrong direction. (H) *ths* and (J) *pyr* mutants spread directionally away from the midline toward dorsal regions.

Quantitative analysis shows that *ths* and *pyr* mutants both display intercalation defects

To further characterize the non-monolayer phenotype of *pyr* and *ths* mutants, we focused on the small cell movements/rearrangements found in intercalation, as the non-monolayer in *pyr* mutants cannot be accounted for by a collapse defect. In this particular case, we investigated whether intercalation events might support the generation of the mesoderm monolayer during gastrulation (Figure 5A). We quantified the rate and number of intercalation events in wild-type and mutant backgrounds to see if mesoderm intercalation is dependent on FGF signaling and if the timing of intercalation corresponds with monolayer formation. Monolayer formation occurs during stage 9 and 10 and involves the transformation of a multi-layer into a single cell layer (~80-90 minutes into migration; Figure 5B,C).

By focusing on the position of mesoderm cells during stage 9 and 10 (grey spots in Figure 5), it is apparent that a subset of cells is not incorporated into the monolayer in *pyr*, *ths*, and *htl* mutants (Figure 5D-I, arrowheads). We used the tracking data from each mutant to examine the timing and number of intercalation events. We found that *pyr* has a reduced number of intercalation events compared to wild-type, that *ths* mutants have even less intercalation events than *pyr*, and that *htl* mutants have the fewest events (Figure 5J; number of cells assayed are 303, 241, 262, and 213 for wild-type, *pyr*, *ths*, and *htl*, respectively, with $p < 0.002$ in all cases). Together, these data suggest that the

presence of FGFs throughout the ectoderm is important for intercalation of all mesoderm cells to form a monolayer. The defects did not necessarily correspond with the particular expression pattern of each ligand. This is not surprising as ligands, including FGF8, may have non-autonomous effects due to diffusion (e.g., Yu et al., 2009).

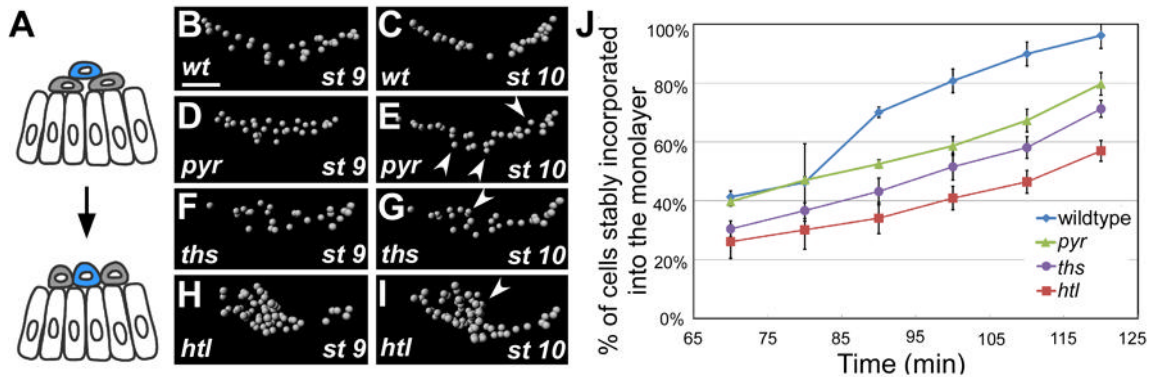


Figure 5. Intercalation of mesoderm cells during monolayer formation is disrupted in FGF mutants. (A) Intercalation occurs during mesoderm migration when a cell that is not in contact with the ectoderm (blue) moves toward the ectoderm. (B-I) A subset of mesoderm cells are tracked from (B,D,F,H) stage 9 to (C,E,G,I) 10 (grey ball = mesoderm cell), showing how cells go from a multilayer to a monolayer in (B,C) wild-type embryos, but not in (D,E) *pyr*, (F,G) *ths*, or (H,I) *htl* mutants. Arrowheads demonstrate cells that have not intercalated. The view shown is similar to a cross section like in Fig. 2. Scale bar = 20 μ m. (J) A graph of stable intercalation of mesoderm cells over time. The number of cells that intercalate stably into the monolayer is highest for wild-type embryos, while *pyr*, *ths*, and *htl* mutants have successively lower numbers of intercalating cells. All four phenotypes shown are statistically different ($p < 0.002$).

It has been previously shown that Htl, Pyr, and Ths can influence cellular projections during collapse and spreading (Schumacher et al., 2004; Wilson et al., 2005;

Klingseisen, A. et al., 2009). Since migratory defects often coincide with a failure to regulate cell shape changes and protrusive activity (McDonald et al., 2008), we examined whether the ligands control cell shape changes that may also be important for movement during monolayer formation. We visualized the protrusions using twist promoter supported expression of CD2, a cell-surface protein not native to *Drosophila*, which permits examination of cell extensions exclusively in the mesoderm during stage 9 and 10 (Dunin-Borkowski and Brown, 1995). We found that, as previously published, the leading edge is affected at stage 9, as cells fail to polarize in embryos lacking both Pyr and Ths or in *pyr* single mutants (arrow, Figure S2A-C in supplementary materials), but not in *ths* single mutants (Klingseisen, A. et al., 2009). Similar effects are observed when the ligands are ectopically expressed in the mesoderm: overexpression of *pyr* leads to severe loss of cellular extensions, whereas overexpression of *ths* has a minor effect (Klingseisen, A. et al., 2009).

It has been previously shown that Htl, Pyr, and Ths can influence cellular projections during collapse and spreading (Schumacher et al., 2004; Wilson et al., 2005; Klingseisen et al., 2009). Since migratory defects often coincide with a failure to regulate cell shape changes and protrusive activity (McDonald et al., 2008), we examined whether the ligands control cell shape changes that may also be important for movement during monolayer formation. We visualized the protrusions using twist promoter supported expression of CD2, a cell-surface protein not native to *Drosophila*, which permits examination of cell extensions exclusively in the mesoderm during stage 9 and 10 (twist-CD2; Dunin-Borkowski and Brown, 1995). We found that, as previously published, the leading edge is affected at stage 9, as cells fail to polarize in embryos

lacking both *Pyr* and *Ths* or in *pyr* single mutants (arrow, Figure S2A-C in supplementary materials), but not in *ths* single mutants (Figure S2D in supplementary materials; Klingseisen et al., 2009). Similar effects are observed when the ligands are ectopically expressed in the mesoderm: overexpression of *pyr* leads to severe loss of cellular extensions, whereas overexpression of *ths* has a minor effect (Figure S2E-F in supplementary materials; Klingseisen et al., 2009).

On the other hand, it had not been examined previously whether mesoderm cells extend protrusions towards the ectoderm during monolayer formation. We found that, in the *pyr/ths* double mutant, mesoderm cells extend fewer large protrusions into the ectoderm than in wild-type embryos (arrowheads, Figure S2A,B in supplementary materials). Mesoderm sections from double mutant embryos contained 4.0 ± 0.8 protrusions per image (N=11) while those from wild-type exhibited 7.7 ± 0.9 protrusions (N=11, $p < 0.01$). *pyr* and *ths* single mutants also failed to extend as many protrusions into the ectoderm (Figure S2C,D in supplementary materials; 4.3 ± 0.9 and 4.8 ± 1.5 , respectively, N=9 for each; $p < 0.01$ for each compared to wild-type). These data suggest that protrusive activity may be important for monolayer formation and provide insights into the mechanism by which FGF signaling may control radial intercalation.

Myospheroid activity is required for monolayer formation and is controlled by Rap1

After characterization of the FGF mutants, we sought out other genes that produce similar phenotypes to the FGF mutants by preliminary screening in fixed sections. To this end, we discovered that embryos mutant for the GTPase Rap1 have collapse and

monolayer formation defects similar to those mutant for Htl (Figure 6A-C and E-G). However, *Rap1* mutants also exhibit defects in ventral furrow formation and germband elongation, making the interpretation of its primary roles in mesoderm migration difficult (Roote and Zusman, 1995; Asha et al., 1999). Therefore, we sought out targets of Rap1 that displayed more specific mesoderm migration defects.

Several studies suggest that Rap1 is required for activation of integrins at the cell membrane, which in turn is required for cell adhesion and migration (rev. in Bos, 2005; Boettner and Van Aelst, 2009; Vicente-Manzanares et al., 2009). This led us to explore the role of integrins during mesoderm migration in *Drosophila*. There are two beta integrin subunits in *Drosophila*, but only the subunit β PS1, Myospheroid (Mys), is expressed during mesoderm migration: in between the mesoderm and ectoderm at stage 9 and 10 (Figure S3A-G in supplementary materials; Leptin et al., 1989; Gotwals et al., 1994).

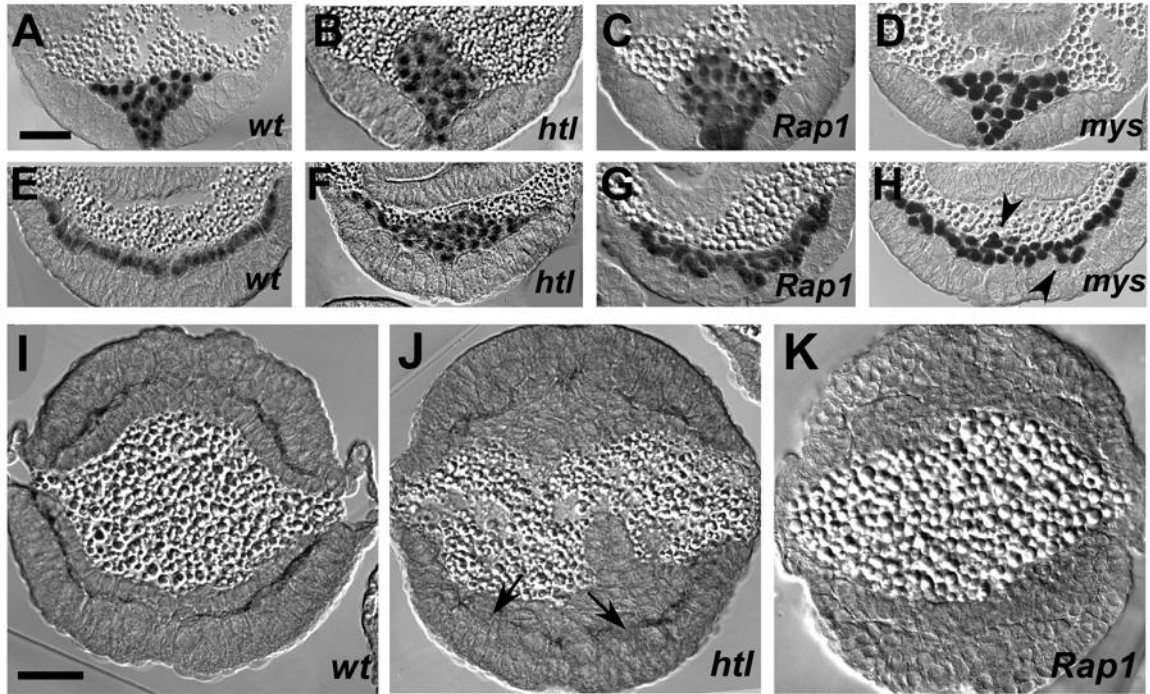


Figure 6. Rap1 and Mys are required for monolayer formation. (A-H) Cross sections of embryos stained with twist antibody (black). (A-D) Stage 7 embryos and (E-H) Stage 10 embryos. (A,E) Wild-type embryos undergo tube collapse at (A) stage 7 and then intercalation to form a monolayer during (E) stage 10. (B-D,F-H) In (B) *htl* mutants and (C) *Rap1* mutants, tube collapse is defective, resulting in a clump of cells at stage 7. Intercalation is also affected, resulting in the lump remaining at (F,G) stage 10. In *mys* mutants, tube collapse is normal, resulting in normal mesoderm behavior at (D) stage 7. (H) During stage 10 a non-monolayer is observed (arrowheads). (I-K) Cross sections of embryos at stage 10 stained with Mys antibody (black). (I) In wild-type embryos, Mys is expressed at the boundary between the mesoderm and ectoderm. (J) In *htl* mutants, Mys levels are reduced and gaps in expression are observed (arrows). (K) *Rap1* mutant embryos fail to localize Mys at the ectoderm-mesoderm boundary. Scale bar = 20 μm.

We found that *mys* mutants exhibit a non-monolayer mesoderm defect at stage 9 and 10 in fixed sections (Figure 6D,H). In addition, we found that Mys localization is affected in *htl* and *Rap1* mutants, with gaps and reduced expression of Mys in *htl* mutants and a total absence of Mys in *Rap1* mutants (Figure 6I-K). These results suggest that Mys plays a specific and crucial role during monolayer formation. To definitively test the role of Mys in intercalation we dissected the phenotype using quantitative imaging methods.

Myospheroid mutants exhibit a decrease in intercalation events during mesoderm migration

We performed live imaging on H2A-GFP embryos injected with a translation blocking morpholino designed against the *mys* transcript (Figure S3H-K in supplementary materials). The Mys morpholino was able to reproduce the phenotype of the genetic null and also eliminate Mys protein expression in the embryo (Figure S3L,M in supplementary materials). We tracked a subset of mesoderm cells from *mys* mutant imaging data and analyzed movement in r and θ (Movie 3 in supplementary materials). We found that neither collapse (r) nor spreading (θ) is affected by loss of Mys (Figure 7A,B). Like the FGF ligand mutants, we found a reduced number of intercalation events during monolayer formation in *mys* mutants compared to wild-type (Figure 7C,F,G; 90 cells were assayed for *mys* mutants, $p < 0.05$). We also found that mesoderm membrane protrusions into the ectoderm were completely absent in *mys* mutants during the same time interval as monolayer formation (i.e. stage 9 and 10), which could be contributing to the observed intercalation defects (Figure 7D,E). Our data indicate that Mys is important

for monolayer formation and provide support for the view that this migratory event is molecularly distinct from earlier events, as ventral furrow formation, collapse, and spreading are unaffected in *mys* mutants.

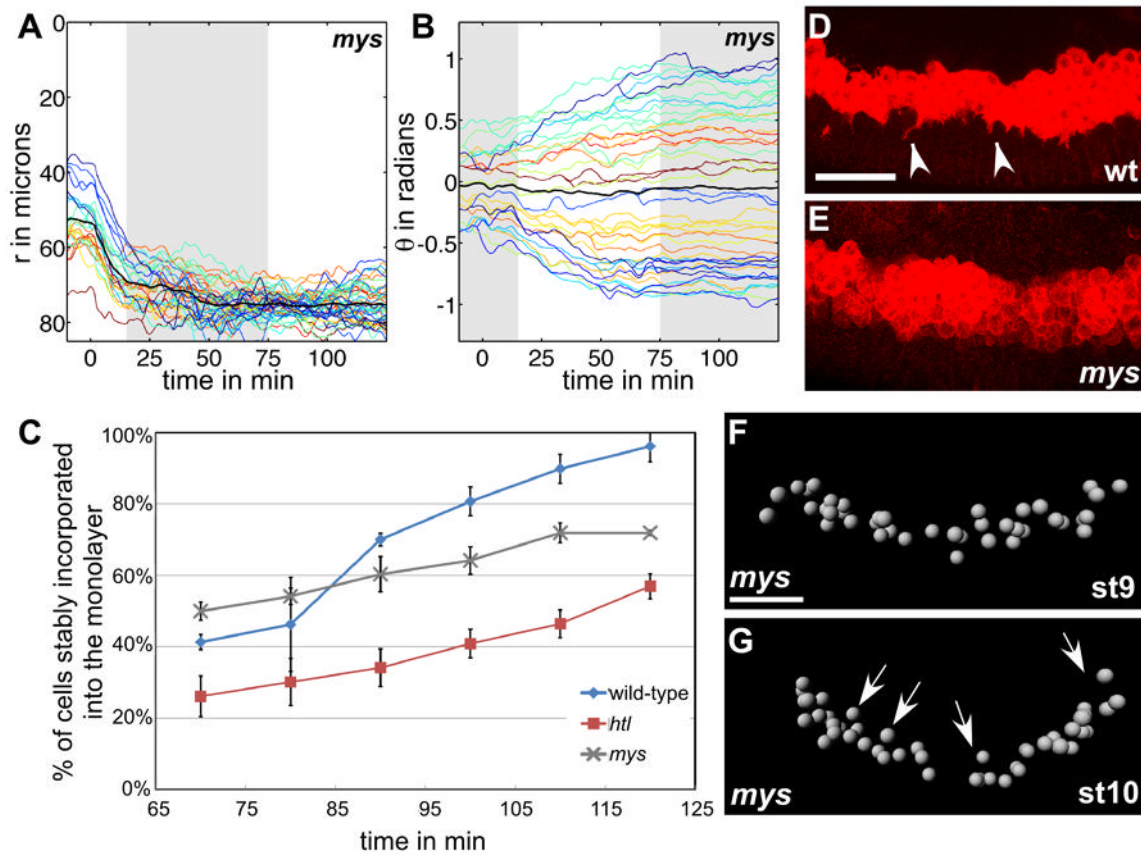


Figure 7. Mys is required for monolayer formation and mesoderm cell shape changes.

(A,B) Collapse and spreading of mesoderm cells in *mys* mutants represented by r and θ over time, respectively (see Figure 4 for more details). A radial color code is applied to distinguish each cell track over time. The black line represents the average behavior of all mesoderm cells. (C) Monolayer formation is measured as the percent of cells that are incorporated by stable intercalation into the monolayer over time. *mys* mutants exhibit a lower number of intercalation events than wild-type embryos, but a higher number than *htl* mutants. (D,E) Lateral projections of stage 9 twist-CD2 embryos stained with CD2 antibody, which marks cellular protrusions in the

mesoderm. **(D)** Wild-type mesoderm cells extend membrane protrusions into the ectoderm during monolayer formation (arrowheads). **(E)** *mys* mutants exhibit rounded mesoderm cells with no protrusions into the ectoderm. Scale bar = 20 μm . **(F,G)** A subset of mesoderm cells are tracked from stage (E) 9 to (F) 10 (grey ball = mesoderm cell). The view shown is similar to a cross section like in Fig. 2.

DISCUSSION

Mesoderm migration is a composed of a series of movements in different directions

Mesoderm migration in *Drosophila* is a combination of complex three-dimensional movements involving many molecular components. We have demonstrated here that live imaging, coupled with quantitative analyses, is important for studying complex cell movements, as it allowed us to decompose migration into different movement types and thus to describe subtle phenotypes. First, we extended analysis of the directional movements of mesoderm cells within wild-type embryos, focusing on the temporal sequences of events. We found that cells follow a sequential and distinct set of trajectories: movement in the radial direction (tube collapse: -5 to 15 min, 0 = onset of germband elongation), followed by movement in the angular direction (dorsal migration: 15 to 75 min), and ending with small intercalation movements in the radial direction (monolayer formation: 75 to 110 min). These movements appear temporally distinct (i.e. stepwise), and thus we searched for molecular signals controlling each process.

FGF signaling controls tube collapse and intercalation to specify a monolayer

We investigated which particular movements were FGF-, and in particular either Ths- or Pyr-, dependent. The interaction between Htl and its two ligands provides a simpler system relative to vertebrates (which exhibit over 120 receptor-ligand interactions) in which to study how and why multiple FGF ligands interact with the same receptor. Previously, we had found that FGF signaling, via the Htl FGFR, controls collapse of the mesodermal tube but not dorsal-directed spreading (McMahon et al., 2008). Here we demonstrated that FGF signaling is also required for monolayer formation. In addition, we defined distinct, non-redundant roles for the FGF ligands: Ths (but not Pyr) is required for collapse of the mesodermal tube, while both Pyr and Ths are required for proper intercalation of mesoderm cells after dorsal spreading (i.e. stage 9/10).

This analysis raises questions about ligand choice during collapse and monolayer formation. Within the mesodermal tube, cells at the top require a long-range signal in order to orient towards the ectoderm during tube collapse, while the signals controlling intercalation during monolayer formation can be shorter-ranged. We suggest that the ligands have different activities that are appropriately tuned for these processes. In fact, recent studies of the functional domains of these proteins suggest that Ths has a longer diffusion range than Pyr (Tulin and Stathopoulos, in review), in agreement with our analysis that Pyr does not support tube collapse, but does have a hand in monolayer formation.

Rap1 and Myospheroid are essential for monolayer formation

We have demonstrated here that *Rap1* mutants have a similar mesoderm phenotype to the FGFR *htl* mutant, with defects in collapse and monolayer formation. We were unable to establish whether Rap1 acts downstream of FGF signaling, as the complete loss of Mys in *Rap1* mutants is more severe than the patchy expression of Mys seen in *htl* mutants. Therefore, Rap1 could be working in parallel to or downstream of FGF signaling during mesoderm migration. Rap1 has been implicated in several morphogenetic events during *Drosophila* gastrulation, and likely interacts with many different signaling pathways (Roote and Zusman, 1995; Asha et al., 1999). Further study of Rap1, along with other GTPases, will shed light onto their role during mesoderm migration, how they interact with one another, and what signaling pathways control them.

We chose to focus on the more specific phenotype of *mys* mutants, as its localization is affected in *htl* mutants and it exhibits a monolayer defect that is similar to *pyr* and *ths* mutants. Integrins are important for cell adhesion, so it is not surprising that cells fail to make stable contact with the ectoderm through intercalation in *mys* mutants. However, some cells do contribute to monolayer formation in the absence of Mys, implying that other adhesion molecules are involved in maintaining contact between the mesoderm and ectoderm. These other molecules may be activated downstream of FGF signaling, as the *htl* mutant monolayer phenotype is more severe than the *mys* mutant. Discovering the downstream targets of Htl will help to shed light on other components that contribute to both collapse, which is not dependent on Mys, and monolayer formation, which is Mys-dependent.

Cell shape changes are important for monolayer formation

Cell protrusions, such as filopodia, are important for sensing chemoattractants and polarizing movement during migration (rev. in Mattila and Lappalainen, 2008). Previous studies have shown that protrusive activity exists at the leading edge during mesoderm migration in *Drosophila* and that these protrusions are FGF dependent (Schumacher et al., 2004; Klingseisen et al., 2009). In this study, we have found that protrusions exist in all mesoderm cells, not just the leading edge, and that these protrusions also extend into the ectoderm.

Our study demonstrates that FGF signaling as well as integrin activity enhance protrusive activity into the ectoderm; this is a potential mechanism by which FGF signaling and Mys could control movement toward the ectoderm during monolayer formation. The function of the protrusions at the leading edge remains unclear, as they appear to be reduced in *pyr* and *mys* mutants (Figure S2), but migration in the dorsal direction still occurs in both mutant backgrounds. One interpretation is that FGF and Mys are important for generalized protrusive activity, and that extensive protrusions are required for intercalation but not dorsal migration.

Mesoderm Migration Involves Four Distinct Steps

Based on our study, we propose mesoderm migration is stepwise, with each event requiring different molecular cues to achieve collective migration (Figure 8). Invagination of the mesoderm is the first step in this process, and is dependent on Snail, Twist, Concertina, Fog, and several other genes (Parks and Wieschaus, 1991; Reuter and

Leptin, 1994; Morize et al., 1998; Aracena et al., 2006; Seher et al., 2007; Martin et al., 2009). Next, collapse of the mesoderm tube onto the ectoderm requires Htl activation via Ths. Rap1 may be involved in this process as well, but the phenotype of *Rap1* mutants is quite complex and it is unclear which phenotypes are primary defects (See Figure 6C,G; Roote and Zusman, 1995; Asha et al., 1999).

Following collapse, mesoderm cells spread dorsally by an unknown mechanism. Dorsal migration is unaffected in *pyr* and *ths* mutants, and occurs in all cells that contact the ectoderm in *htl* mutants, implying that FGF signaling is at most indirectly involved in this step due to the earlier tube collapse defect (McMahon et al., 2008). Whether dorsal migration requires chemoattractive signals or whether the cells simply move in this direction because it is the area of least resistance remains unclear. Finally, after dorsal spreading is complete, any remaining cells not contacting the ectoderm intercalate to form a monolayer. This process is controlled by a combination of both Pyr and Ths interacting through Htl and also by Rap1 and Mys. In other systems, intercalation can lead to changes in the properties of the collective, for instance lengthening of a body plan (Keller, 2006). However, we have shown here that dorsal migration/spreading is not a result of intercalation, as intercalation occurs after spreading has finished (Figure 5).

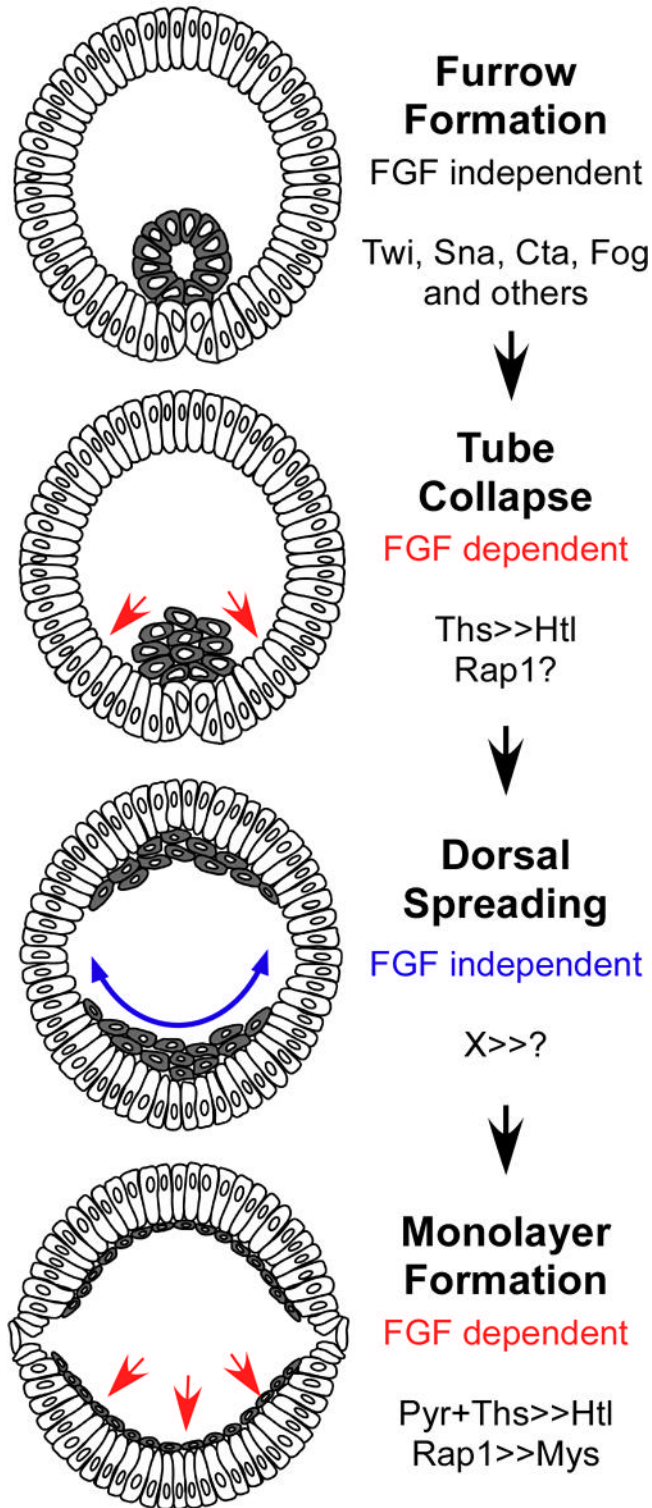


Figure 8. Multi-step model of mesoderm migration. Formation of the ventral furrow occurs first during gastrulation. This process depends on many inputs, such as Twist, Snail, Concertina,

Fog. Following furrow and tube formation, the mesoderm collapses onto the ectoderm, which is dependent on FGF signaling through Thisbe. Rap1 may also be involved. Subsequently, directed dorsal spreading occurs, and it appears to be independent of FGF signaling. Lastly, monolayer formation by intercalation is FGF dependent and requires both ligands. Rap1 controls Mys, which in turn is required for monolayer formation.

Coordination of these signals to control collective migration enables the mesoderm to form a symmetrical structure, which is essential for embryo survival. This model begins to address the question of how hundreds of cells move in concerted fashion and is relevant for a generalized understanding of embryogenesis and organogenesis. We find that mesoderm migration is accomplished through sequential movements in different directions, implying that collective migration may be best achieved by distinct phases of movement.

Chapter 5:

Discussion

The purpose of my thesis work has been to gain an understanding of collective migration using the mesoderm of the *Drosophila* embryo as a model. We sought to bring the study of mesoderm migration up to the standard of other models, such as border cell migration in the fly or lateral line migration in zebrafish (see introduction for discussion of these models). To do this, we had to first develop a method for examining mesoderm migration in vivo, as described in Chapter 2. We tailored two-photon microscopy techniques to the *Drosophila* embryo such that we could image thousands of cells in motion with sufficient spatial and temporal resolution for further computational analysis. We then developed methods to quantify migratory behavior by utilizing tracking software and custom-made scripts so that we could decompose the three-dimensional complexity of mesoderm migration into manageable pieces.

To validate this in vivo approach, we had to go back to the first well-studied mutant, the fibroblast growth factor (FGF) receptor mutant *heartless* (*htl*), to determine if we could make advances in the field that were previously unattainable. In Chapter 3, we demonstrate that we could indeed describe the *htl* mutant phenotype accurately for the first time using the approach in Chapter 2. We found that in the absence of Heartless, collective migration is lost as two populations of migratory cells emerge. We discovered that Heartless is required for all mesoderm cells to contact the ectoderm and that cells that do not contact the ectoderm are unable to move directionally. Thus, we found that the initial function of FGF signaling in mesoderm migration is to bring cells into contact with the ectoderm during tube formation so that they can move collectively toward the dorsal side of the embryo.

Our next step was to determine the functions of the two ligands, Pyramus and Thisbe (Pyr and Ths, respectively), during mesoderm migration in order to address several questions about FGF signaling during migration. In Chapter 4, we investigated whether each ligand was required for migration, whether different pathways downstream of FGF were activated during movement, and whether there were additional roles for FGF during collective migration that were unapparent in the initial study. We found that indeed each ligand is required for mesoderm migration, specifically migration in the radial direction, but that Thisbe plays a larger role than Pyramus. We also found that FGF signaling is not only required for collapse of mesoderm cells onto the ectoderm, but that it is also necessary for intercalation of cells during monolayer formation. Both processes are crucial for setting up mesoderm cells to be in the correct place for later developmental functions. Lastly, we discovered other inputs into radial migration: Rap1, a small GTPase, and its downstream target β PS1 integrin (Myospheroid). We found that Myospheroid is important for intercalation, establishing that monolayer formation is a molecularly distinct process from the other radial motion of mesoderm tube collapse.

Collective Migration: Justification for using the mesoderm as a model

Several models for migration (both individual and group migrations) exist and many are fairly well characterized (Rorth, 2009). The logical question, then, is why adding additional models will advance the field. There are two particularly important reasons for having many distinct models. Firstly, it is already apparent that although there are underlying themes for migration, different types of migration require different molecules to achieve similar goals. For instance, border cells follow epidermal growth

factors and platelet-derived growth factors on their journey for one end of an egg chamber to another, while *Dictyostelium* cells migrate in response to cyclic AMP and folate. Whether these different signaling molecules elicit similar downstream responses in migrating cells has yet to be fully realized and it is only by studying many models that this will become apparent. Secondly, migration of cells occurs in disparate environments, so studying how cells move in an open, two-dimensional environment is most likely not sufficient for understanding migration in an environment choked with extracellular matrix molecules. We, therefore, present mesoderm migration as a model for studying how hundreds of cells can move in concert in three dimensions. This type of migration has been underrepresented in collective migration studies because of the difficulty in assaying many cells moving in three dimensions. The advances in imaging and analysis, however, finally allow us to quantify the behavior of these cells, making mesoderm migration a tractable model for studying collective movement. We think that this model is very relevant for understanding gastrulation and organ formation, as many migrations involve movements of very large groups of cells moving in concert.

The Three steps of Mesoderm Migration

Because we are the first group to fully characterize wild-type mesoderm migration in *Drosophila*, we have only recently discovered that movement of the mesoderm during gastrulation is a multistep process presumably controlled by many different inputs. We have found that these steps, (i) collapse, (ii) dorsal spreading, and (iii) monolayer formation, require separate chemical cues.

Even before migration begins, the mesoderm furrow must first invaginate to form a tube. This process is dependent on Twist, Snail, Folded-Gastrulation and Concertina, which together control regulated apical constriction resulting in furrow formation (Morize et al., 1998; Martin et al., 2009). Collapse of the mesoderm onto the ectoderm, the first step of migration, is an FGF-dependent process, with Thisbe controlling the majority of collapse (see below for discussion of FGF specificity).

The molecules that control dorsal spreading remain uncharacterized, but our results suggest that it is an FGF independent event. There is some preliminary evidence that suggest this process may be controlled by activation of Rac GTPase through the RhoGEF Pebble (Trisnadi and Stathopoulos, unpublished observations). What is upstream of Rac remains to be found and will resolve the question of whether dorsal migration is a directed process (i.e., guided by chemoattractants) or if the migration is only controlled by the availability of space, with cells spreading out to occupy gaps along the ectoderm.

The last step of mesoderm migration, monolayer formation, requires FGF signaling and is dependent on the presence of both ligands in the ectoderm. We were able to characterize additional component, the β integrin Myospheroid, which is also required for monolayer formation. We plan to use gene expression profiling and proteomics to find additional components downstream and independent of FGF that play a role during collapse and monolayer formation.

During mesoderm migration, there are other events that still remain uncharacterized. For instance, during migration there are two spatially and temporally controlled waves of cell divisions (McMahon et al., 2008). This precise regulation of cell

divisions may aid in keeping migration from becoming overly disrupted by division events, although the exact reason for this control remains to be seen. It also remains unclear what molecules are responsible for the epithelial-to-mesenchymal transition (EMT) that occurs during collapse of the mesoderm tube. There is clearly a switch from E-cadherin to N-cadherin during this time, which could be the cause of the loss of epithelial characteristics (Akiyama-Oda et al., 2000). However, the mesoderm does seem to retain some epithelial-like features, hinting at an incomplete EMT, as there is some residual E-cadherin and the cells seem to remain attached during migration (Oda et al., 1998). It seems unlikely that the EMT is controlled by FGF signaling or Pebble, as both the mesoderm in both mutants is able to collapse to some degree onto the ectoderm (Schumacher et al., 2004). Further characterization of additional candidate genes like Rac and Pebble combined with larger screens will help to identify additional inputs into mesoderm movement at different stages of migration.

Specificity in Fibroblast Growth Factor Signaling

FGF signaling plays a pivotal role in development: guiding migration and differentiation in many cell types (Thisse and Thisse, 2005). The prevalence of FGF signaling during development makes it crucial to understand the details of this pathway in order to combat disease. *Drosophila* offers an exceptional model for studying FGF signaling, as it offers a simplified version of ligand-receptor interactions; there are hundreds of interactions in mammals versus the three interactions in *Drosophila* (Huang and Stern, 2005; Kadam, S. et al., 2009). Therefore, we examined the FGFR Heartless

and the two ligands Pyramus and Thisbe and how they are involved in mesoderm migration as a model for signal specificity.

In the FGF field, it remains unclear whether ligands act specifically by, for instance, activating only differentiation or migratory cellular responses. By combining our studies with others (Franzdottir et al., 2009), it has become apparent that the two ligands Pyramus and Thisbe can influence both differentiation and migration, implying that there is at least some amount of redundancy. Interestingly, in the two most well characterized systems in *Drosophila*, mesoderm migration and glial cell migration, each ligand seems to have distinct, dominant roles. In glial cell migration, Pyramus guides migration while Thisbe controls differentiation (Franzdottir et al., 2009). The roles of the ligands are reversed, surprisingly, during mesoderm development, with Thisbe being more important for migration while Pyramus controls heart cell differentiation (Kadam, S. et al., 2009). This may be related to the nature of the ligands, as Pyramus and Thisbe seem to be processed differently and have different activity ranges (Tulin and Stathopoulos, unpublished observations).

Studying both models has led to the idea that different pathways downstream of FGF control differentiation versus migration, implying that there is some switch that occurs to bias which pathway is activated. The small GTPase Rap1 may control migratory behavior downstream of FGF, as we found that loss of Rap1 and Heartless produce similar phenotypes. In glial cell migration, it was also found that *Rap1* mutants produced a migratory phenotype like in *pyr* mutants. Ras1, another small GTPase, is results in MAP kinase activation and a differentiation output. Our studies, however, do not support the idea that only Pyramus or Thisbe control Rap1 or Ras1 downstream of the

FGFR, as both ligands are involved in migration and differentiation, so some additional input must be required to control which pathways are active. This input may be direct, such as a change in how the ligands or receptor are processed resulting in differential activation of Heartless, or indirect, with another signaling pathway providing regulatory inputs into the FGF pathway.

Although the ligands can control the same downstream pathways, there is some preliminary evidence that the ligands can in fact activate Heartless to different degrees, with Pyramus eliciting a stronger response than Thisbe (Tulin and Stathopoulos, in review). This is also apparent in mesoderm migration, as overexpression of Pyramus in the mesoderm or ectoderm causes a stronger phenotype than overexpression of comparable amounts of Thisbe (Kadam et al., 2009). We found that the levels and spatial domains of Pyramus and Thisbe are crucial to proper mesoderm migration and that we were unable to substitute one ligand for the other, implying that each ligand has unique properties. Future studies of the ligands themselves through biochemical assays with a focus on binding kinetics will shed light onto the reasons for the disparity in ligand function.

Future Directions: Large Scale Imaging Studies

We have made the first steps toward the future of studying migration: utilizing high-resolution imaging and tracking programs to decipher migratory behavior. Using quantitative imaging we have for the first time fully characterized wild-type mesoderm migration and begun to understand the underlying mechanisms through the study of FGF signaling. This technique is applicable to all studies of migration dynamics, and we

predict it will become routine as the process becomes more streamlined. In addition, live studies of cellular protrusions and actin reorganization, as well as being able to quantify signal transduction in vivo, will strengthen this technique even further (Pertz and Hahn, 2004). As the technology improves, we will be able to move toward larger-scale screens, where the process of imaging and analysis will become commonplace and be combined with preliminary fixed-section analyses, and we can focus on deciphering the exact mechanisms of migration during development and disease (Chuai et al., 2009).

Appendices

Appendix A: Supplementary Materials for Chapter 2

All supplementary data is available online through Nature Protocols at the following address:

http://www.nature.com/nprot/journal/v4/n10/supinfo/nprot.2009.130_S1.html

Supplementary Data 1. Matlab scripts.

See Table 2 for details.

Supplementary Data 2. Sample datasets.

Mesoderm, ectoderm, and midline tracking sample datasets are included.

Supplementary Movie 1.

3D image of an entire *Drosophila* embryo at the onset of mesoderm cell spreading. This movie shows the good signal obtained from the mesoderm tube. The nls-GFP signal is diffuse during cell division (see the anterior pole). This dataset has been acquired in slightly different conditions compared to the rest of this protocol to image the embryo with a larger field of view using a 20x 0.95NA objective from Olympus. The nls-GFP *Drosophila* embryo (Bloomington Stock Center, stock number 5623) has been imaged on a TriMScope 2PEF setup provided by LaVision BioTech company.

Supplementary Movie 2.

3D schematic animation of quantitative imaging of *Drosophila* embryos. This movie successively shows (i) the *Drosophila* embryo shape and body plan with the position of the midline; (ii) the position of the image acquisition field of view on the ventral side of the embryo; (iii) the position and shape of the ectoderm and mesoderm layers at the onset of mesoderm spreading, with a representation of the ventral furrow; (iv) a 3D view of the cylindrical coordinate system adapted to the shape of the embryo in the imaging area; (v) a 3D representation of morphogenetic movements showing the ectoderm convergence-extension during germband extension (GBE), the mesoderm furrow collapse and the mesoderm spreading.

Supplementary Movie 3.

Example of angular drift during image acquisition. View of the ectoderm layer from the ventral side in H2A-GFP expressing embryos. Arrow indicates the position of midline cells and highlights the angular drift. It corresponds to the drift corrected in Figure 5. The specific shape of the nuclei from midline cells (elongated along the anterior-posterior axis) is clear. Anterior-posterior axis is vertical, posterior is up.

Appendix B: Supplementary Materials for Chapter 3

All supplementary data is available online through Science Magazine at the following address:

<http://www.sciencemag.org/cgi/content/full/sci;322/5907/1546/DC1>

I. Supplemental Figures

Figure S1. Coordinate systems used during imaging and analysis processes.

Figure S2. Virtual cross-sections and tracking data for H2A-GFP embryos in wild-type and *htl* mutant backgrounds.

Figure S3. Decomposition of movement, correlation data and ectoderm subtraction for *Heartless* mutant embryos.

Figure S4. Spreading consistency analysis: $\theta_{\text{start}}(\theta_{\text{end}})$ graphs.

Figure S5. Spreading consistency analysis: table of linear regression and main conclusions.

Figure S6. Wild-type and *klarschist* embryos show similar morphology in fixed sections.

Figure S7. Disrupting the spatial or temporal patterns of division in the mesoderm does not affect the spreading pattern.

II. Movies Legends

Movie S1: Two-photon excitation of ubiquitous H2A-GFP in early embryos.

Movie S2: Segmentation and tracking of mesoderm nuclei in wild-type embryos using Imaris software.

Movie S3: 3D tracks of mesoderm and ectoderm cells over time.

Movie S4: Visualization of cylindrical coordinate system.

Movie S5: Ectoderm subtraction in a wild-type embryo (simulation).

Movie S6: Ectoderm subtraction in a wild-type embryo (experimental data).

Movie S7: Wild-type data along radial and angular axes (theta color code).

Movie S8: Wild-type data along radial and angular axes (radial color code).

Movie S9: Segmentation and tracking of mesoderm nuclei in *htl* mutant.

Movie S10: *htl* data along radial and angular axes (theta color code).

Movie S11: *htl* data along radial and angular axes (radial color code).

I. Supplemental Figures

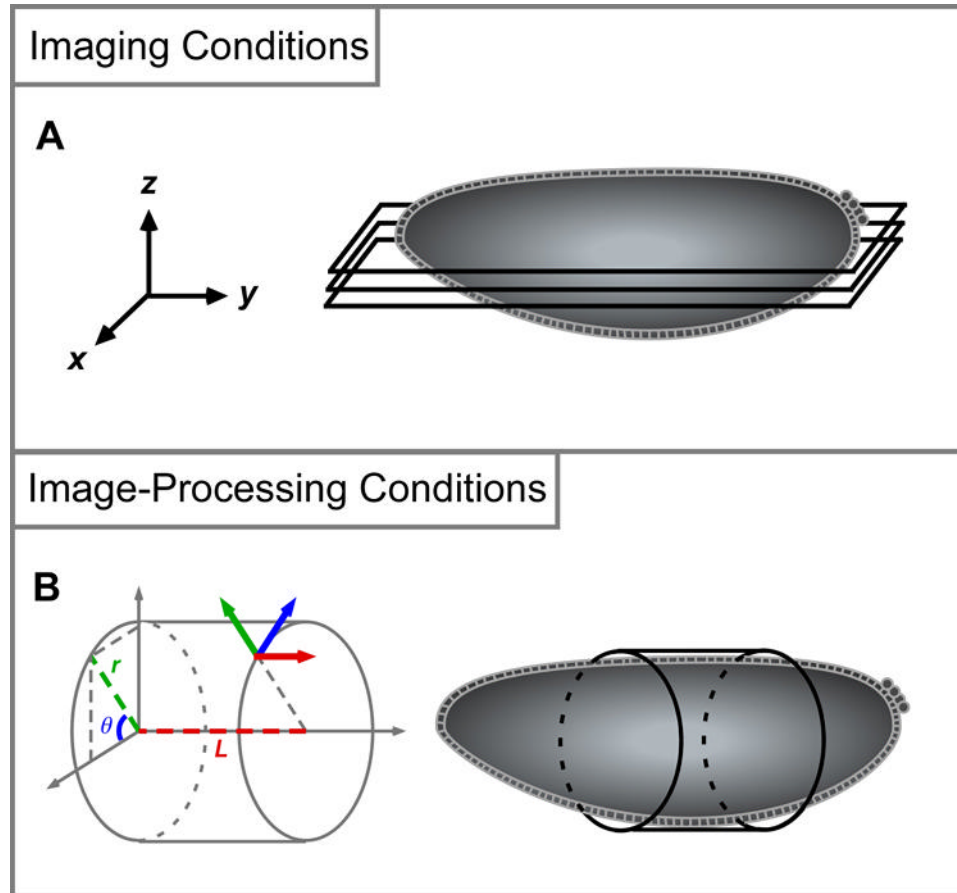


Figure S1. Coordinate systems used during imaging and analysis processes.

(A) Stacks of two-photon images are collected using traditional Cartesian coordinates (x , y , z). This system works well for imaging in 3D space and is employed in most microscope setups. Initial tracking data created with Imaris also uses this coordinate system. (B) During image processing, we change to a cylindrical coordinate system (r , θ , L) to conform roughly to the body plan of the embryo, which makes analysis of each morphogenetic movement along each axis more straightforward. r corresponds to the

radial position of each cell over time (e.g., furrow collapse, intercalation). The 0 value of r defines the center of the embryo. θ represents the angular movement of cells (spreading). The 0 value of θ is determined experimentally as the position of the embryonic ventral midline (see Materials and Methods for additional information). L corresponds to the location of cells along the anterior-posterior axis (germband elongation).

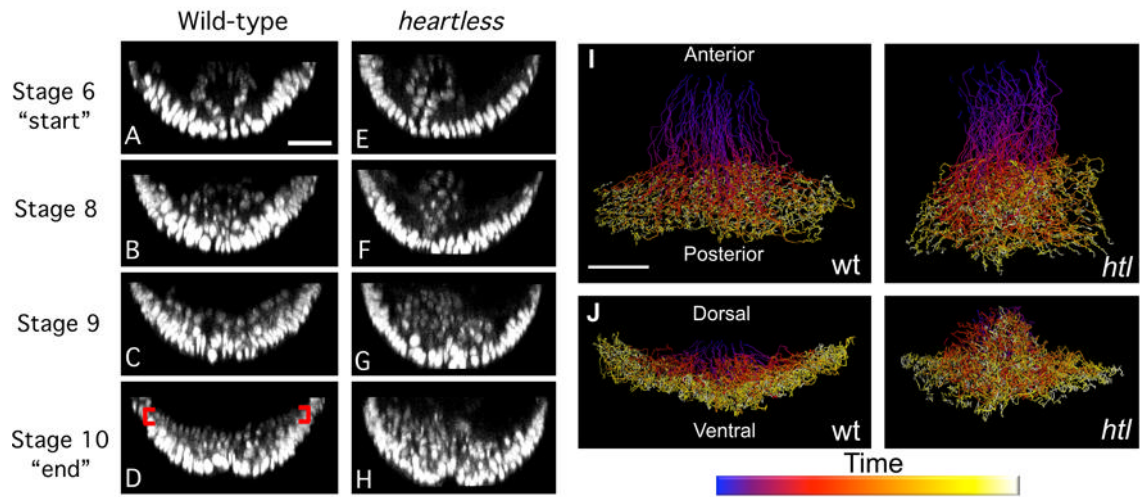


Figure S2. Virtual cross-sections and tracking data for H2A-GFP embryos in wild-type and *htl* backgrounds. (A–H) 5 μm thick cross-sections through H2A-GFP data were created using Imaris software. Mesoderm cells can be observed inside of the embryo at each stage, and each main morphogenetic event is represented: furrow formation (stage 6; A,E), the collapse of the furrow (stage 8; B,F), spreading (stage 9; C,G), and formation of the monolayer (stage 10; D,H, red brackets). *htl* mutant embryos, also expressing H2A-GFP, show defects in mesoderm spreading similar to those documented in the literature. Nuclei were tracked over time using Imaris. (I) Dorsal view of tracking data in wild-type and *htl* embryos. (J) Posterior view of tracks from wild-type and *htl* embryos. Time is represented by color (purple=early, yellow=late). Scale bar = 20 μm .

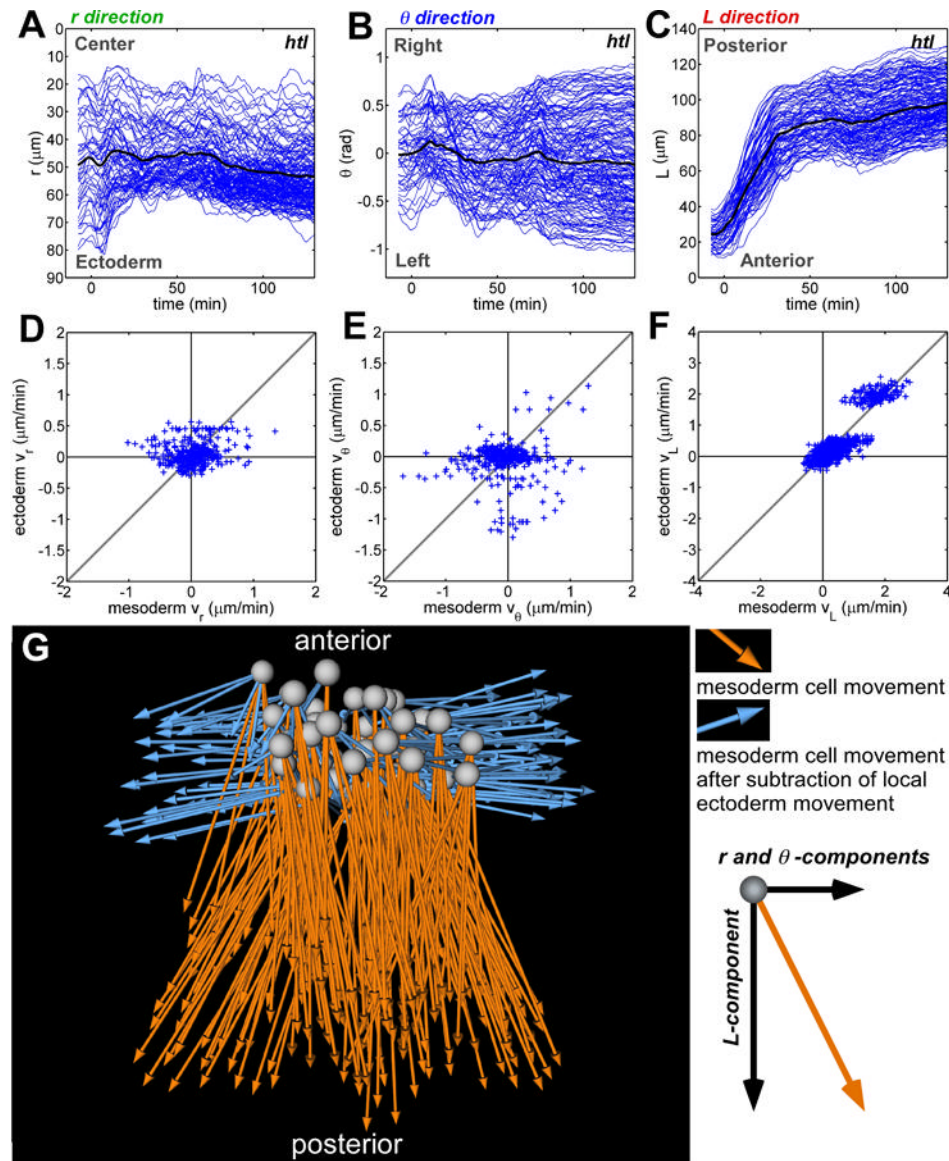


Figure S3. Decomposition of movement, correlation data and ectoderm subtraction for *htl*. Cylindrical coordinates are used to position cells according to the body plan of embryo at stage 6. Each axis of the cylinder corresponds to a specific morphogenetic movement: (A) r corresponds to the radial position of each cell over time (e.g. furrow

collapse, intercalation) The 0 value of r defines the center of the embryo. (B) θ represents the angular movement of cells (spreading). The 0 value of θ is determined experimentally as the position of the embryonic ventral midline. (C) L corresponds to the location of cells along the anterior-posterior axis (germband elongation). Each blue line represents the movement of one cell in time. (D–F) Statistical analysis of correlation of the velocity of mesoderm and ectoderm cells along the (D) radial, (E) angular, and (F) AP axes in a *htl* mutant, with correlation values of 0.24 ± 0.21 , 0.13 ± 0.12 , and 0.86 ± 0.06 , respectively. (G) Displacement of the mesoderm before (orange) and after (blue) subtraction of local ectoderm movement in a *htl* mutant.

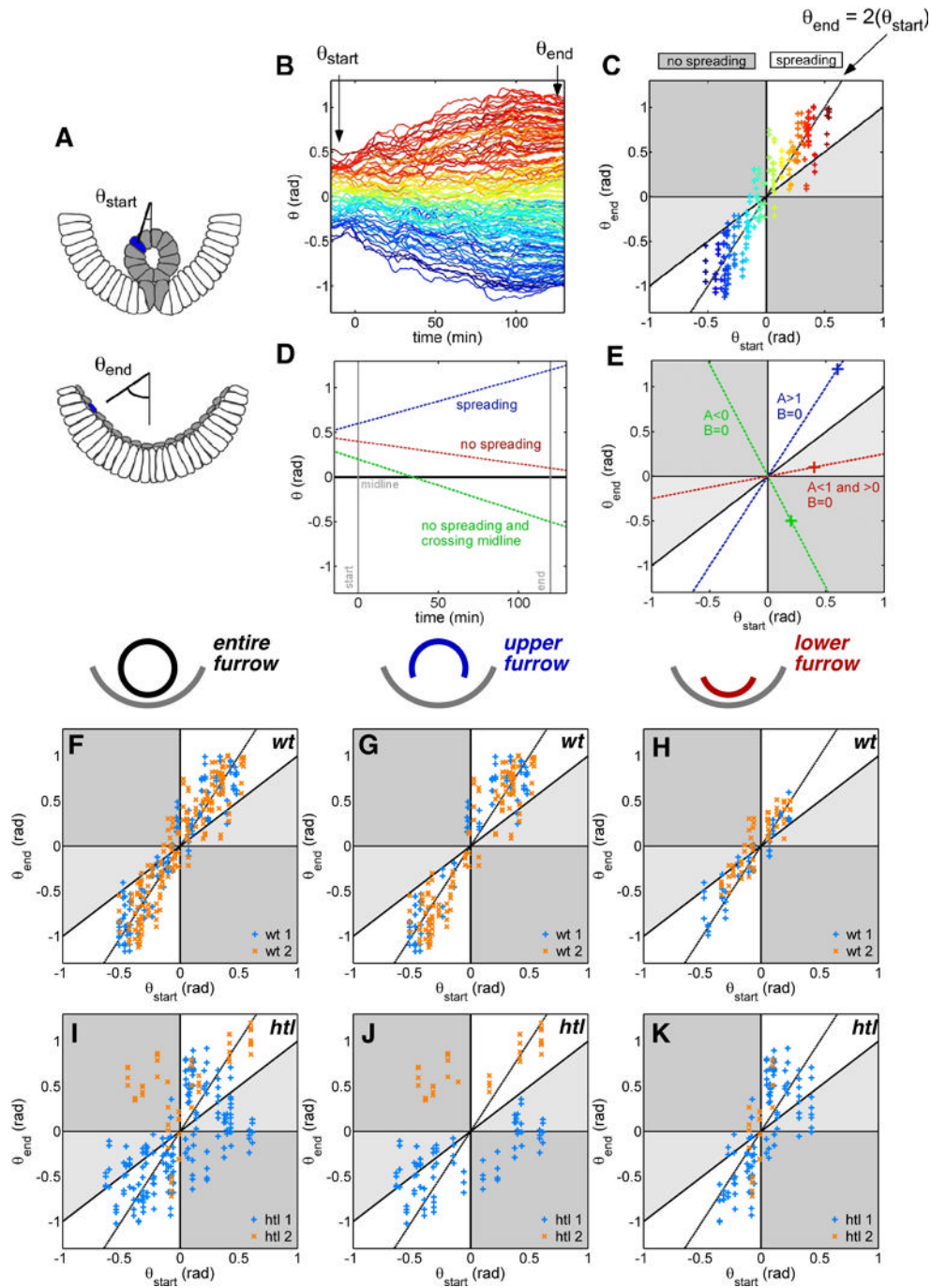


Figure S4. Spreading consistency analysis: $\theta_{start}(\theta_{end})$ graphs. (A–C) The mesoderm spreading is analyzed by obtaining the angular position of each cell at the onset and the

end of the process, θ_{start} and θ_{end} , respectively (A). The color code is similar to Figure 3A. The spatial organization observed in a $\theta(\text{time})$ graph (B, similar to Figure 3A) is translated into a 2D graph where the $\theta_{\text{end}}(\theta_{\text{start}})$ position of each cell is plotted (C). This graph is used to characterize the spreading by fitting a regression line [$\theta_{\text{end}} = (A \cdot \theta_{\text{start}}) + B$] on the experimental data. Data points that fall within the white region of the graph represent spreading cells, while points in grey regions represent cells that do not spread with the collective. The values of A and B are estimated using a least-squares method, and the correlation coefficient R of the fitting is displayed in the table of Figure S6 for different embryos. (D–E) $\theta(\text{time})$ graph (D) and $\theta_{\text{end}}(\theta_{\text{start}})$ graph (E) for three typical cell movements assuming $B=0$: normal spreading (blue color, $A>1$ and $B=0$ line in E), movement toward the midline (no spreading, red color, $A<1$ and >0 and $B=0$ line in E), and movement toward the opposite side of the embryo (no spreading and crossing the midline, green color, $A<0$ and $B=0$ line in E). (F–H) Wild-type embryo spreading profile within the entire mesoderm (F), upper furrow (G), and lower furrow (H). The orange or blue ticks represent datapoints for each of two embryos of either *wt* or *htl* backgrounds. (I–K) *htl* embryo spreading profile in the entire mesoderm (I), upper (J) and lower furrow (K). Cells in the lower furrow of *htl* embryos display wild-type behavior (compare to H); whereas cells in the upper furrow fall into two categories. Most spread abnormally (grey area), but some spread normally (white area).

A

Embryos	Cell population	A	$\pm \Delta A$	B	$\pm \Delta B$	R
wt 1	all (126)	1.85	0.12	0.03	0.04	0.94
wt 2	all (186)	1.93	0.12	0.01	0.03	0.92
wt 3	all (90)	2.36	0.26	-0.02	0.05	0.90
wt 4 (klar)	all (138)	1.98	0.14	0.05	0.04	0.92
wt 5 (klar)	all (56)	2.01	0.22	0.03	0.07	0.93
all wt embryos	all (596)	1.96	0.06	0.03	0.02	0.93
htl 1	all (185)	0.92	0.18	-0.11	0.06	0.61
htl 2	all (53)	0.69	0.33	0.48	0.12	0.51
htl 3	all (46)	1.34	0.29	-0.21	0.09	0.81
all htl embryos	all (284)	0.98	0.16	-0.02	0.05	0.58
wt 1	upper furrow (82)	1.90	0.15	0.04	0.05	0.94
wt 2	upper furrow (128)	1.99	0.13	-0.04	0.04	0.93
wt 3	upper furrow (36)	2.69	0.49	0.02	0.10	0.89
wt 4 (klar)	upper furrow (77)	2.08	0.17	0.10	0.06	0.94
wt 5 (klar)	upper furrow (36)	1.96	0.26	0.07	0.10	0.94
all wt embryos	upper furrow (359)	2.02	0.08	0.04	0.03	0.93
htl 1 (klar)	upper furrow (81)	0.54	0.13	-0.29	0.05	0.69
htl 2 (klar)	upper furrow (37)	0.51	0.13	0.69	0.06	0.79
htl 3	upper furrow (28)	1.16	0.23	-0.34	0.08	0.90
all htl embryos	upper furrow (146)	0.78	0.19	-0.05	0.08	0.55
wt 1	lower furrow (44)	1.63	0.20	-0.01	0.05	0.93
wt 2	lower furrow (58)	1.58	0.22	0.10	0.04	0.89
wt 3	lower furrow (54)	2.13	0.24	-0.05	0.05	0.93
wt 4 (klar)	lower furrow (61)	1.65	0.21	-0.01	0.05	0.89
wt 5 (klar)	lower furrow (23)	2.37	0.66	-0.03	0.10	0.90
all wt embryos	lower furrow (237)	1.74	0.11	0.01	0.02	0.90
htl 1 (klar)	lower furrow (104)	1.79	0.34	-0.01	0.07	0.71
htl 2 (klar)	lower furrow (16)	4.14	2.42	0.10	0.19	0.70
htl 3	lower furrow (18)	1.98	0.84	-0.07	0.16	0.78
all htl embryos	lower furrow (138)	1.83	0.31	-0.01	0.06	0.71
htl 1 (klar)	far from ectoderm (83)	0.45	0.17	-0.15	0.06	0.52
htl 2 (klar)	far from ectoderm (33)	0.43	0.36	0.54	0.12	0.40
htl 3	far from ectoderm (38)	1.09	0.34	-0.14	0.10	0.73
all htl embryos	far from ectoderm (154)	0.39	0.19	0.02	0.07	0.31
htl 1 (klar)	close to ectoderm (102)	1.90	0.27	0.06	0.07	0.81
htl 2 (klar)	close to ectoderm (20)	2.04	0.61	-0.02	0.23	0.86
htl 3	close to ectoderm (8)	1.85	0.75	-0.28	0.25	0.93
all htl embryos	close to ectoderm (130)	1.93	0.21	0.03	0.06	0.85

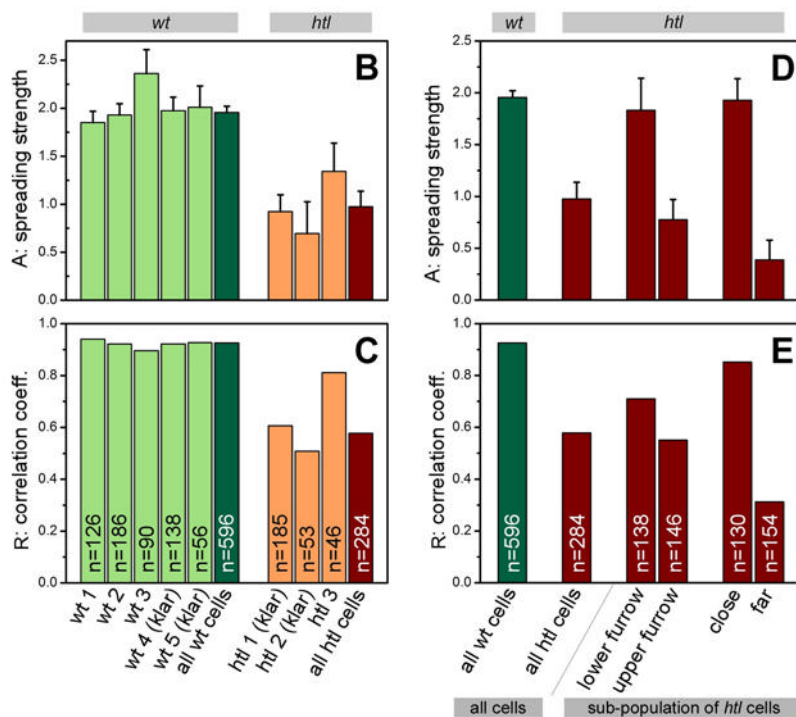


Figure S5. Spreading consistency analysis: table of linear regression and main conclusions. (A) The $\theta_{\text{end}}(\theta_{\text{start}})$ graphs (e.g., Figure S4C) are analyzed by fitting a

regression line ($\theta_{\text{end}} = A \cdot \theta_{\text{start}} + B$) on the experimental data. The estimated A and B values (with a 95% confidence interval), as well as the resulting correlation coefficient R are indicated in this table for different cell populations. The number of cells analyzed in each case is indicated between brackets. (C–E) “A” (C) and “R” (D) values of five *wt* embryos (including the data of two *klar*, which for all extent of purposes shares a similar phenotype with *wt*) versus three *htl* embryos are indicated in light green and light red, respectively. The same analysis performed by pooling the cells from all *wt* or *htl* embryos are plotted in dark green and dark red, respectively. (E and F) The analysis (A and R values) of two *htl* cell populations are performed using either the upper/lower furrow cutoff (middle of the graphs) or the close/far position from the ectoderm at the end of the process (right of the graphs). When segregated, the *htl* cells coming from the lower furrow exhibited movements that were collective (i.e., higher A and R values), similar to *wt* cells; in contrast, the *htl* cells from the upper furrow displayed less coordination (i.e. low values for A and R). **n** indicates the number of cells used for the analyses. See Methods section for full description of approach.

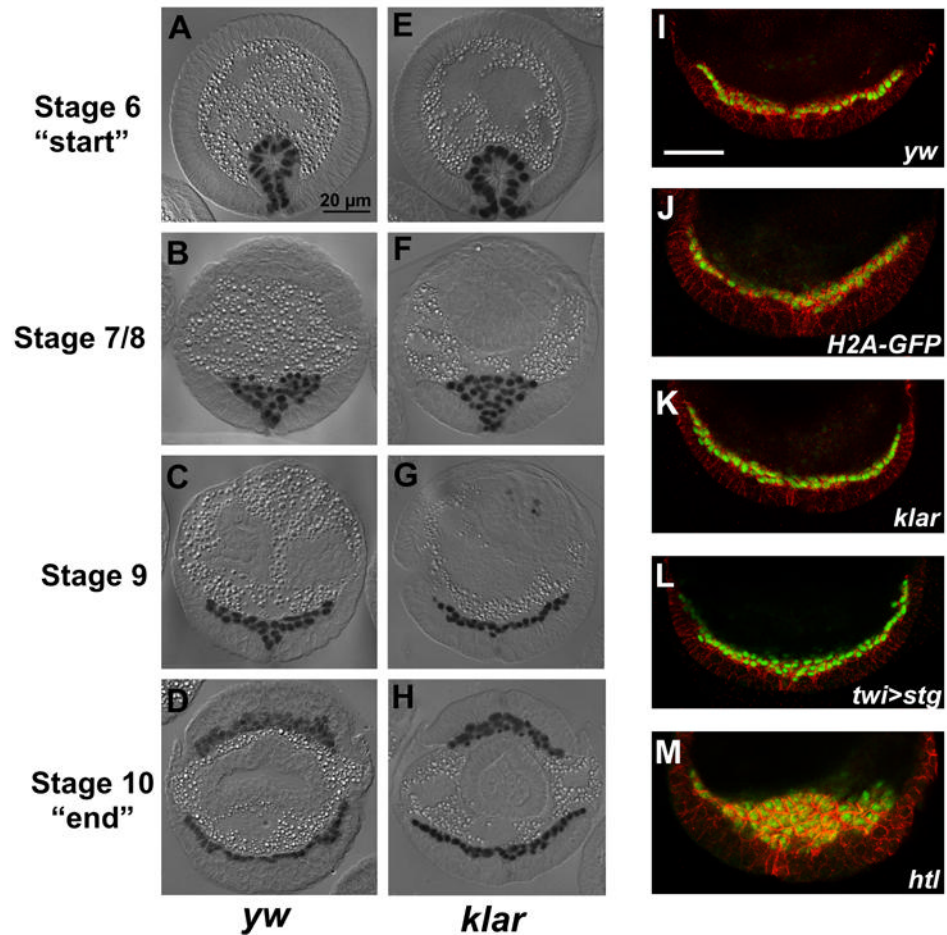


Figure S6. Wild-type and *klarschist* embryos show similar morphology in fixed sections. (A–D) *yw* (“wild-type”) and (E–H) *klar* (*klarschist*) embryos were stained with an anti-Twist antibody and sectioned. (A and E) Stage 6, (B and F) Stage 7/8, (C and G) Stage 9, and (D and H) Stage 10 sections are shown. (I–M) Fluorescent sections of embryos with anti-Twist (green) and anti-Neurotactin (red) antibodies show morphology of different genetic backgrounds. *yw* (I), ubiquitous H2A-GFP (J), *klarschist* (K), and embryos ectopically expressing string in the mesoderm (*twi*-Gal4 UAS-string) (L)

embryos all show wild-type mesoderm morphology (see “yw”). *htl*^{AB42} embryos (M) have a multi-layered mesoderm, indicative of defective mesoderm migration.

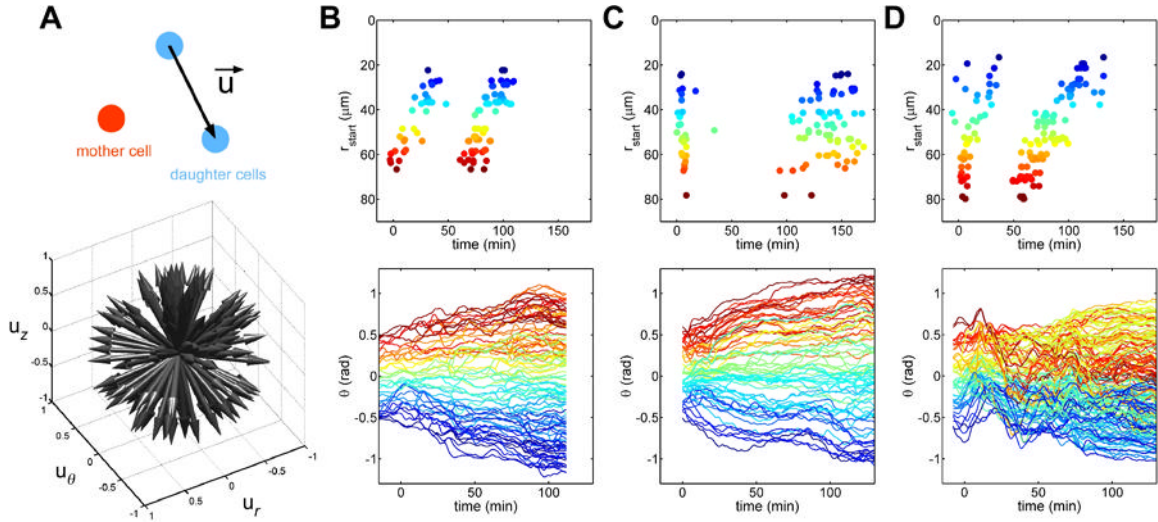
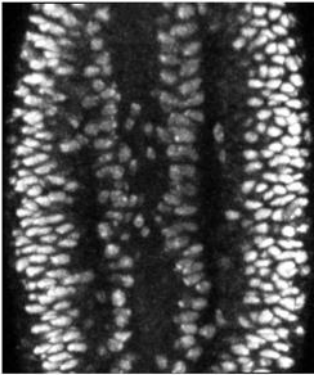
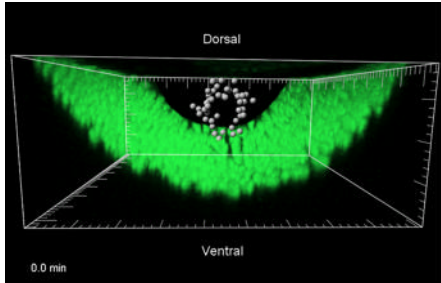


Figure S7. Disrupting the spatial or temporal patterns of division in the mesoderm does not affect the spreading pattern. (A) Cell division orientation in wild-type embryos is random (N=8 embryos). Each arrow shows the division orientation, \mathbf{u} , of the daughter cells for one particular mother cell, see diagram at the top for example. (B) Wild-type pattern of divisions and spreading correlate with radial position, as cells closer to the ectoderm divide first followed by cells farther away. See Figure 4 and Figure S5 for color code. (C) *klarschist* embryos with mild induced phototoxicity exhibit abnormal division patterns consistent with previous studies of phototoxicity. The spreading pattern is not affected by this disruption. (D) *htl* mutants display wild-type division patterns. The spreading pattern, however, is highly disrupted.

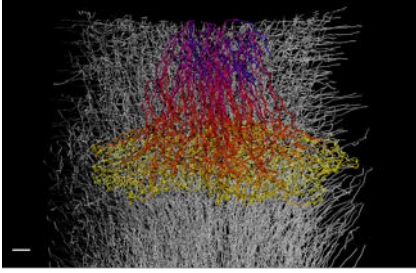
II. Movie Legends



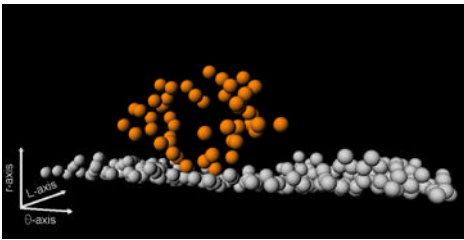
Movie 1. Two-photon excitation of ubiquitous H2A-GFP in early embryos. Images of a H2A-GFP expressing embryo taken from dorsal view (10 μm thick stack 50 μm deep into the embryo) or a posterior view (5 μm thick stack) using two-photon microscopy. Scale bar = 20 μm .



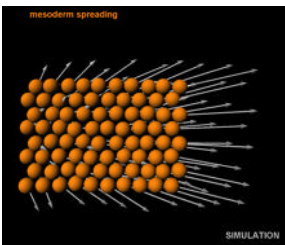
Movie 2. Segmentation and tracking of mesoderm nuclei in wild-type embryos using Imaris software. Spots represent mesoderm nuclei tracked over time (see Materials and Methods for more details). Ectoderm H2A-GFP raw data is kept in for reference. Tracks are represented by lines with a temporal color code, where purple represents early time points and yellow represents late time points (see scale bar in Figure 1). The first view is dorsal, and the second view is posterior. Large grid mark = 20 μm .



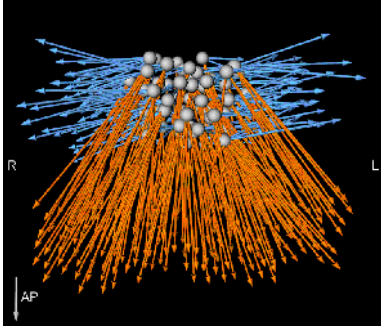
Movie 3. 3D tracks of mesoderm and ectoderm cells over time. A dorsal view of mesoderm tracks is first shown in with a temporal color scale (see Figure 1) on top of grey ectoderm tracks. Displacement vectors for mesoderm and ectoderm are represented by orange and grey arrows, respectively. Scale bar = 20 μm .



Movie 4. Visualization of cylindrical coordinate system. Data from each embryo can be unwrapped according to cylindrical coordinates (See Figure S1 and Materials & Methods for more details).

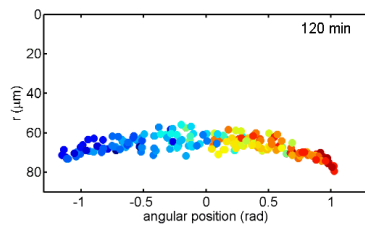


Movie 5. Ectoderm Subtraction in a wild-type embryo (simulation). The local movement of ectoderm cells is subtracted from the mesoderm to show autonomous movement of the mesoderm (see Materials & Methods for more details).



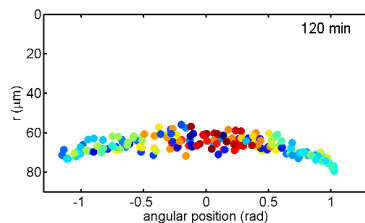
Movie 6. Ectoderm Subtraction in a wild-type embryo (experimental data).

Displacement of the mesoderm before (orange) and after (blue) subtraction of local ectoderm movement (3-D version of Figure 2I, see Materials & Methods for more details). A= Anterior, P=Posterior, L=Left, R=Right, D=Dorsal, V=Ventral.



Movie 7. Wild-type cell movements along radial and angular axes (theta color code).

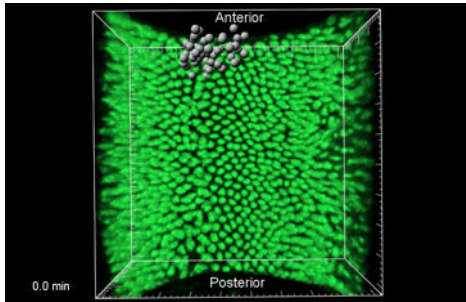
The position of each cell is represented with a dot. Its color encodes for the angular position at the onset of mesoderm collapse (stage 7). In addition, dots representing dividing cells are circled with a black line at the time of the division.



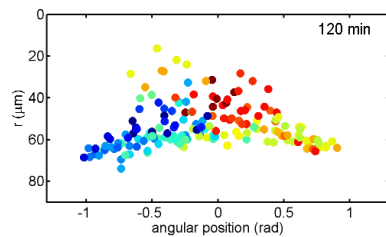
Movie 8. Wild-type cell movements along radial and angular axes (radial color code).

The position of each cell is represented with a dot. Its color encodes for the radial

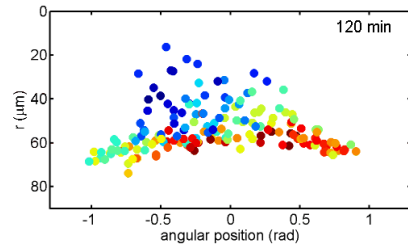
position at the onset of mesoderm collapse (stage 7). In addition, dots representing dividing cells are circled with a black line at the time of the division.



Movie 9. Segmentation and tracking of mesoderm nuclei in *htl* mutant. Mesoderm nuclei are represented by spots, with raw ectoderm H2A-GFP data underneath. Tracks have a temporal color code (see scale bar in Figure 1). The first view is dorsal, and the second view is posterior. Large grid mark = 20 μm .



Movie 10. *htl* cell movements along radial and angular axes (angular color code). The position of each cell is represented with a dot. Its color encodes for the angular position at the onset of mesoderm collapse (stage 7). The dots of dividing cells are circled with a black line.

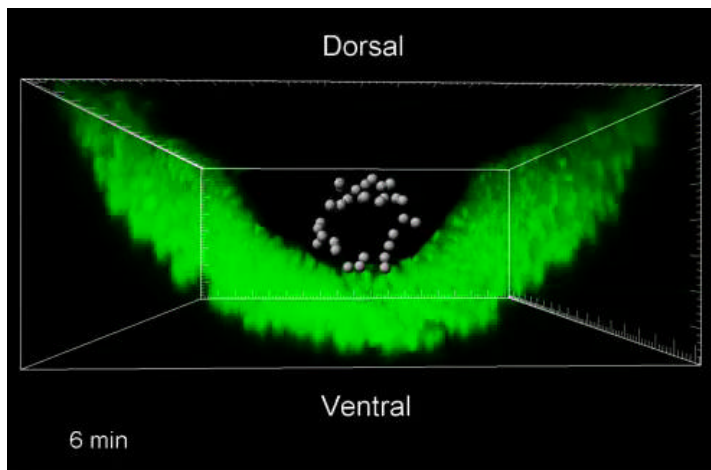


Movie 11. *htl* cell movements along radial and angular axes (radial color code). The position of each cell is represented with a dot. Its color encodes for the radial position at the onset of mesoderm collapse (stage 7). The dots of dividing cells are circled with a black line.

Appendix C: Supplementary Materials for Chapter 4

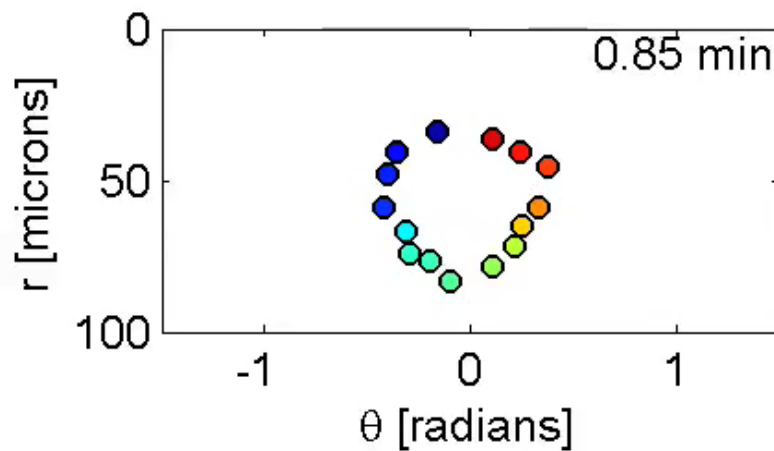
- I. Movie Captions
- II. Supplementary Figures

I. Movie Captions.



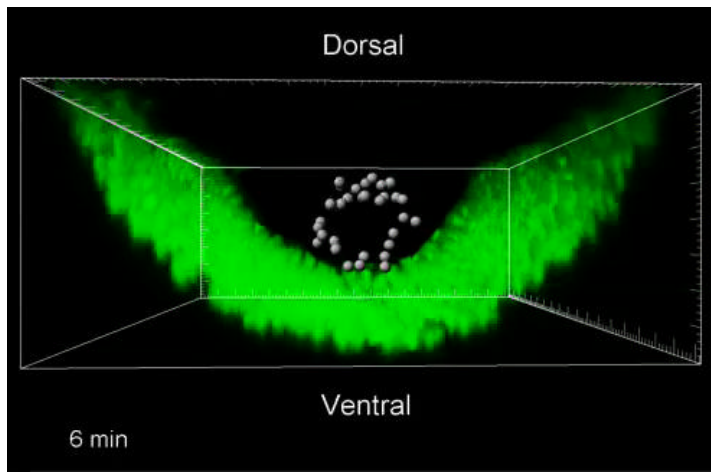
Movie 1. In vivo imaging of mesoderm spreading in different genetic backgrounds.

Images of H2A-GFP expressing embryos imaged using two-photon microscopy. Mesoderm nuclei were tracked (grey balls) over time using Imaris software (see Materials and Methods for details). Ectoderm raw data is shown for reference and is the substratum on which the mesoderm cells crawl. Large grid mark = 20 μm .



Movie 2. Mesoderm cell movements along the radial and angular axes over time in different genetic backgrounds. Mesoderm tracking data was exported from Imaris

into Matlab and decomposed into cylindrical coordinates (see Materials and Methods for details). Each cell is represented by a dot and is color-coded according to its initial angular position to make visualization easier. r , the radial axis, represents movement toward or away from the ectoderm (0 = center of the embryo, 90 = ectoderm). θ , the angular axis, represents movement along the dorsoventral axis (0 = midline).



Movie 3. In vivo imaging and analysis of *mys* mutant. Images of H2A-gfp expressing embryos injected with *mys* morpholino. Mesoderm nuclei were tracked (grey balls) over time using Imaris software (see Materials and Methods for details). Ectoderm raw data is shown for reference and is the substratum on which the mesoderm cells crawl. Large grid mark = 20 μm . This data is then exported into Matlab and decomposed into cylindrical coordinates. Each cell is represented by a color-coded dot according to its initial angular position. The radial axis, r , represents movement toward or away from the ectoderm (0 = center of the embryo, 90 = ectoderm). The angular axis, θ , represents movement along the dorsoventral axis (0 = midline).

II. Supplementary Figures

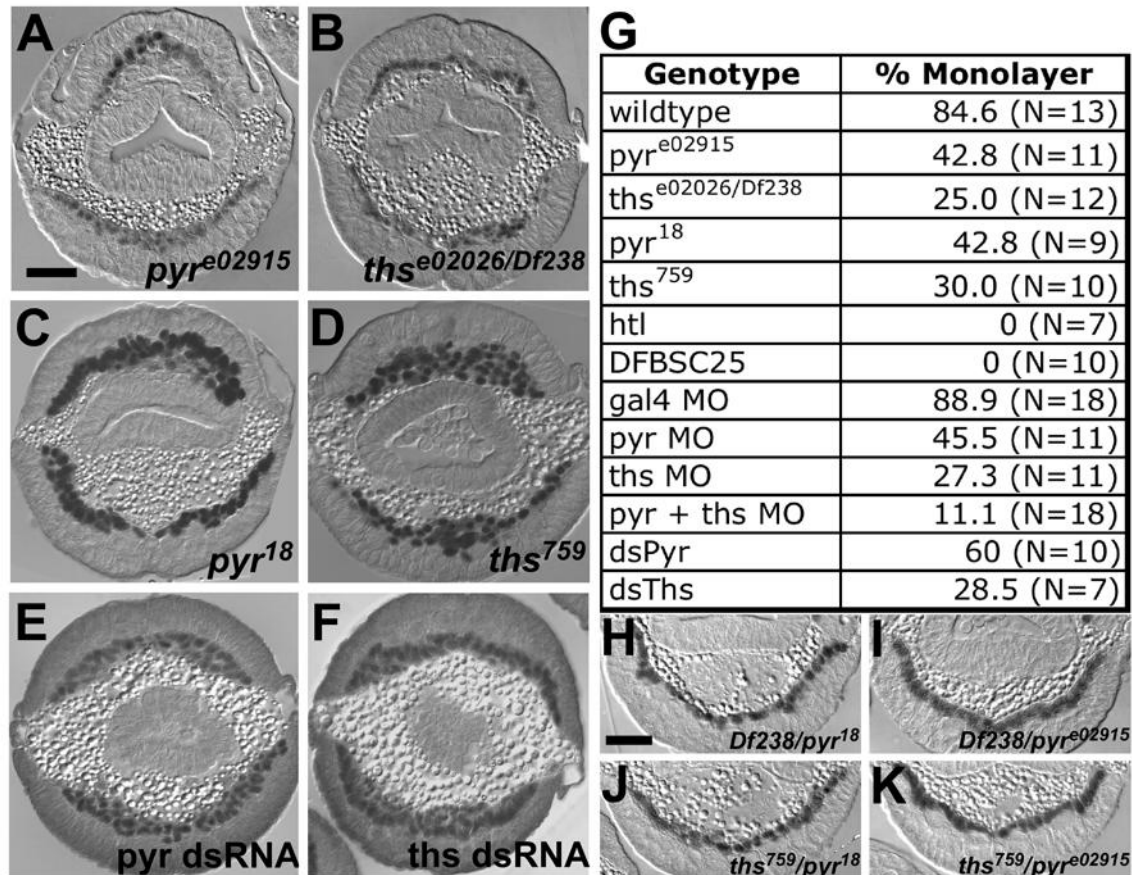


Figure S1. Pyr and Ths exhibit a non-monolayer phenotype. (A-F, H-K) Stage 10 embryos cross-sectioned and stained with twist antibody (black). (A,B) *pyr* and *ths* lines from (Kadam, Snehalata et al., 2009). (C,D) *pyr* and *ths* lines obtained from (Klingseisen, Anna et al., 2009). (E,F) Double stranded RNA designed against Pyr and Ths transcripts was injected into pre-cellularized embryos and allowed to age to stage 10. (G) Percent of embryos with a consistent monolayer (>90% of the embryo length) in different mutant backgrounds. (H-K) The two *pyr* alleles were placed of the two *ths* alleles. Rescue was seen in all embryos, except in embryos containing the *ths*⁷⁵⁹ allele,

which had a slight non-monolayer phenotype (~20% of embryos, N=9). Scale bar = 20 μm .

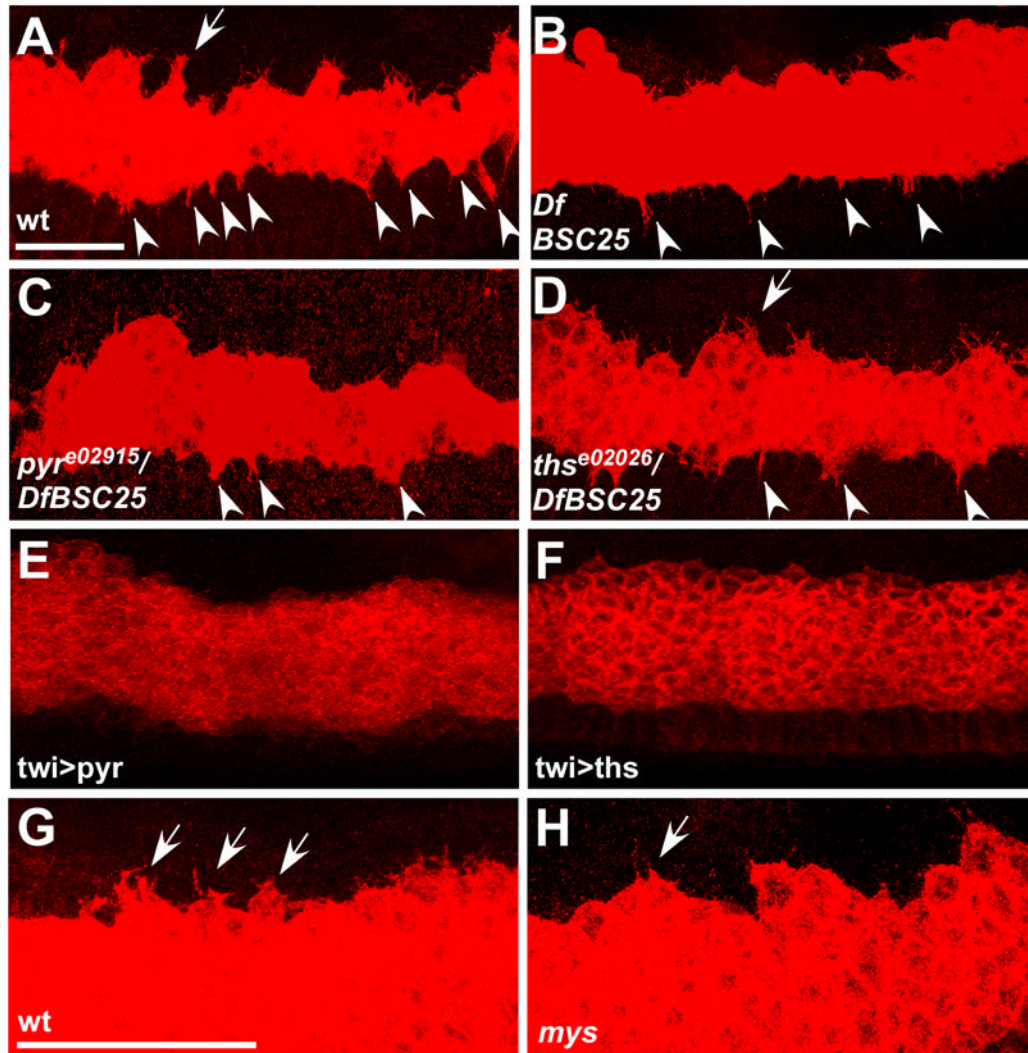


Figure S2. Protrusions into the ectoderm are reduced in FGF mutants. (A-I) Stage 9 embryos stained with CD2 antibody to mark mesoderm membranes (red). (A) Wild-type embryos send out protrusions at the leading edge (arrow) and into the ectoderm (arrowheads). (B) *pyr* and *ths* double mutants and (C) *pyr* single mutants have fewer protrusions at the leading edge and in the ectoderm (arrowheads). (D) *ths* mutants have fewer protrusions into the ectoderm (arrowheads), but a normal number of protrusions at

the leading edge (arrow). **(E)** Protrusions are completely suppressed in embryos expressing *Pyr* in the mesoderm using *twi-gal4*. **(F)** Protrusive activity is moderately inhibited in embryos expressing *Ths* in the mesoderm using *twi-gal4*. **(G)** By examining the leading edge at higher magnification, it is apparent that wild-type embryos have several hair-like protrusions at the leading edge. **(H)** *mys* mutants have a severe reduction in the number of hair like protrusions. Scale bar = 20 μm .

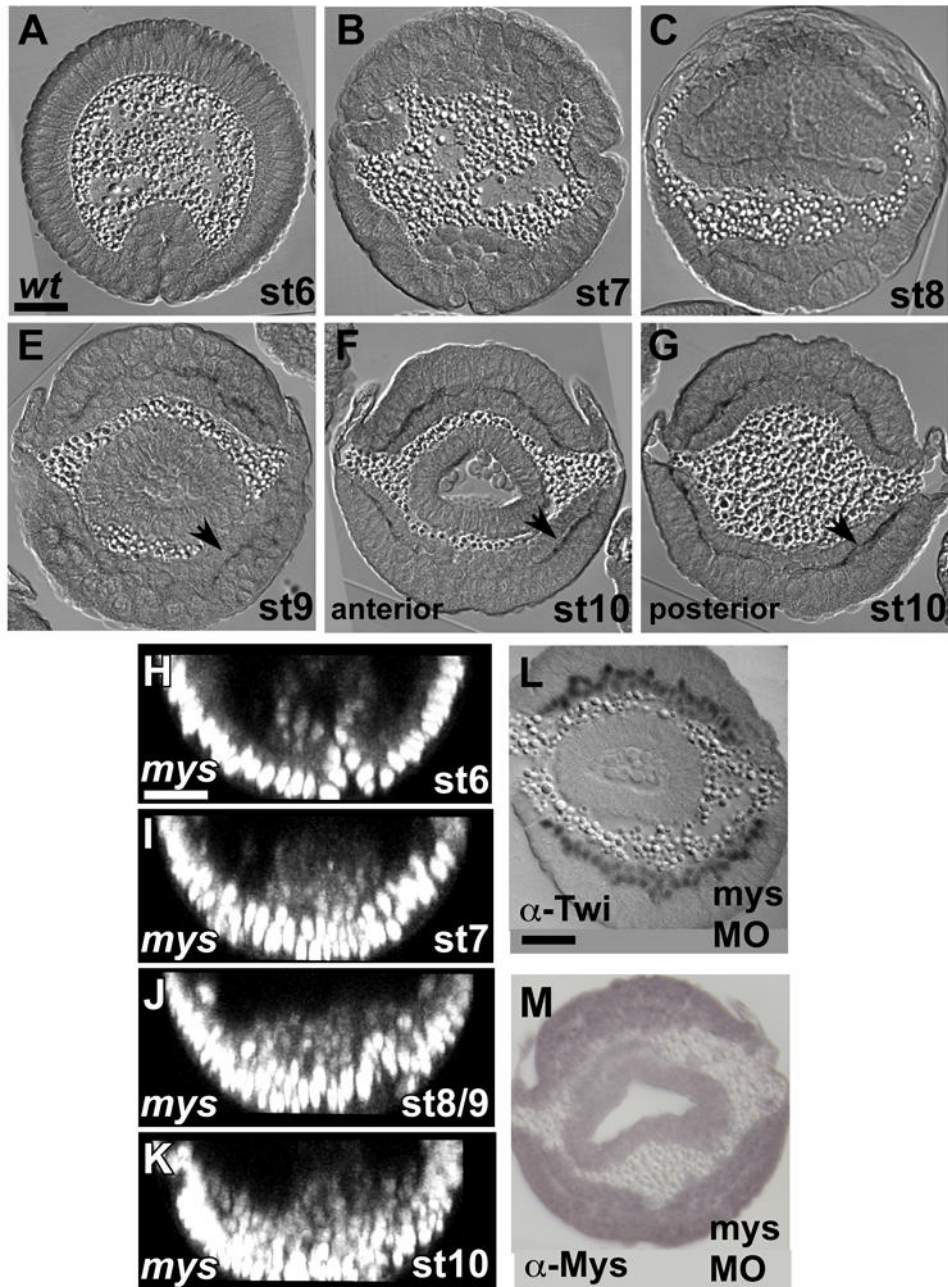


Figure S3. Mys is localized to the interface of the mesoderm and ectoderm at stage 9 and 10. (A-G) Wild-type embryos cross-sectioned and stained with Mys antibody (black). (A-C) Mys protein is not observed at (A) stage 6, (B) stage 7, or (C) stage 8. (E) At stage 9, Mys begins to localize between the ectoderm and mesoderm (arrowhead). (F,G) Mys is localized at the interface between the ectoderm and mesoderm during stage

10 throughout the embryo. **(H-K)** Virtual cross sections through *mys* mutants during live imaging at (H) stage 6, (I) stage 7, (J) stage 8/9, (K) and stage 10. **(L)** Cross section of stage 10 embryo stained with Twist antibody (black). Mys morpholino (MO) was injected at a concentration of 2 mM, which resulted in a non-monolayer. **(M)** Cross section of stage 10 embryo stained with Mys antibody. The Mys MO was able to reduce the level of Mys protein, such that it was not detectable by immunostaining. Scale bar = 20 μm .

Appendix D: Data for the GTPase Ras1

FGF and other receptor tyrosine kinase (RTK) signaling pathways have the potential to act through several downstream effectors that perform different functions during development (Thisse and Thisse, 2005). The two downstream pathways of relevance in mesoderm migration are through the effectors Ras and Rap1, two similar small GTPases. Ras activation downstream of RTK signaling is associated with cell differentiation, polarity, and migration, while Rap1 activates components that are involved in cell migration and adhesion (Bos, 2005; Charest and Firtel, 2007).

During mesoderm development in *Drosophila*, FGF signaling through Ras is required for differentiation of heart cell precursors called Eve cells (Carmena et al., 1998). The downstream components that control FGF dependent migration in the mesoderm have not been discovered. It has been hypothesized that Pyramus and Thisbe may be able to differentially activate Heartless, such that one ligand activates Ras dependent signaling, while the other activates migratory components like Rap1. In glial cell migration, for instance, it has been shown that Rap1 appears to be required for migration, while Map kinase (ERK) activation, which is often downstream of Ras activity, appears to be important for subsequent differentiation (Franzdottir et al., 2009). Within these tissues, Pyramus and Thisbe are expressed in distinct, non-overlapping domains, which could explain why each ligand appears dedicated to the activation of either ERK or Rap1. It remains unclear, however, whether this association is a general rule, with Pyramus and Thisbe acting through different downstream pathways, or whether it is a condition of the expression domains of Pyramus and Thisbe during glial cell development.

During mesoderm migration, *Pyramus* and *Thisbe* are expressed in non-overlapping domains, so we also sought to understand what downstream effectors of FGF signaling are important for mesoderm migration and whether each ligand is responsible for a different downstream pathway.

We discovered that *Rap1* mutants share the same migration defects as *htl* mutants (Figure 1A-C). *Ras1* mutants have a less severe phenotype, with a collapse defect similar to *htl* mutants, but a non-monolayer defect only occasionally (Figure 1D). Therefore, *Ras1* may also play a part in mesoderm migration, although the phenotype did not resemble that of *htl* mutants at stage 10. Diphosphorylated ERK (dpERK), a readout for FGF signaling, seems to be influenced by both *Ras1* and *Rap1*, but in different ways; *Ras1* is required for dpERK to be activated to any extent, while *Rap1* may be required to restrict dpERK to the leading edge (Figure 2A-I). Whether dpERK is important for mesoderm migration has yet to be determined. These data support the idea that multiple GTPases are involved in mesoderm migration.

We found that *Heartless* acts through *Ras1* and not *Rap1* to control heart cell differentiation following mesoderm migration (Figure 3A-F). *Ras1* mutants, as well as *htl* mutants, are unable to specify *Eve* cells (Figure 3B,D). *Rap1* mutants have a subtle defect in *Eve* cell number, but this may be a result of the earlier migration defect (Figure 3F). Activated *Ras1* is able to cause *Eve* cell proliferation, similar to activated *Heartless* (Figure 3C, data not shown). Activated *Rap1* does not affect *Eve* specification (Figure 3E). These data suggest that *Rap1* is not involved in *Eve* cell specification.

Unlike glial cell migration, both ligands seem to be involved in supporting mesoderm migration as well as differentiation of heart cell precursors, which implies that

both Pyramus and Thisbe can activate either downstream pathway, if they are indeed separate. Together these results suggest that both Pyramus and Thisbe may signal through Heartless, Ras1 and Rap1 to control collective mesoderm migration and through Heartless and Ras1 during heart cell specification.

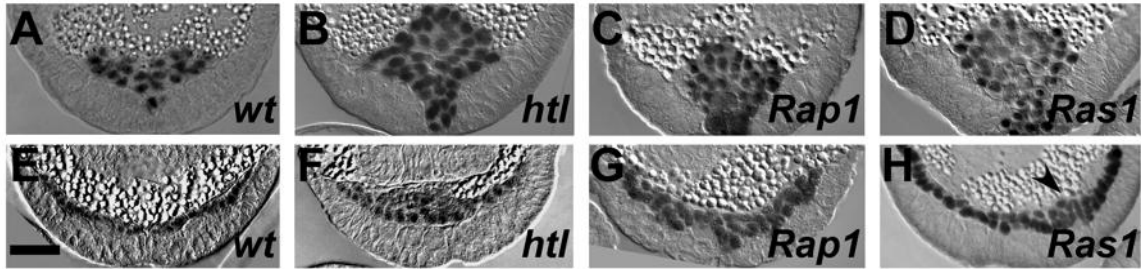


Figure 1. Rap1 and Ras1 both have defects during mesoderm migration. (A-D) Stage 7 embryos stained with anti-Twist antibody. (A) The mesoderm tube collapses onto the ectoderm in wild-type embryos. (B-D) In *htl*, *Rap1*, and *Ras1* mutants, the tube fails to collapse. (E-H) Stage 10 embryos stained with anti-Twist antibody. (E) In wild-type embryos the mesoderm forms a monolayer. (F,G) In *htl* and *Rap1* mutants, the mesoderm consistently fails to form a monolayer. (H) *Ras1* mutants have a variable phenotype with a monolayer formed in some embryos (not shown) and a mild non-monolayer formed in others (arrowhead).

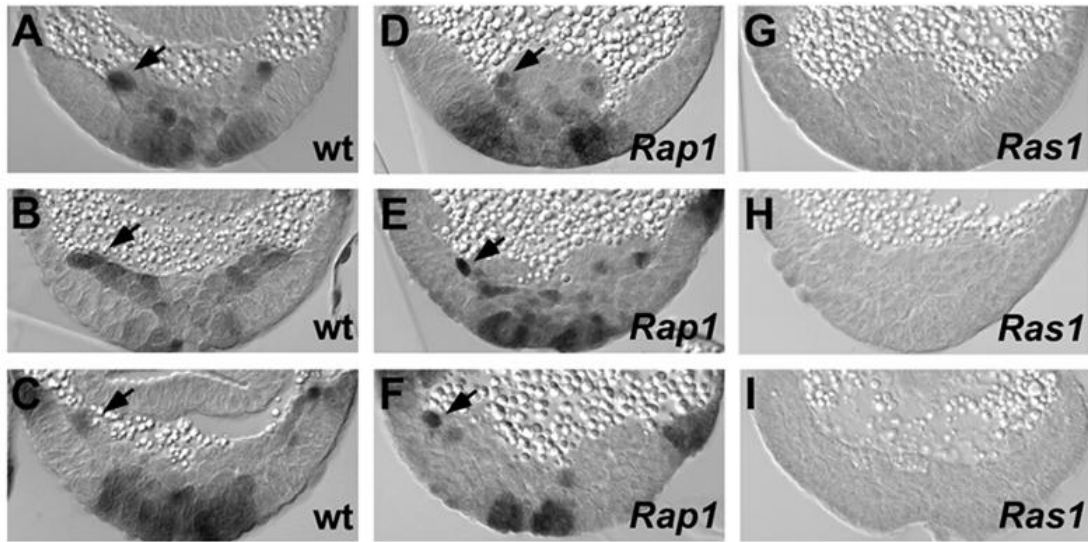


Figure 2. Regulation of ERK in the mesoderm is dependent on Ras1 and Rap1. (A-I) Embryos stained with anti-dpERK antibody. (A,D,G) Stage 7 embryos. (B,E,H) Stage 9 embryos. (C,F,I) Stage 10 embryos. (A-C) Wild-type embryos have dpERK activated at the leading edge throughout migration. (D-F) *Rap1* mutants have dpERK at the leading edge (arrow), but also ectopically within the rest of the mesoderm. (G-I) *Ras1* mutants are unable to activate dpERK during mesoderm migration.

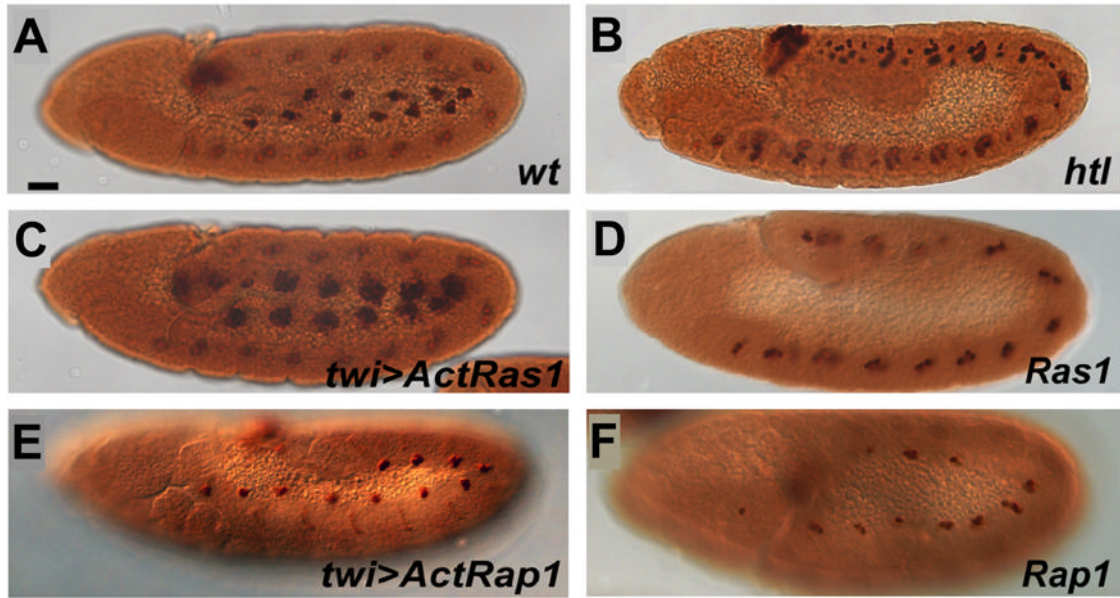


Figure 3. Htl and Ras1 are required for Eve cell specification. (A-F) Stage 11 embryos stained with anti-Eve antibody. (A) In wild-type embryos Eve-positive cells are specified at stage 11 and form a cluster of 3 in every hemisegment. (B) In *htl* mutants, Eve positive cells are not specified. (C) Expression of activated Ras1 in the mesoderm causes the number of Eve cells per cluster to increase. (D) *Ras1* mutants do not specify Eve cells. (E) Expression of activated Rap1 in the mesoderm does not affect Eve cell specification. (F) In *Rap1* mutants, Eve cells are specified. A few cells are missing, which may be an indirect result of a spreading defect.

Bibliography

Akiyama-Oda, Y., Hotta, Y., Tsukita, S. and Oda, H. (2000). Distinct mechanisms triggering glial differentiation in *Drosophila* thoracic and abdominal neuroblasts 6-4. *Dev Biol* **222**, 429-439.

Anant, S., Roy, S. and VijayRaghavan, K. (1998). Twist and Notch negatively regulate adult muscle differentiation in *Drosophila*. *Development* **125**, 1361-1369.

Aracena, J., Gonzalez, M., Zuniga, A., Mendez, M. A. and Cambiazo, V. (2006). Regulatory network for cell shape changes during *Drosophila* ventral furrow formation. *J Theor Biol* **239**, 49-62.

Asha, H., de Ruiter, N. D., Wang, M. G. and Hariharan, I. K. (1999). The Rap1 GTPase functions as a regulator of morphogenesis in vivo. *EMBO J* **18**, 605-615.

Baylies, M. K. and Bate, M. (1996). twist: a myogenic switch in *Drosophila*. *Science* **272**, 1481-1484.

Beaurepaire, E. and Mertz, J. (2002). Epifluorescence collection in two-photon microscopy. *Appl Opt* **41**, 5376-5382.

Beccari, S., Teixeira, L. and Rorth, P. (2002). The JAK/STAT pathway is required for border cell migration during *Drosophila* oogenesis. *Mech Dev* **111**, 115-123.

Beiman, M., Shilo, B. Z. and Volk, T. (1996). Heartless, a *Drosophila* FGF receptor homolog, is essential for cell migration and establishment of several mesodermal lineages. *Genes Dev* **10**, 2993-3002.

Bertet, C., Sulak, L. and Lecuit, T. (2004). Myosin-dependent junction remodelling controls planar cell intercalation and axis elongation. *Nature* **429**, 667-671.

- Bianco, A., Poukkula, M., Cliffe, A., Mathieu, J., Luque, C. M., Fulga, T. A. and Rorth, P.** (2007). Two distinct modes of guidance signalling during collective migration of border cells. *Nature* **448**, 362-365.
- Boettner, B. and Van Aelst, L.** (2009). Control of cell adhesion dynamics by Rap1 signaling. *Curr Opin Cell Biol* **21**, 684-693.
- Bos, J. L.** (2005). Linking Rap to cell adhesion. *Curr Opin Cell Biol* **17**, 123-128.
- Brown, N. H.** (2000). Cell-cell adhesion via the ECM: integrin genetics in fly and worm. *Matrix Biol* **19**, 191-201.
- Butler, L. C., Blanchard, G. B., Kabla, A. J., Lawrence, N. J., Welchman, D. P., Mahadevan, L., Adams, R. J. and Sanson, B.** (2009). Cell shape changes indicate a role for extrinsic tensile forces in *Drosophila* germ-band extension. *Nat Cell Biol* **11**, 859-864.
- Carmona, G., Gottig, S., Orlandi, A., Scheele, J., Bauerle, T., Jugold, M., Kiessling, F., Henschler, R., Zeiher, A. M., Dimmeler, S. et al.** (2009). Role of the small GTPase Rap1 for integrin activity regulation in endothelial cells and angiogenesis. *Blood* **113**, 488-497.
- Chou, T. B. and Perrimon, N.** (1996). The autosomal FLP-DFS technique for generating germline mosaics in *Drosophila melanogaster*. *Genetics* **144**, 1673-1679.
- Chuai, M., Dormann, D. and Weijer, C. J.** (2009). Imaging cell signalling and movement in development. *Semin Cell Dev Biol* **20**, 947-955.
- Clarkson, M. and Saint, R.** (1999). A His2AvDGFP fusion gene complements a lethal His2AvD mutant allele and provides an in vivo marker for *Drosophila* chromosome behavior. *DNA Cell Biol* **18**, 457-462.

- Debarre, D., Supatto, W., Farge, E., Moulia, B., Schanne-Klein, M. C. and Beaufrepaire, E.** (2004). Velocimetric third-harmonic generation microscopy: micrometer-scale quantification of morphogenetic movements in unstained embryos. *Opt Lett* **29**, 2881-2883.
- Debarre, D., Supatto, W., Pena, A. M., Fabre, A., Tordjmann, T., Combettes, L., Schanne-Klein, M. C. and Beaufrepaire, E.** (2006). Imaging lipid bodies in cells and tissues using third-harmonic generation microscopy. *Nat Methods* **3**, 47-53.
- Deisboeck, T. S. and Couzin, I. D.** (2009). Collective behavior in cancer cell populations. *Bioessays* **31**, 190-197.
- Delon, I. and Brown, N. H.** (2007). Integrins and the actin cytoskeleton. *Curr Opin Cell Biol* **19**, 43-50.
- Devreotes, P. and Janetopoulos, C.** (2003). Eukaryotic chemotaxis: distinctions between directional sensing and polarization. *J Biol Chem* **278**, 20445-20448.
- Devreotes, P. N. and Zigmond, S. H.** (1988). Chemotaxis in eukaryotic cells: a focus on leukocytes and Dictyostelium. *Annu Rev Cell Biol* **4**, 649-686.
- Dossenbach, C., Rock, S. and Affolter, M.** (2001). Specificity of FGF signaling in cell migration in Drosophila. *Development* **128**, 4563-4572.
- Duchek, P. and Rorth, P.** (2001). Guidance of cell migration by EGF receptor signaling during Drosophila oogenesis. *Science* **291**, 131-133.
- Duchek, P., Somogyi, K., Jekely, G., Beccari, S. and Rorth, P.** (2001). Guidance of cell migration by the Drosophila PDGF/VEGF receptor. *Cell* **107**, 17-26.
- Dunin-Borkowski, O. M. and Brown, N. H.** (1995). Mammalian CD2 is an effective heterologous marker of the cell surface in Drosophila. *Dev Biol* **168**, 689-693.

- Etienne-Manneville, S. and Hall, A.** (2001). Integrin-mediated activation of Cdc42 controls cell polarity in migrating astrocytes through PKCzeta. *Cell* **106**, 489-498.
- Etienne-Manneville, S. and Hall, A.** (2002). Rho GTPases in cell biology. *Nature* **420**, 629-635.
- Forman-Kay, J. D. and Pawson, T.** (1999). Diversity in protein recognition by PTB domains. *Curr Opin Struct Biol* **9**, 690-695.
- Franzdottir, S. R., Engelen, D., Yuva-Aydemir, Y., Schmidt, I., Aho, A. and Klambt, C.** (2009). Switch in FGF signalling initiates glial differentiation in the Drosophila eye. *Nature* **460**, 758-761.
- Frasch, M.** (1995). Induction of visceral and cardiac mesoderm by ectodermal Dpp in the early Drosophila embryo. *Nature* **374**, 464-467.
- Friedl, P. and Wolf, K.** (2003). Tumour-cell invasion and migration: diversity and escape mechanisms. *Nat Rev Cancer* **3**, 362-374.
- Friedl, P. and Gilmour, D.** (2009). Collective cell migration in morphogenesis, regeneration and cancer. *Nat Rev Mol Cell Biol* **10**, 445-457.
- Fuss, B., Josten, F., Feix, M. and Hoch, M.** (2004). Cell movements controlled by the Notch signalling cascade during foregut development in Drosophila. *Development* **131**, 1587-1595.
- Gabay, L., Seger, R. and Shilo, B. Z.** (1997). MAP kinase in situ activation atlas during Drosophila embryogenesis. *Development* **124**, 3535-3541.
- Ghabrial, A., Luschnig, S., Metzstein, M. M. and Krasnow, M. A.** (2003). Branching morphogenesis of the Drosophila tracheal system. *Annu Rev Cell Dev Biol* **19**, 623-647.

- Ghabrial, A. S. and Krasnow, M. A.** (2006). Social interactions among epithelial cells during tracheal branching morphogenesis. *Nature* **441**, 746-749.
- Gisselbrecht, S., Skeath, J. B., Doe, C. Q. and Michelson, A. M.** (1996). heartless encodes a fibroblast growth factor receptor (DFR1/DFGF-R2) involved in the directional migration of early mesodermal cells in the *Drosophila* embryo. *Genes Dev* **10**, 3003-3017.
- Gotwals, P. J., Paine-Saunders, S. E., Stark, K. A. and Hynes, R. O.** (1994). *Drosophila* integrins and their ligands. *Curr Opin Cell Biol* **6**, 734-739.
- Greenspan, R. J.** (2004). Fly pushing: the theory and practice of *Drosophila* genetics. Cold Spring Harbor, NY: Cold Spring Harbor Press.
- Grosshans, J. and Wieschaus, E.** (2000). A genetic link between morphogenesis and cell division during formation of the ventral furrow in *Drosophila*. *Cell* **101**, 523-531.
- Gryzik, T. and Muller, H. A.** (2004). FGF8-like1 and FGF8-like2 encode putative ligands of the FGF receptor Htl and are required for mesoderm migration in the *Drosophila* gastrula. *Curr Biol* **14**, 659-667.
- Guan, J. L.** (2005). Cell migration: developmental methods and protocols. Totowa, NJ: Humana Press.
- Hartenstein, V.** (1993). The Development of *Drosophila melanogaster*. New York: Cold Spring Harbor Laboratory Press.
- Hegerfeldt, Y., Tusch, M., Brocker, E. B. and Friedl, P.** (2002). Collective cell movement in primary melanoma explants: plasticity of cell-cell interaction, beta1-integrin function, and migration strategies. *Cancer Res* **62**, 2125-2130.

- Helmchen, F. and Denk, W.** (2005). Deep tissue two-photon microscopy. *Nat Methods* **2**, 932-940.
- Hopt, A. and Neher, E.** (2001). Highly nonlinear photodamage in two-photon fluorescence microscopy. *Biophys J* **80**, 2029-2036.
- Huang, P. and Stern, M. J.** (2005). FGF signaling in flies and worms: more and more relevant to vertebrate biology. *Cytokine Growth Factor Rev* **16**, 151-158.
- Huelsmann, S., Hepper, C., Marchese, D., Knoll, C. and Reuter, R.** (2006). The PDZ-GEF dizzy regulates cell shape of migrating macrophages via Rap1 and integrins in the *Drosophila* embryo. *Development* **133**, 2915-2924.
- Ilna, O. and Friedl, P.** (2009). Mechanisms of collective cell migration at a glance. *J Cell Sci* **122**, 3203-3208.
- Irvine, K. D. and Wieschaus, E.** (1994). Cell intercalation during *Drosophila* germband extension and its regulation by pair-rule segmentation genes. *Development* **120**, 827-841.
- Jang, A. C., Starz-Gaiano, M. and Montell, D. J.** (2007). Modeling migration and metastasis in *Drosophila*. *J Mammary Gland Biol Neoplasia* **12**, 103-114.
- Jeon, T. J., Lee, D. J., Lee, S., Weeks, G. and Firtel, R. A.** (2007). Regulation of Rap1 activity by RapGAP1 controls cell adhesion at the front of chemotaxing cells. *J Cell Biol* **179**, 833-843.
- Ji, N., Magee, J. C. and Betzig, E.** (2008). High-speed, low-photodamage nonlinear imaging using passive pulse splitters. *Nat Methods* **5**, 197-202.
- Kadam, S., McMahon, A., Tzou, P. and Stathopoulos, A.** (2009). FGF ligands in *Drosophila* have distinct activities required to support cell migration and differentiation. *Development* **136**, 739-747.

- Kadam, S., McMahon, A., Tzou, P. and Stathopoulos, A.** (2009). FGF ligands in *Drosophila* have distinct activities required to support cell migration and differentiation. In *Development*, vol. 136, pp. 739-747.
- Kam, Z., Minden, J. S., Agard, D. A., Sedat, J. W. and Leptin, M.** (1991). *Drosophila* gastrulation: analysis of cell shape changes in living embryos by three-dimensional fluorescence microscopy. *Development* **112**, 365-370.
- Keller, P. J., Schmidt, A. D., Wittbrodt, J. and Stelzer, E. H.** (2008). Reconstruction of zebrafish early embryonic development by scanned light sheet microscopy. *Science* **322**, 1065-1069.
- Keller, R.** (2006). Mechanisms of elongation in embryogenesis. *Development* **133**, 2291-2302.
- King, J. S. and Insall, R. H.** (2009). Chemotaxis: finding the way forward with *Dictyostelium*. *Trends Cell Biol* **19**, 523-530.
- Klingseisen, A., Clark, I. B. N., Gryzik, T. and Müller, H.-A. J.** (2009). Differential and overlapping functions of two closely related *Drosophila* FGF8-like growth factors in mesoderm development. In *Development*, vol. 136, pp. 2393-2402.
- Klingseisen, A., Clark, I. B., Gryzik, T. and Muller, H. A.** (2009). Differential and overlapping functions of two closely related *Drosophila* FGF8-like growth factors in mesoderm development. *Development* **136**, 2393-2402.
- Knox, A. L. and Brown, N. H.** (2002). Rap1 GTPase regulation of adherens junction positioning and cell adhesion. *Science* **295**, 1285-1288.
- Kooistra, M. R., Dube, N. and Bos, J. L.** (2007). Rap1: a key regulator in cell-cell junction formation. *J Cell Sci* **120**, 17-22.

- Kosman, D., Mizutani, C. M., Lemons, D., Cox, W. G., McGinnis, W. and Bier, E.** (2004). Multiplex detection of RNA expression in *Drosophila* embryos. *Science* **305**, 846.
- Krieg, M., Arboleda-Estudillo, Y., Puech, P. H., Kafer, J., Graner, F., Muller, D. J. and Heisenberg, C. P.** (2008). Tensile forces govern germ-layer organization in zebrafish. *Nat Cell Biol* **10**, 429-436.
- Lauffenburger, D. A. and Horwitz, A. F.** (1996). Cell migration: a physically integrated molecular process. *Cell* **84**, 359-369.
- Lecaudey, V. and Gilmour, D.** (2006). Organizing moving groups during morphogenesis. *Curr Opin Cell Biol* **18**, 102-107.
- Lecaudey, V., Cakan-Akdogan, G., Norton, W. H. and Gilmour, D.** (2008). Dynamic Fgf signaling couples morphogenesis and migration in the zebrafish lateral line primordium. *Development* **135**, 2695-2705.
- Lehmann, R. and Tautz, D.** (1994). In situ hybridization to RNA. *Methods Cell Biol* **44**, 575-598.
- Leptin, M.** (2005). Gastrulation movements: the logic and the nuts and bolts. *Dev Cell* **8**, 305-320.
- Leptin, M. and Grunewald, B.** (1990). Cell shape changes during gastrulation in *Drosophila*. *Development* **110**, 73-84.
- Leptin, M., Bogaert, T., Lehmann, R. and Wilcox, M.** (1989). The function of PS integrins during *Drosophila* embryogenesis. *Cell* **56**, 401-408.
- Liebling, M., Forouhar, A. S., Gharib, M., Fraser, S. E. and Dickinson, M. E.** (2005). Four-dimensional cardiac imaging in living embryos via postacquisition synchronization of nongated slice sequences. *J Biomed Opt* **10**, 054001.

- Mann, S. K., Brown, J. M., Briscoe, C., Parent, C., Pitt, G., Devreotes, P. N. and Firtel, R. A.** (1997). Role of cAMP-dependent protein kinase in controlling aggregation and postaggregative development in *Dictyostelium*. *Dev Biol* **183**, 208-221.
- Martin, A. C., Kaschube, M. and Wieschaus, E. F.** (2009). Pulsed contractions of an actin-myosin network drive apical constriction. *Nature* **457**, 495-499.
- Mattila, P. K. and Lappalainen, P.** (2008). Filopodia: molecular architecture and cellular functions. *Nat Rev Mol Cell Biol* **9**, 446-454.
- McDonald, J. A., Khodyakova, A., Aranjuez, G., Dudley, C. and Montell, D. J.** (2008). PAR-1 kinase regulates epithelial detachment and directional protrusion of migrating border cells. *Curr Biol* **18**, 1659-1667.
- McMahon, A., Supatto, W., Fraser, S. E. and Stathopoulos, A.** (2008). Dynamic analyses of *Drosophila* gastrulation provide insights into collective cell migration. *Science* **322**, 1546-1550.
- Megason, S. G. and Fraser, S. E.** (2007). Imaging in systems biology. *Cell* **130**, 784-795.
- Michelson, A. M., Gisselbrecht, S., Zhou, Y., Baek, K. H. and Buff, E. M.** (1998). Dual functions of the heartless fibroblast growth factor receptor in development of the *Drosophila* embryonic mesoderm. *Dev Genet* **22**, 212-229.
- Misquitta, L. and Paterson, B. M.** (1999). Targeted disruption of gene function in *Drosophila* by RNA interference (RNA-i): a role for nautilus in embryonic somatic muscle formation. *Proc Natl Acad Sci U S A* **96**, 1451-1456.
- Montell, D. J.** (2006). The social lives of migrating cells in *Drosophila*. *Curr Opin Genet Dev* **16**, 374-383.

- Montell, D. J.** (2008). Morphogenetic cell movements: diversity from modular mechanical properties. *Science* **322**, 1502-1505.
- Mori, S., Wu, C. Y., Yamaji, S., Saegusa, J., Shi, B., Ma, Z., Kuwabara, Y., Lam, K. S., Isseroff, R. R., Takada, Y. K. et al.** (2008). Direct binding of integrin alphavbeta3 to FGF1 plays a role in FGF1 signaling. *J Biol Chem* **283**, 18066-18075.
- Morize, P., Christiansen, A. E., Costa, M., Parks, S. and Wieschaus, E.** (1998). Hyperactivation of the folded gastrulation pathway induces specific cell shape changes. *Development* **125**, 589-597.
- Murray, M. J. and Saint, R.** (2007). Photoactivatable GFP resolves Drosophila mesoderm migration behaviour. *Development* **134**, 3975-3983.
- Nabel-Rosen, H., Toledano-Katchalski, H., Volohonsky, G. and Volk, T.** (2005). Cell divisions in the drosophila embryonic mesoderm are repressed via posttranscriptional regulation of string/cdc25 by HOW. *Curr Biol* **15**, 295-302.
- Nobes, C. D. and Hall, A.** (1995). Rho, rac, and cdc42 GTPases regulate the assembly of multimolecular focal complexes associated with actin stress fibers, lamellipodia, and filopodia. *Cell* **81**, 53-62.
- O'Reilly, A. M., Lee, H. H. and Simon, M. A.** (2008). Integrins control the positioning and proliferation of follicle stem cells in the Drosophila ovary. *J Cell Biol* **182**, 801-815.
- Oda, H., Tsukita, S. and Takeichi, M.** (1998). Dynamic behavior of the cadherin-based cell-cell adhesion system during Drosophila gastrulation. *Dev Biol* **203**, 435-450.
- Oheim, M., Beaurepaire, E., Chaigneau, E., Mertz, J. and Charpak, S.** (2001). Two-photon microscopy in brain tissue: parameters influencing the imaging depth. *J Neurosci Methods* **111**, 29-37.

- Parks, S. and Wieschaus, E.** (1991). The *Drosophila* gastrulation gene *concertina* encodes a G alpha-like protein. *Cell* **64**, 447-458.
- Pawson, T.** (1995). Protein modules and signalling networks. *Nature* **373**, 573-580.
- Pertz, O. and Hahn, K. M.** (2004). Designing biosensors for Rho family proteins--deciphering the dynamics of Rho family GTPase activation in living cells. *J Cell Sci* **117**, 1313-1318.
- Pollard, T. D. and Borisy, G. G.** (2003). Cellular motility driven by assembly and disassembly of actin filaments. *Cell* **112**, 453-465.
- Prasad, M. and Montell, D. J.** (2007). Cellular and molecular mechanisms of border cell migration analyzed using time-lapse live-cell imaging. *Dev Cell* **12**, 997-1005.
- Raaijmakers, J. H. and Bos, J. L.** (2009). Specificity in Ras and Rap signaling. *J Biol Chem* **284**, 10995-10999.
- Raftopoulou, M. and Hall, A.** (2004). Cell migration: Rho GTPases lead the way. *Dev Biol* **265**, 23-32.
- Reed, B. H., McMillan, S. C. and Chaudhary, R.** (2009). The preparation of *Drosophila* embryos for live-imaging using the hanging drop protocol. *J Vis Exp*.
- Reedquist, K. A., Ross, E., Koop, E. A., Wolthuis, R. M., Zwartkruis, F. J., van Kooyk, Y., Salmon, M., Buckley, C. D. and Bos, J. L.** (2000). The small GTPase, Rap1, mediates CD31-induced integrin adhesion. *J Cell Biol* **148**, 1151-1158.
- Reuter, R. and Leptin, M.** (1994). Interacting functions of snail, twist and huckebein during the early development of germ layers in *Drosophila*. *Development* **120**, 1137-1150.

- Ridley, A. J., Schwartz, M. A., Burridge, K., Firtel, R. A., Ginsberg, M. H., Borisy, G., Parsons, J. T. and Horwitz, A. R.** (2003). Cell migration: integrating signals from front to back. *Science* **302**, 1704-1709.
- Riechmann, V., Irion, U., Wilson, R., Grosskortenhaus, R. and Leptin, M.** (1997). Control of cell fates and segmentation in the *Drosophila* mesoderm. *Development* **124**, 2915-2922.
- Rohde, L. A. and Heisenberg, C. P.** (2007). Zebrafish gastrulation: cell movements, signals, and mechanisms. *Int Rev Cytol* **261**, 159-192.
- Roote, C. E. and Zusman, S.** (1995). Functions for PS integrins in tissue adhesion, migration, and shape changes during early embryonic development in *Drosophila*. *Dev Biol* **169**, 322-336.
- Rorth, P.** (2007). Collective guidance of collective cell migration. *Trends Cell Biol* **17**, 575-579.
- Rorth, P.** (2009). Collective cell migration. *Annu Rev Cell Dev Biol* **25**, 407-429.
- Sato, M. and Kornberg, T. B.** (2002). FGF is an essential mitogen and chemoattractant for the air sacs of the *drosophila* tracheal system. *Dev Cell* **3**, 195-207.
- Schlessinger, J.** (1994). SH2/SH3 signaling proteins. *Curr Opin Genet Dev* **4**, 25-30.
- Schlessinger, J.** (2000). Cell signaling by receptor tyrosine kinases. *Cell* **103**, 211-225.
- Schumacher, S., Gryzik, T., Tannebaum, S. and Muller, H. A.** (2004). The RhoGEF Pebble is required for cell shape changes during cell migration triggered by the *Drosophila* FGF receptor Heartless. *Development* **131**, 2631-2640.
- Seher, T. C. and Leptin, M.** (2000). Tribbles, a cell-cycle brake that coordinates proliferation and morphogenesis during *Drosophila* gastrulation. *Curr Biol* **10**, 623-629.

- Seher, T. C., Narasimha, M., Vogelsang, E. and Leptin, M.** (2007). Analysis and reconstitution of the genetic cascade controlling early mesoderm morphogenesis in the *Drosophila* embryo. *Mech Dev* **124**, 167-179.
- Silver, D. L., Geisbrecht, E. R. and Montell, D. J.** (2005). Requirement for JAK/STAT signaling throughout border cell migration in *Drosophila*. *Development* **132**, 3483-3492.
- Smallhorn, M., Murray, M. J. and Saint, R.** (2004). The epithelial-mesenchymal transition of the *Drosophila* mesoderm requires the Rho GTP exchange factor Pebble. *Development* **131**, 2641-2651.
- Stathopoulos, A. and Levine, M.** (2004). Whole-genome analysis of *Drosophila* gastrulation. *Curr Opin Genet Dev* **14**, 477-484.
- Stathopoulos, A., Tam, B., Ronshaugen, M., Frasch, M. and Levine, M.** (2004). pyramus and thisbe: FGF genes that pattern the mesoderm of *Drosophila* embryos. *Genes Dev* **18**, 687-699.
- Stern.** (2004). Gastrulation: From Cells to Embryos. Cold Spring Harbor, NY: Cold Spring Harbor Press.
- Sternberg, P. W. and Alberola-Ila, J.** (1998). Conspiracy theory: RAS and RAF do not act alone. *Cell* **95**, 447-450.
- Supatto, W., Fraser, S. E. and Vermot, J.** (2008). An all-optical approach for probing microscopic flows in living embryos. *Biophys J* **95**, L29-31.
- Supatto, W., McMahon, A., Fraser, S. E. and Stathopoulos, A.** (2009). Quantitative imaging of collective cell migration during *Drosophila* gastrulation: multiphoton microscopy and computational analysis. *Nat Protoc* **4**, 1397-1412.

- Supatto, W., Debarre, D., Moulia, B., Brouzes, E., Martin, J. L., Farge, E. and Beaufrepaire, E.** (2005). In vivo modulation of morphogenetic movements in *Drosophila* embryos with femtosecond laser pulses. *Proc Natl Acad Sci U S A* **102**, 1047-1052.
- Thisse, B. and Thisse, C.** (2005). Functions and regulations of fibroblast growth factor signaling during embryonic development. *Dev Biol* **287**, 390-402.
- Tyszka, J. M., Ewald, A. J., Wallingford, J. B. and Fraser, S. E.** (2005). New tools for visualization and analysis of morphogenesis in spherical embryos. *Dev Dyn* **234**, 974-983.
- Valentin, G., Haas, P. and Gilmour, D.** (2007). The chemokine SDF1a coordinates tissue migration through the spatially restricted activation of *Cxcr7* and *Cxcr4b*. *Curr Biol* **17**, 1026-1031.
- van Impel, A., Schumacher, S., Draga, M., Herz, H. M., Grosshans, J. and Muller, H. A.** (2009). Regulation of the Rac GTPase pathway by the multifunctional Rho GEF Pebble is essential for mesoderm migration in the *Drosophila* gastrula. *Development* **136**, 813-822.
- Vermot, J., Fraser, S. E. and Liebling, M.** (2008). Fast fluorescence microscopy for imaging the dynamics of embryonic development. *HFSP J* **2**, 143-155.
- Vicente-Manzanares, M., Choi, C. K. and Horwitz, A. R.** (2009). Integrins in cell migration--the actin connection. *J Cell Sci* **122**, 199-206.
- Vincent, S., Wilson, R., Coelho, C., Affolter, M. and Leptin, M.** (1998). The *Drosophila* protein Dof is specifically required for FGF signaling. *Mol Cell* **2**, 515-525.

- Voiculescu, O., Bertocchini, F., Wolpert, L., Keller, R. E. and Stern, C. D.** (2007). The amniote primitive streak is defined by epithelial cell intercalation before gastrulation. *Nature* **449**, 1049-1052.
- Wang, Y. and Steinbeisser, H.** (2009). Molecular basis of morphogenesis during vertebrate gastrulation. *Cell Mol Life Sci* **66**, 2263-2273.
- Weijer, C. J.** (2009). Collective cell migration in development. *J Cell Sci* **122**, 3215-3223.
- Welte, M. A., Gross, S. P., Postner, M., Block, S. M. and Wieschaus, E. F.** (1998). Developmental regulation of vesicle transport in *Drosophila* embryos: forces and kinetics. *Cell* **92**, 547-557.
- Wilson, R. and Leptin, M.** (2000). Fibroblast growth factor receptor-dependent morphogenesis of the *Drosophila* mesoderm. *Philos Trans R Soc Lond B Biol Sci* **355**, 891-895.
- Wilson, R., Vogelsang, E. and Leptin, M.** (2005). FGF signalling and the mechanism of mesoderm spreading in *Drosophila* embryos. *Development* **132**, 491-501.
- Yang, X., Dormann, D., Munsterberg, A. E. and Weijer, C. J.** (2002). Cell movement patterns during gastrulation in the chick are controlled by positive and negative chemotaxis mediated by FGF4 and FGF8. *Dev Cell* **3**, 425-437.
- Yayon, A., Klagsbrun, M., Esko, J. D., Leder, P. and Ornitz, D. M.** (1991). Cell surface, heparin-like molecules are required for binding of basic fibroblast growth factor to its high affinity receptor. *Cell* **64**, 841-848.

Yu, S. R., Burkhardt, M., Nowak, M., Ries, J., Petrasek, Z., Scholpp, S., Schwille, P. and Brand, M. (2009). Fgf8 morphogen gradient forms by a source-sink mechanism with freely diffusing molecules. *Nature* **461**, 533-536.

Zallen, J. A. and Blankenship, J. T. (2008). Multicellular dynamics during epithelial elongation. *Semin Cell Dev Biol* **19**, 263-270.

Zamir, E. A., Czirok, A., Cui, C., Little, C. D. and Rongish, B. J. (2006). Mesodermal cell displacements during avian gastrulation are due to both individual cell-autonomous and convective tissue movements. *Proc Natl Acad Sci U S A* **103**, 19806-19811.